CHARGE AND SPIN TRANSPORT STUDIES IN GRAPHENE AND BLACK PHOSPHORUS

GAVIN KOON KOK WAI

DEPARTMENT OF PHYSICS
NATIONAL UNIVERSITY OF SINGAPORE

(2015)

CHARGE AND SPIN TRANSPORT STUDIES IN GRAPHENE AND BLACK PHOSPHORUS

GAVIN KOON KOK WAI

(*B.Sc. & B.Eng. National University of Singapore*)

A THESIS SUBMITTED

FOR THE DEGREE OF DOCTOR OF PHILOSOPHY

DEPARTMENT OF PHYSICS

NATIONAL UNIVERSITY OF SINGAPORE

(2015)

DECLARATION

I hereby declare that this thesis is originally conducted and written solely by me in its entirety.

I have duly acknowledged all sources of information which have been used directly or indirectly in the thesis.

This thesis has never previously been submitted for any degree in any university.

______________ ____________________

Date Gavin Koon Kok Wai

This thesis is dedicated to my late grandparents.

Your love stays forever with me.

ACKNOWLEDGEMENT

First and foremost, I express my deepest gratitude to both my parents and sister for their endless love and encouragement while I pursue my lifelong ambition; without them I certainly would not be where I am today. I take this opportunity especially to thank my aunt, Ms. Lim Lian Hong for her constant care and generosity in supporting me financially throughout my years of tertiary studies and my uncle, Mr. Lim Hwa Meng for being my caring guardian in Singapore and my role model. To my other respectable uncle and devoted aunts, I extend my sincere gratitude and appreciation for their affectionate support constantly offered without any hesitation.

I expressly thank Prof. Barbaros Özyilmaz for granting me a great opportunity to pursue my Ph.D. studies in his fully equipped graphene lab and Prof. Antonio H. Castro Neto for providing me financial support in my final year of Ph.D. studies.

I sincerely thank both Dr. Jayakumar Balakrishnan and Dr. Ahmet Avsar; whom I had constantly worked with during my initial years of graduate studies. They have rendered me valuable assistance and profound advice whenever needed. I am very grateful to Mr. Toh Chee Tat and Mr. Ho Yu Da; both for their friendship and regular presence in making this a pleasant journey right from the start.

I am highly grateful to Dr. Xu Xiangfan, Dr. Eoin Conor O’Farrell, Dr. Lee Jonghak and Dr. Ivan J. Vera Marun; for their teaching and guidance throughout my time in the research lab. I also extend my warmest appreciation to my fellow lab colleagues, Mr. Wu Jing, Mr. Henrik Andersen, Mr. Tan Jun You and Ms. Yeo Yuting for their significant and beneficial

collaboration and to my three closest friends; Mr. Wong Joe Yee, Mr. Tee Ting Leong and Mr. Tan Chin Han for their steady motivation.

Last but not least, I express my heartfelt appreciation to my fiancée, Ms. Chow Kai Hui; whose unconditional love, care and moral support over the years has inspired me to improve myself to levels beyond my initial expectation and especially for making Singapore a new home for me.

And most importantly and proudly, I extend my humble but highest appreciation to The National University of Singapore for offering me such a priceless opportunity and an ideal environment to pursue my studies for the past decade.

TABLE OF CONTENTS

ACKNOWLEDGEMENT 5
ABSTRACT 10
LIST OF FIGURES 11
CHAPTER 1 INTRODUCTION 25
1.1 SPINTRONICS 25
1.2 THERMOELECTRIC 29
1.3 THESIS OUTLINE 32
CHAPTER 2 BASIC CONCEPTS 35
2.1 GRAPHENE 35
2.1.1 INTRODUCTION 35
2.1.2 ELECTRONIC STRUCTURE 36
2.1.3 ELECTRONIC PROPERTIES 41
2.1.4 ELECTRONIC TRANSPORT UNDER MAGNETIC FIELD 42
2.2 BLACK PHOSPHORUS 43
2.2.1 INTRODUCTION 43
2.2.2 ELECTRONIC STRUCTURE 44
2.2.3 ELECTRONIC PROPERTIES 48
2.3 SPINTRONICS 49
2.3.1 ELECTRICAL SPIN INJECTION AND DETECTION 49
2.3.2 NON-LOCAL SPIN VALVE CONFIGURATION 52
2.3.3 SPIN-ORBIT COUPLING 56
2.3.4 SPIN HALL EFFECT 63
2.3.5 GRAPHENE SPINTRONICS 69
2.4 THERMOELECTRIC 73
2.4.1 SEEBECK-PELTIER-THOMSON EFFECT 73
2.4.2 THERMOELECTRIC TRANSPORT IN SOLIDS 76
CHAPTER 3 EXPERIMENTAL TECHNIQUES 83
3.1 FROM BULK TO 2D 83
3.1.1 GRAPHENE 83
3.1.2 BLACK PHOSPHORUS 85
3.2 CHEMICAL VAPOUR DEPOSITION GRAPHENE 86
3.2.1 PREPARATION 86
3.3 GRAPHENE SPIN HALL EFFECT DEVICES 87
3.4 BLACK PHOSPHORUS DEVICES 92
3.4.1 THERMOELECTRIC 93
3.4.2 PHOTODETECTOR 95

3.5 MEASUREMENT SET-UPS AND TECHNIQUES 95
3.5.1 MEASUREMENT SET-UPS 96
3.5.2 ELECTRICAL CHARGE TRANSPORT MEASUREMENTS FOR GRAPHENE BASED DEVICES 97
3.5.3 ELECTRICAL SPIN HALL EFFECT MEASUREMENTS FOR GRAPHENE BASED DEVICES 98
3.5.4 THERMOELECTRIC MEASUREMENTS FOR BLACK PHOSPHORUS BASED DEVICES 99
3.5.5 PHOTODETECTION MEASUREMENTS FOR BLACK PHOSPHORUS BASED DEVICES 100
CHAPTER 4 SPIN HALL EFFECT IN FUNCTIONALIZED GRAPHENE 101
4.1 COLOSSAL ENHANCEMENT OF SPIN-ORBIT COUPLING IN WEAKLY HYDROGENATED GRAPHENE 101
4.1.1 HYDROGENATION OF EXFOLIATED GRAPHENE 103
4.1.2 ELECTRICAL CHARGE AND SPIN CHARACTERIZATION 108
4.1.3 MAGNETIC FIELD MEASUREMENTS 110
4.1.4 ADDITIONAL NON-LOCAL STUDIES AND SPIN-ORBIT COUPLING STRENGTH 111
4.2 SPIN HALL EFFECT IN SEMI-IONIC FLUORINATED GRAPHENE 116
4.2.1 PREPARATION OF FLUORINATED GRAPHENE 117
4.2.2 ELECTRICAL CHARGE CHARACTERIZATION 118
4.2.3 ELECTRICAL SPIN CHARACTERIZATION 119
CHAPTER 5 GIANT SPIN HALL EFFECT IN GRAPHENE GROWN BY CHEMICAL VAPOUR DEPOSITION 121
5.1 CVD GRAPHENE AND EXFOLIATED GRAPHENE DECORATED BY METALLIC ADATOMS 123
5.2 DEVICE FABRICATION AND CHARACTERIZATION 124
5.2.1 DEVICE FABRICATION 124
5.2.2 RAMAN CHARACTERIZATION 127
5.2.3 EDX AND XPS CHARACTERIZATION 128
5.2.4 PRELIMINARY ELECTRICAL CHARGE AND SPIN TRANSPORT CHARACTERIZATION 129
5.3 ELECTRICAL SPIN HALL EFFECT MEASUREMENTS 131
5.4 SPIN ORBIT COUPLING STRENGTH 146
CHAPTER 6 COLOSSAL THERMOELECTRIC RESPONSE IN FEW-LAYER BLACK PHOSPHORUS 152
6.1 BLACK PHOSPHORUS BASED THERMOELECTRIC DEVICES 154
6.2 DEVICE FABRICATION AND CHARACTERIZATION 154
6.2.1 DEVICE FABRICATION AND RAMAN CHARACTERIZATION 154
6.2.2 ELECTRICAL CHARGE TRANSPORT MEASUREMENTS 156

6.3 THERMOELECTRIC MEASUREMENTS AND FIGURE OF MERIT ZT 158
6.4 THERMOELECTRIC RESPONSE FOR THINNER BLACK PHOSPHORUS ... 166
6.5 PHONON DRAG IN BLACK PHOSPHORUS 169
CHAPTER 7 SUMMARY AND FUTURE WORK 175
7.1 GRAPHENE SPINTRONICS 175
7.2 BLACK PHOSPHORUS THERMOELECTRIC 176
7.3 BLACK PHOSPHORUS ULTRAVIOLET PHOTODETECTOR 177
7.4 BLACK PHOSPHORUS SPINTRONICS 178
BIBLIOGRAPHY 179
LIST OF PUBLICATIONS 196

ABSTRACT

Transport studies in graphene and black phosphorus two-dimensional systems will be explored in this thesis. Specifically, I studied the spin transport and spin characteristics of graphene subjected to an enhancement of its otherwise low intrinsic spin-orbit coupling. Taking advantage of its flexibility for engineering modification, we enhanced the spin-orbit coupling via chemical functionalization and metallic adatom decoration. With the initial aim of studying spin transport in black phosphorus which has an energy band gap, I unexpectedly uncovered black phosphorus' potential as an outstanding thermoelectric material. Our discovery also agrees well with a recent theoretical prediction of high thermopower factor in black phosphorus. The published works on graphene spintronics described in this thesis are both scientifically enlightening and technologically promising[1,2]. We have also demonstrated the first thermoelectric response in few layer black phosphorus crystals and the performance of this elemental semiconductor is comparable to the state of the art hybrid heterostructures/nanostructures.

LIST OF FIGURES

Figure 2- 1: The hexagonal lattice of carbon atoms showing carbon atoms on site A and B. The lattice can also be seen as two overlapping triangular lattices..37

Figure 2- 2: The first Brillouin zone of graphene (adapted from Vozmediano[55]). 38

Figure 2- 3: Layered structure of black phosphorus with puckered honeycomb lattice (adapted from Liu et al.)[60]. 43

Figure 2- 4: Projection of two adjacent layers on x-y plane. 45

Figure 2- 5: First Brillouin zone of black phosphorus as given by the bold lines and the light rectangle line showing the Brillouin zone for a two-dimensional single layer black phosphorus. 46

Figure 2- 6: Electronic band structure for bulk black phosphorus (adapted from Takao et al.)[63]. 47

Figure 2- 7: Typical conductance of few layers black phosphorus as a function of back gate voltage with source drain voltage V_{SD}=0.1 V. Inset: I-V characteristics of the same junction with different applied back gate voltage. 48

Figure 2- 8: Schematic illustration of the density of states in a) ferromagnetic material, b) un-polarized non-magnetic material and c) spin-polarized non-magnetic material.....................51

Figure 2- 9: Schematic diagram of a non-local spin valve geometry and measurement configuration. In this configuration, red contacts denote the ferromagnetic metal and yellow denotes the non-magnetic channel. 52

Figure 2- 10: Electrical spin precession of the injected spins under an applied out-of-plane magnetic field..55

Figure 2- 11: Schematics showing the trajectory of spin-up and spin-down electrons after skew scattering process. The angle θ denotes the deflection angle of the electrons........................59

Figure 2- 12: Schematics showing the trajectory for both spin-up and spin-down electrons after side-jump scattering process. The vector δ denotes the sideway displacement for both spin-up and spin-down electrons. 60

Figure 2- 13: Schematic showing the orthogonally aligned charge and spin currents; the longitudinal charge current induces a transverse spin current under spin Hall Effect due to an accumulation of spin-up and spin-down electrons on the opposite sides. 63

Figure 2- 14: Schematic showing the measurement configuration for the detection of non-equilibrium spins via the non-local inverse spin Hall Effect. In this case, the spin accumulation is injected into the non-magnetic system via a ferromagnetic metal with magnetization M... 65

Figure 2- 15: Schematic showing the non-local H-bar measurement configuration for the detection of non-equilibrium spins via the inverse spin Hall Effect. In this case, the spin accumulation is injected into the non-magnetic system via the spin Hall Effect. 66

Figure 2- 16: Schematic showing non-local spin detection in the diffusive regime (H-bar configuration). Black arrow denotes the direction of charge current which is perpendicular to the spin current (blue arrow) and the corresponding system dimensions. In the case of precession measurement, the in plane magnetic field is applied in the direction as shown. ... 67

Figure 2- 17: Schematics for Elliot-Yafet spin relaxation mechanism. The momentum scattering by impurities or phonons has a finite probability to flip the electron spin. 70

Figure 2- 18: Schematic for D'yakonov-Perel spin relaxation mechanism. Electron spin flip occurs via electron spin precession about the momentum dependent magnetic field. 71

Figure 2- 19: Schematics illustrating Seebeck effect with two junctions formed by two dissimilar materials subjected to a temperature gradient. 73

Figure 2- 20: Schematics showing Peltier effect whereby heat can be generated or removed in a junction between two distinct materials depending on the direction of the applied electrical current. 74

Figure 2- 21: Schematics showing Thomson effect; combination of Seebeck and Peltier effects in a single material whereby a temperature gradient creates a variation of Seebeck coefficient and in turn causes a continuous Peltier effect. 75

Figure 2- 22: Schematics showing normal scattering with **q** being parallel to **Δk**. 79

Figure 2- 23: Schematics showing Umklapp scattering process with **q** being antiparallel to **Δk**. 80

Figure 2- 24: Schematics showing a single thermoelectric couple for thermoelectric power generation. In this case black phosphorus can be doped to p-type and n-type to be incorporated into a single thermoelectric couple device. Multiple of these thermoelectric couples can then be connected electrically in series and thermally in parallel to create a thermoelectric module for energy harvesting system. 82

Figure 3- 1: Optical images showing the different steps in obtaining exfoliated graphene via micro-mechanical exfoliation method with scotch tape. 84

Figure 3- 2: a) Scanning electron microscope (SEM) image with false color of a hydrogenated exfoliated graphene hall bar device with varying junction lengths. Inset: Optical microscope image of the same device. b) Atomic force microscopy (AFM) image of a CVD grown graphene hall bar device with varying junction lengths. Scale bar is 2 μm. 88

Figure 3- 3: Schematic diagrams showing the device fabrication steps involved by using positive electron beam resist such as PMMA. 89

Figure 3- 4: Schematic diagrams showing the device fabrication steps involved (up to development) by using negative electron beam resist such as HSQ. 89

Figure 3- 5: Optical images of graphene taken after a) patterning of alignment markers (graphene is area with darker contrast), b) patterning of device electrodes with the aid of the patterned alignment markers, c) thermal evaporation of Cr/Au metals and liftoff process and d)

patterning of etch mask to define the unwanted area of graphene to be etched away. Scale bar in a) is 100 µm and in b), c), and d) is 50 µm. 91

Figure 3- 6: Optical images of CVD graphene taken after a) patterning of etch mask with metal alignment markers, b) RIE O2 plasma of unwanted areas of CVD graphene (to define CVD graphene device channel) and c) liftoff of PMMA resist layers in acetone. Scale bar denotes 20 µm. 92

Figure 3- 7: Optical microscope images of few layers black phosphorus taken after a), b) patterning of alignment markers c), d) patterning of device electrodes with the aid of the defined alignment markers and e), f) thermal evaporation of Ti/Au metals and liftoff process. Scale bar in a) and b) is 100 µm and in c), d), e) and f) is 50 µm. 94

Figure 3- 8: Optical microscope images of four different black phosphorus crystals with patterned electrodes (2-probe devices). Scale bar is 20 µm. 95

Figure 3- 9: Schematics showing the measurement configurations for local transport, two-probe or four-probe measurements. 97

Figure 3- 10: Schematics showing the measurement configuration for non-local transport, spin Hall measurement. 98

Figure 4- 1: Schematics showing the measurement configuration of non-local spin Hall Effect. Inset: the deformation of graphene lattice from sp2 to sp3 due to hydrogenation. 102

Figure 4- 2: Optical microscope image of an exfoliated graphene device (after thermal evaporation) with hydrogen silsesquioxane (HSQ) resist as etch mask to define the desired Hall bar graphene channel. 103

Figure 4- 3: Hydrogenation percentage as a function of irradiation dose of HSQ as obtained from Raman measurements 104

Figure 4- 4: The evolution of D peak in the Raman spectrum showing progressive hydrogenation percentage in graphene with increasing irradiation dose of HSQ. 105

Figure 4- 5: a) Change of Si-H peak at 2265 cm^{-1} as a function of irradiation dose. The peak intensity decreases with increasing dose indicating the dissociation of hydrogen from HSQ. b) Raman spectrum of a hydrogenated graphene SHE device showing the reversibility of hydrogenation upon annealing in argon environment at 250 °C for 2 hours. Constant gas flow of argon was maintained during annealing process ~0.3 $lmin^{-1}$. The disappearance of D peak after annealing shows that HSQ irradiation creates minimal vacancies/defects to graphene lattice. 106

Figure 4- 6: a) Increment of I_D/I_G Raman peak ratios of graphene coated with HSQ irradiated with increasing EBL dose. b) σ versus n plot for one of these devices irradiated with EBL dose of 1 $mCcm^{-2}$. The red curve is a fit to the plot with resonant scatters which gives an impurity density of 1×10^{12} cm^{-2}..106

Figure 4- 7: Scanning electron micrograph of a hydrogenated graphene hall bar device showing multiple junctions with different lengths. Scale bar denotes 5μm. 108

Figure 4- 8: a) Non-local signal versus n for pristine graphene sample and hydrogenated graphene sample at room temperature. The dashed grey line denotes the ohmic contribution to the measured signal. Inset: resistivity versus n for pristine and hydrogenated graphene. b) Non-local signal dependence on hydrogenation percentage. The dashed grey line denotes the calculated ohmic contribution for this device. 109

Figure 4- 9: Parallel field precession curve for device with L/W=5 and mobility of ~20,000 $cm^2V^{-1}s^{-1}$. The red dashed line is the fit to measurement data. 110

Figure 4- 10: Length dependence of non-local signal at room temperature (red solid circle: 0.02 % hydrogenation and blue: 0.05 % hydrogenation). a) At CNP. b) At $n=1\times10^{12}$ cm^{-2}. The solid

lines are the fit for the measurement data and dashed grey line is the calculated ohmic contribution. 111

Figure 4- 11: Width dependence of non-local signal at room temperature. Length L=2 µm, red solid line is the fit to the measurement data and dashed grey line is the calculated ohmic contribution. Inset: width dependence on a linear scale. 112

Figure 4- 12: A plot of ln R versus ln W showing the power law dependence of the measured non-local signal with width W. This power law dependence signifies that the measured signal is due to SHE. The dashed grey line denotes calculated ohmic contribution. 114

Figure 4- 13: Schematics representation of the s-FG based device fabrication and reduction process; schematics of s-FG and reduced s-FG strucures. Scale bar is 50 µm. 117

Figure 4- 14: Raman characteristics and resistance versus back gate voltage of reduced single layer s-FG device, a) as prepared, b) intermediate reduction and c) one week reduction. 118

Figure 4- 15: Local (solid line) and non-local (dashed) signal dependence on back gate voltage V_g at room temperature. For comparison both hydrogenated graphene (red) and fluorinated graphene (blue) are plotted. Both devices have length to width ratio of L/W=1.5. 119

Figure 5- 1: Schematic diagram showing a graphene non-local Hall bar device with junctions of different length with adatom impurities (red solid spheres). 123

Figure 5- 2: a) AFM scan for Cu-CVD graphene device after annealing at 300 °C, particle analysis show details of distribution of particle sizes on graphene and the average of Cu nanoparticle size in this device is about ~40 nm in diameter. b) SEM and c) AFM scans of graphene device with Au adatoms. Scale bar is 2µm. 126

Figure 5- 3: Optical image of a 3 by 3 array of CVD graphene devices on Si/SiO_2 substrate together with Raman and SEM image of the graphene channel in a typical spin Hall device. Scale bar is 5 µm. 127

Figure 5- 4: Raman mapping of a CVD graphene device (upper panel) and exfoliated graphene device (lower panel) showing the 2D (2680 cm^{-1}), G (1560 cm^{-1}) and D (1360 cm^{-1}) peak intensities. The prominent relative 2D peak intensity with respect to G peak intensity confirms that the Cu-CVD graphene samples are monolayer. A comparison of the CVD Raman scan with that of the exfoliated pristine graphene device show negligible D peak for the entire channel of the device and is similar to the Raman mapping of exfoliated graphene device. 127

Figure 5- 5: EDX spectrum of CVD graphene sample. The samples for EDX measurements are prepared on a standard transmission electron microscopy (TEM) gold grids and are hence suspended samples. Size of each grid is 7 μm by 7 μm. The additional Au peaks in the EDX spectrum are due to the presence of gold TEM grids. Inset: XPS data on CVD graphene showing Cu 2p peaks. 128

Figure 5- 6: Resistivity versus n for the upper and lower contacts in the H bar geometry. Inset: the low temperature data for the AHE measurement showing the absence of any transverse Hall signal at zero magnetic field. 129

Figure 5- 7: a) Non-local spin valve measurements for in-plane magnetic field. b) Non-local spin valve Hanle precession measurements for Cu-CVD graphene devices for parallel (blue solid circles) and antiparallel (black solid circles) configuration of the injector and detector electrodes. The red lines are the fits to the measured data. 130

Figure 5- 8: AFM three-dimensional surface topography of a typical spin Hall device with details of actual spin Hall measurements. 131

Figure 5- 9: Non-local signal versus n for pristine graphene sample (lower panel) and Cu-CVD graphene (upper panel). L/W=2 for both devices. The grey dashed line represents the ohmic contribution in these devices. 133

Figure 5- 10: Measured non-local signal (voltage) as a function of source drain current. 134

Figure 5- 11: R_{NL}/ρ versus length for CVD graphene with width W=500 nm. The plotted data are average values for three different samples and the error bar corresponds to the standard deviation from the mean value. Inset: Non-local signal for different L/W ratio of the channel. 135

Figure 5- 12: a) Width dependence of the non-local signal for different carrier densities. b) The carrier density dependence of the extracted spin Hall angle. c) spin Hall conductivity for the same sample. 136

Figure 5- 13: The in-plane magnetic field dependence of the non-local signal for Cu-CVD graphene samples. The dotted line is the fit for the data. Inset: magnetic field dependence of pristine exfoliated graphene sample. 137

Figure 5- 14: Non-local spin Hall precession measurements showing un-damped oscillatory behavior. 139

Figure 5- 15: Additional in-plane magnetic field dependence data of non-local signal at different back gate voltages for device decorated with Au adatoms. 140

Figure 5- 16: Length dependence of the non-local signal for exfoliated graphene samples immersed in the etchant solution of ammonium persulphate. The width of the sample is W=500 nm. The measured non-local signal is comparable to the calculated ohmic contribution. Inset: non-local signal versus n for junction with dimensions L/W=2. 141

Figure 5- 17: Length dependence of the non-local signal for Cu-CVD graphene sample before and after vacuum annealing at 400 K for 24 hours. 142

Figure 5- 18: a) Comparison of Raman 2D peak for Cu-CVD and exfoliated graphene samples. b) Comparison of Raman G peak for Cu-CVD and exfoliated graphene samples. c) Raman G peak shift for hydrogenated graphene sample showing the chemisorbed nature of the adsorption. 144

Figure 5- 19: a) and b) Length and width dependence of the non-local signal for exfoliated graphene samples decorated with Cu, Au and Ag adatoms. The grey dotted line shows the measured non-local signal (which is equal to the ohmic contribution) for a pristine graphene sample. Inset of a): non-local signal versus n. 145

Figure 5- 20: a) In-plane magnetic field dependence precession measurements for exfoliated graphene device with Cu adatoms. b) For exfoliated graphene device with Au adatoms. The blue dashed lines are fit to the experimental data. L/W=3 for all samples with comparable mobility ~10,000 $cm^2V^{-1}s^{-1}$. 146

Figure 5- 21: The Fermi energy dependence of the spin relaxation time for various adatoms. 147

Figure 5- 22: Room temperature data for the Cu-CVD graphene sample. The (dashed) blue line is the ideal spin Hall angle as generated by SOC active dilute Cu clusters in otherwise perfect graphene. The (solid) orange line shows the realistic spin Hall coefficient taking into account other sources of disorder (modelled here as resonant scatterers). Calculations in this plot were performed at room temperature and neglecting the effect of quantum side jump. 149

Figure 5- 23: The Fermi energy dependence of the longitudinal (charge) conductivity at room temperature for the Cu-CVD graphene sample. The (solid) orange line shows the theoretical value of the conductivity. The excellent qualitative agreement shows that fit parameters are consistent with charge transport characteristics of the system. 149

Figure 5- 24: The Fermi-energy dependence of the spin Hall coefficient for Cu-CVD graphene extracted from the length dependence data and theoretically calculated Fermi-energy dependence of spin Hall coefficient in the resonant scattering regime taking into account Cu adatoms and other impurities limiting charge transport. The data points are from fitting the length dependence at the specified Fermi energy and the error bar corresponds to the standard deviation for spin Hall coefficient obtained from the fitting. 150

Figure 6- 1: Architecture of a mesoscopic few-layer phosphorene thermoelectric device. Schematic of a single layer phosphorene device. A snake shaped micro-fabricated resistor is used to create a thermal gradient (red) via Joule heating. Metal Au electrodes (yellow) serve as electrical contacts to the phosphorene channel, and as resistive thermometers when measured in a four-terminal configuration. NiCu electrodes (blue) are used to make the 4-terminal connection to the Au electrodes, and also as alternative NiCu/Au thermocouple thermometers. Atomic force microscopy image of a few-layer phosphorene device showing the same architecture. 152

Figure 6- 2: Raman characterization of a black phosphorus based thermoelectric device showing the orientation of the black phosphorus crystal with respect to the heater element. The A^2_g/A^1_g ratio shows that in this device the thermoelectric transport was probed along the light effective mass direction[55]. 156

Figure 6- 3: Electrical resistance of the black phosphorus (~12 nm) measured at room temperature with source drain bias of 50 mV. 156

Figure 6- 4: a) Au electrode 4-terminal resistance versus dc bias applied to heater element, at a base temperature of 20 K. The red line is the parabolic fit characteristic of Joule heating. b) Calibration of Au electrode 4-terminal resistance versus temperature. The data in a) and b) are combined to measure the temperature increase at the electrode location due to the heater element, with a typical resolution of 10 mK. c) Temperature bias ΔT, obtained by subtracting the temperature of two Au electrodes, applied to sample from Figure 6-10 versus reference temperature T. d) Temperature profile at room temperature along a black phosphorus device, referenced to the last electrode. Black symbols correspond to the Au resistive thermometry discussed in the previous panels, the standard method used in this work. Red symbols correspond to the NiCu/Au thermocouple thermometry, showing agreement with the Au

thermometry but with a resolution < 5 mK. Error bars in c) and d) are derived from the standard errors in the parabolic fit (as in a)) and in ∂R/∂T (as in b)). 158

Figure 6- 5: a) Local thermometry for 13 nm black phosphorus (T black) and corresponding ‘ghost device’ (T* red) under a heater current of 2 mA. The inset is an optical image indicating the location of the thermometry. b) Comparative thermometry from data shown in a. For all base temperatures we observe a difference T-T*≤1 mK. c) Simulation of temperature profile along black phosphorus (black) and ‘ghost device’ (red) using a model (see inset) of the sample shown in a). Black phosphorus acts as a thermal shunt, leading to a smaller thermal gradient than that of the bare substrate. The dashed line indicates the location of where T and T* are obtained. A large κ= 100 $Wm^{-1}K^{-1}$ is used to make the effect apparent. d) Dependence of T-T* on κ. The result consistent with our measurements (1 mK, κ = 13 $Wm^{-1}K^{-1}$) is indicated by dashed lines. The hatched area indicates the range ruled out (κ>30 $Wm^{-1}K^{-1}$) by our measurements. 160

Figure 6- 6: Room temperature thermoelectric response for sample from Figure 6-10, before cooldown. a) Electrical resistance. b) Seebeck coefficient. The bandgap region is visible as the highly insulating region where the Seebeck coefficient becomes zero. The black curve corresponds to the standard lock-in measurement configuration at 4 Hz, same as in Figure 6-10. The red curve corresponds to inverting the voltage probes, its similar magnitude and opposite polarity to the standard configuration demonstrates the differential nature of the measurement and the absence of any significant common-mode signal. The blue curve is a standard measurement at 1.5 Hz (and half the Vg sweep rate), its similar magnitude and lineshape to the measurement at 4 Hz demonstrates the quasi-steady-state equilibrium in the range of frequencies used (1.5–4 Hz). 162

Figure 6- 7: Thermoelectric response in 12 nm thick black phosphorus at room temperature. a) and b) Electrical resistance (V=50 mV) and Seebeck coefficient (ΔT=170 mK). c) Power factor

$S^2\sigma$ calculated from data in a) and b) and ZT considering a thermal conductivity κ=12 $Wm^{-1}K^{-1}$. The inset zooms into the region around Vg=0. For all panels black and red lines correspond to Vg trace (40→40) and retrace (-40→40) sweeps, respectively. The gray and light red bands are errors due to ΔT. 163

Figure 6- 8: Thermoelectric response for 8 nm thick black phosphorus showing bandgap region at room temperature. a) and b) Electrical resistance (V=100 mV) and Seebeck coefficient (ΔT=50 mK). The bandgap region is visible as the highly insulating region where the Seebeck coefficient becomes zero. The inset in b zooms into the region of large hole doping showing saturation of the Seebeck coefficient to a value of 200 μV/K. c) Power factor $S^2\sigma$ calculated from data in a) and b) and ZT considering a thermal conductivity κ=12 $Wm^{-1}K^{-1}$. The inset shows the maximum ZT values achieved for different thicknesses. Open symbols in b) and c) correspond to R > 100 MΩ. The gray bands are errors due to ΔT. 166

Figure 6- 9: Thermoelectric response for 6 nm thick black phosphorus at room temperature. a) Electrical resistance (V=100 mV). b) Seebeck coefficient (ΔT=200 mK). The gray band is the error due to ΔT. Compared with the thicker samples, this sample showed lower mobility, a larger bandgap region and unipolar FET operation. The Seebeck coefficient is underestimated due to the resistance of the sample being > 100 MΩ...168

Figure 6- 10: Low temperature thermoelectric response. a) and b) Electrical resistance and Seebeck coefficient at different temperatures for 8 nm thick, 8.5 μm long sample. The electrical response showed no significant hysteresis for T<200 K (Figure 6-11). c) and d) 2D maps of the temperature dependence of the electric (V=100 mV) and thermoelectric responses, respectively. Black contours in c correspond to I = 10^{-9} A indicating the band edges. Blue (red) contours in d) correspond to S=+(-)3 mVK^{-1}. e) Maximum Seebeck coefficient versus temperature. Red (blue) symbols correspond to electron (hole) regime. Open stars correspond

to the initial room temperature measurement (Figure 6-6). Error bars are due to uncertainty in ΔT. The dashed line is the phonon-drag model described in the discussion. 169

Figure 6- 11: Low temperature thermoelectric response including trace and retrace analysis, for sample from Figure 6-10. a) Maximum Seebeck coefficient versus temperature, separately for Vg trace (80→80) and retrace (-80→80) sweeps. Red and blue symbols correspond to electron and hole regimes. Filled and open symbols correspond to trace and retrace sweeps. Error bars are due to uncertainty in ΔT. b) Vg position of Seebeck maximum versus temperature. Symbols have the same meaning as in a. Note the absence of hysteresis below 200 K for the electric response and for the maximum hole thermopower. 2D maps of the temperature dependence are shown for the electric response (V=100 mV) in c) (trace) and d) (retrace), and for the thermoelectric response in e) (trace) and f) (retrace). Black contours in c) and d) correspond to R=100 MΩ, indicating the band edges. Blue (red) contours in e) and f) correspond to S=+(-)3 mVK^{-1}. 170

Figure 6- 12: Additional low temperature thermoelectric response for 9 nm thick black phosphorus. a) Maximum Seebeck coefficient versus temperature, separately for Vg trace (60→60) and retrace (-60→60) sweeps. Red and blue symbols correspond to electron and hole regimes. Filled and open symbols correspond to trace and retrace sweeps. b) Raman characterization of the same device showing the orientation of the black phosphorus flake with respect to the heater element. The A^2_g=A^1_g ratio shows that in this device thermoelectric transport was probed along the light effective mass direction. Similarly to the previous sample, 2D maps of the temperature dependence are shown for the electric response (V=50 mV) in c) (trace) and d) (retrace), and for the thermoelectric response in e) (trace) and f) (retrace). ...173

Figure 7- 1: Optical microscope images. a) After deposition of metal alignment markers to locate area of clean CVD graphene. b) After patterning of etch mask to define the final device

channel. c) After liftoff of etch mask resist in acetone. d) After patterning of device electrodes for MgO and Co depositions. Scale bar is 20 µm. 175

Figure 7- 2: a) Optical microscope image of etched bilayer graphene on BN substrate. b) Optical microscope image after second transfer of BN top gate. c) Optical image after complete device fabrication showing top and bottom gates. 176

Figure 7- 3: Optical microscope images of two different black phosphorus based thermoelectric device with lateral contacts for the measurement of Nernst effect. Scale bar is 20 µm. 176

Figure 7- 4: a) Photo-responsivity of device within energy range of 1-4 eV measured at source drain bias V_{SD}=0.1 V. b) Three-dimensional schematics of the device structure used to measure photo-response. c) Photo-responsivity in the ultraviolet regime as a function of source drain bias V_{SD}. 177

Figure 7- 5: Optical microscope image of a black phosphorus based non-local spin valve device with MgO and Co electrodes. Scale bar is 20 µm. 178

CHAPTER 1 INTRODUCTION

1.1 SPINTRONICS

Spin electronics[3] or simply spintronics is a fast evolving technology that utilizes the intrinsic spin property of electron and its magnetic moment. Spintronics exploits the presence of non-equilibrium spin accumulations and encompasses the study of the electrical, optical and magnetic properties of materials affected by these spin populations. Overall, spintronics is the investigation of spin phenomena such as spin-orbit, hyperfine interactions and exchange interactions in a given system. A thorough comprehension of spin phenomena in different material systems enables us to understand the fundamental processes leading to spin relaxation and/or spin dephasing in metals, semiconductors and hybrid structures.

First experimental observation of the influence of electron spins on charge transport has been reported[4,5] even prior to the discovery of electrons by J. J. Thomson in 1897. Following this discovery, the topic of electron spins has gained much attention. The first important finding that has propelled spintronics studies is the discovery of anisotropic magneto resistance (AMR) by William Thomson (later known as Lord Kelvin); it was found that the resistance of a ferromagnetic metal depends on the relative angle between the driven charge current direction and the magnetization direction of the ferromagnetic metal[4–6]. Both the discovery of electrons and the establishment of quantum mechanics by Dirac in the early half of the 20th century[7], have led to the proposal of electron's intrinsic angular momentum by Uhlenbeck and Goudsmit in 1925; following the peculiar observations in line spectra of atoms[8]. This intrinsic angular momentum arises from spins interactions with magnetic field and it can be defined by quantized values of 1/2 or -1/2. These quantized values turn out to be of technological importance since it can be implemented in a similar fashion as the Boolean logical operations which is based on binary numbers 0 and 1. Since then a new era of electronics has begun which

focuses on the spin degree of freedom of electron for accomplishing spin based electronics applications[4,9,10]. With spintronics, the possible applications varies from simple spin field effect transistors (s-FETs)[11], magnetic random access memories (MRAM)[12] to novel and niche topological quantum computations[9].

There are a number of obstacles to overcome before we could successfully utilize the spin degree of freedom for electronics applications: 1) introducing and receiving information: the injection of spin polarized current into the system of interest such as metals and semiconductors and the detection of this spin polarized current and 2) information transporting: an ideal channel system which can preserve the injected spins and thus possesses long spin relaxation length/time[3]. One of the possible approaches for the introduction of spins was proposed by Aronov and Pikus in 1976. They introduced the idea of electrical spin injection as a method to generate non-equilibrium spin accumulation in non-magnetic systems[13,14]. Approximately a decade later, the electrical spin injection in metals was demonstrated by Johnson and Silsbee in 1985 in a system of single crystal aluminum[15–17].

Even with the promise of potential applications, the field of spintronics remained to be a field of research for fundamental science studies only. However a few years later, in 1988-89, two independent researchers, Albert Fert in France and Peter Grünberg in Germany have discovered the phenomenon of giant magneto resistance (GMR) in a configuration of ferromagnetic/non-magnetic metal/ferromagnetic heterostructure[18,19]. This discovery has earned them the Nobel Prize in Physics in 2007. GMR refers to the effect whereby the relative orientation of the magnetization in the ferromagnetic metals will determine the total electrical resistance of the heterostructure. The relative change of the resistance between parallel (magnetization directions of both ferromagnetic metals are along the same direction) and anti-parallel (oppositely magnetized ferromagnetic metals) configurations of the ferromagnetic layers could be > ~100 %. This is in fact the first technological breakthrough for spintronics

studies; GMR based magnetic read heads were designed to be employed in commercially available hard drives. The GMR based magnetic read head is the pioneer application and remains the leading technological discovery of spintronics till date.

The promising invention based on GMR also prompted renewed interests to expand spin transport studies in semiconductor heterostructure systems. Tunneling magneto resistance (TMR) in magnetic tunnel junctions which resembles the GMR (tunneling oxide in place of the non-magnetic metal) has been discovered[20,21]. Following that electrical charge injection of spins into non-magnetic systems (metals and semi-conductors) by a four terminal non-local technique has been demonstrated. This is in fact the non-local lateral spin-valve configuration that will be discussed in detailed later on in chapter 2[22–25]. The next stage of spin transport studies is the generation of non-equilibrium spin accumulations in metallic and semiconductor systems by the spin Hall and inverse spin Hall Effects[26–29]. Increasing interests of spin transport in semiconductor systems can be attributed to their fundamental physical properties; 1) the existence of a band gap allows the injection and detection of spins via optical methods (observation of spin Hall Effect in GaAs by optical Kerr rotation technique[28]) and 2) spin relaxation length in semiconductor systems due to their weak intrinsic spin-orbit interaction strength as compared to metallic systems. Persisting efforts have been placed to continuously seek the ideal system in which spin-orbit coupling can be manipulated where desired without significantly jeopardizing the spin relaxation length.

Researchers begin to introduce spintronics studies in organic conductors such as carbon nanotubes[30] and most recently graphene[31]. Carbon with an atomic number of 6 possesses weak intrinsic spin-orbit coupling and hence, the spin relaxation mechanism in carbon derivatives due to spin-orbit interaction is also weak[32]. Theoretical investigations have shown that the spin relaxation length in the order of ~100 μm can be realized in these systems[33,34]. Another advantage of these systems is they provide a possible platform for easy structural/chemical

modifications. These carbon derivatives can be engineered with chemical dopants such as hydrogen and fluorine[35] and also by deposition of metallic atoms[36] to enhance spin properties where desired. In the first part of the thesis I will concentrate on spin transport studies in graphene. I will demonstrate the spin Hall Effect in such modified graphene based devices. Experimental efforts have been focused to understand the origin of this effect and the externally induced spin-orbit coupling.

Another important question to address in spintronics would be the studies of spin transport in low dimensional system with an energy band gap. Graphene is a zero band gap semimetal and as a result it is deemed to be unattractive for any transistor applications. In view of this, we have shifted our attention to black phosphorus, which has recently joined the family of two-dimensional crystals. Within the layers of black phosphorus crystals, each phosphorus atom is covalently bonded to three adjacent phosphorus atoms depleting all its valence electrons to form a puckered lattice. Therefore, in contrast to graphene, black phosphorus has a direct energy band gap that persists from single layer ~2.0 eV up to bulk ~0.3 eV; spin studies in black phosphorus are interesting not only in terms of technological but also on scientific point of view. However, I have failed in the experiment of spin injection and detection in black phosphorus due to the following reasons: 1) Lower mobility of black phosphorus as compared to graphene and 2) surface degradation of black phosphorus. Due to the latter, various metal contacts (chromium, titanium, gold, copper-nickel, cobalt) have been employed in order to optimize the contact resistances of black phosphorus devices before any attempt of spin injections which is extremely sensitive to the surface preparations. Initiated by these studies and driven by the recent theoretical report of thermopower in black phosphorus, we have revealed a huge thermoelectric response in this system. I shall give a brief introduction of this field in the subsequent sub-chapter.

1.2 THERMOELECTRIC

Thermal electric or simply thermoelectric is a branch of physical study that encompasses all of Seebeck, Peltier and Thomson effects. The thermoelectric effect is the direct conversion of temperature bias/difference/gradient between two points/materials into electrical voltage and vice versa. Thermoelectric process is a thermodynamically reversible process whereas for Joule heating it is an irreversible process which occurs when an electrical charge current is driven through a resistive material. In a thermoelectric device, electrical voltage can be generated if there is a presence of temperature gradient from waste heat. On the contrary, a temperature difference can be created by applying a voltage across the thermoelectric device; for cooling or heating application. In the atomic scale, a heat gradient causes the charge carriers to diffuse from the hotter end to the colder end.

In 1821-1823, Thomas Johann Seebeck first observed the phenomena of Seebeck effect; he noticed that in his circuit composed of two distinct metals with junctions at different temperatures would deflect a compass magnet[37]. Initially he thought this effect was due to magnetism induced by the temperature gradient and it is related to the Earth's magnetic field. Later on, he realized that it was actually the induced electrical current which according to Ampere's law would deflect the magnet. More specifically, the temperature bias produces an electrical potential which can drive electrical current in a closed circuit. This effect is known today as Seebeck effect. The voltage generated is proportional to the temperature difference through the Seebeck coefficient or thermopower. Around three decades later, Gustav Magnus observed that this induced voltage is invariant to the temperature distribution along the metals in between the junctions; this indicated that thermopower is a transport coefficient which later forms the basis for a thermocouple for temperature measurements.

In 1834, a French physicist Jean Charles Athanase Peltier independently found that an electrical current would produce heating or cooling effect at the junction of two dissimilar

metals. Few years later Lenz showed that depending on the current direction, the junction can actually be heated (to melt ice) or cooled (to freeze water). The heat absorbed or generated at the junction is found to be proportional to the current and the proportionality constant is known as Peltier coefficient.

Two decades later, William Thomson published an extensive explanation for both Seebeck and Peltier Effects and explained their inter-relations through Kelvin relations[38]. The Peltier coefficient is simply the multiplication of Seebeck coefficient with absolute temperature. From his derivations, he discovered the third thermoelectric effect which is the Thomson Effect; heat can be generated or absorbed when current is driven into a material with a temperature difference. The heat is proportional to both current and temperature difference with the proportionality constant given by Thomson coefficient.

In 1909, Altenkirch was the first who used these models to derive a maximum efficiency for thermoelectric generator[39] and this later on has been developed into the figure of merit ZT that we know today. Within this figure of merit, a good thermoelectric material should possess large Seebeck coefficient, low thermal conductivity to minimize heat loss and large electrical conductivity to minimize Joule heating. Following this, Eucken and Kuhn found that thermal conductivity can be significantly reduced in a defected allow system[40]; this method has since became an important strategy in improving thermoelectric materials.

In the early stage, thermoelectricity was actively studied for application in valuable technologies, primarily cooling as well as power generation for military. By the 1950's, efficiencies of thermoelectric generators had reached ~5 % and has eventually led to viable industries[41]. However a decade later the progress of thermoelectricity had slowed due to discussion that the upper limit of ZT might be ~1 and many research labs were discontinued.

In 1949, it was Abram Fedorovich Ioffe who developed the modern theory of thermoelectricity by introducing the concept of the figure of merit ZT[42,43]. Ioffe also

encouraged the application of semiconductors in thermoelectrics. Materials with high ZTs are typically heavily doped semiconductors; such as the tellurides of antimony, bismuth and lead. Ioffe actively pursued thermoelectric research and development in Russia leading to some of the first commercial thermoelectric power generator devices.

The search for high ZT materials continues with a strategy to look for small band gap semiconductors made from heavy elements. In his handbook, Glen Slack summarized the material requirements with the "phonon-glass electron-crystal" concept; phonons should be disrupted like in a glass but the electrons should have high mobility like they do in crystalline semiconductors[44].

Research in thermoelectricity has been revitalized in the 1990's due to input of new ideas with the hope that engineered system will improve ZT[45]; some of these ideas had created an entirely new class of complex thermoelectric materials[46]. The worldwide need for clean renewable energy sources has revived interest in commercial applications and in developing cost and environmentally friendly thermoelectric materials. Recently, there has been a theoretical prediction suggesting that black phosphorus subjected to appropriate doping could be a good thermoelectric material with high thermopower[47]. In this thesis, I will report on the first giant thermoelectric response of few layer black phosphorus due to phonon-drag mechanism which has also been used to describe the thermopower observation in other semiconductors.

Now, thermoelectric device/technology has been actively used in vast field ranging from; 1) modern electronics, thermoelectric is used to reduce high energy waste as heat which leads to excessive heating and failure in microprocessors, 2) full efficiency in automobiles, recycling waste heat to increase performance efficiency, 3) energy cost in industrial processes which include heating elements, 4) solar cells efficiency, increasing its efficiency from lower frequency solar radiation (heat), 5) consumer products, such as portable coolers and climate

controlled jackets and 6) niche application such as thermoelectric generators for space explorations.

1.3 THESIS OUTLINE

The focus of this Ph.D. thesis is to explore the spin transport studies in two-dimensional materials in particular graphene and black phosphorus. Specifically in the case of graphene, we studied the spin transport properties under the enhancement of spin orbit coupling in this system. We have developed a new spin injection technique based on spin Hall Effect in modified graphene (chemically/adatom dopants). Our discovery is of technological interest because we have shown an independent method of introducing and detecting of spin accumulation without the need of any ferromagnetic elements and tunneling oxides in our device architecture/configuration/geometry. This is in contrast with the previous spin transport studies in graphene which rely heavily on ferromagnetic contacts and tunneling oxides for the injection of non-equilibrium spins.

With black phosphorus, our aim was to study the spin transport with the presence of an energy band gap. However our initial efforts on spintronics studies have not been rewarding due to the complication stated above. Beginning with charge transport characterization and contact resistance optimization, these initial experiments have led us to an unexpected discovery. We reported the first giant thermoelectric response in this system. Encouraged by this, we study the thermoelectric properties, by first systematically studying the temperature dependence of its Seebeck coefficient to unearth the underlying mechanism that governs the characteristics of this material. In this system, phonon-drag mechanism is used to describe the observed giant thermopower. From our observations and also confirmed by recent theoretical predictions, black phosphorus is indeed a wonder thermoelectric material. Black phosphorus has the highest

ever measured thermopower among other two-dimensional materials, and figure of merit ZT~2.1 approaching the state of the art value for hybrid nanostructures.

Chapter 2: Introduction on the two-dimensional materials explored in this thesis; graphene and black phosphorus. This is followed by basic concepts essential for understanding the spin transport in non-magnetic materials; conventional non-local spin valve, spin-orbit coupling studies and spin Hall Effect will be introduced. This chapter will close with basic concepts on thermoelectric in particular Seebeck-Peltier-Thomson Effect and heat transport in metallic and semiconducting systems.

Chapter 3: This chapter concentrates on the basic experimental techniques needed to perform the various experiments on graphene and black phosphorus; from device fabrications to different charge and spin measurement setups.

Chapter 4: First result of spin Hall Effect in weakly hydrogenated graphene will be presented. Spin-orbit interaction in graphene is enhanced by chemically modifying graphene lattice with hydrogen atoms. This work was published with me as an equally contributing co-author (see List of Publications (9)). I extended this experiment to study also the spin Hall Effect in semi-ionic fluorinated graphene (see List of Publications (1)), a novel fluorination technique that we have published previously (see List of Publications (8)).

Chapter 5: First experimental observation of spin Hall Effect in graphene is followed by the discovery of giant spin Hall Effect in graphene grown by CVD and metallic adatoms decorated graphene. This work was published with me as an equally contributing co-author (see List of Publications (6)).

Chapter 6: First experimental observation of thermoelectric response in black phosphorus. Our results show that black phosphorus can be incorporated into thermoelectric devices with figure of merit approaching state of the art value ZT~2.1 (see List of Publications (2)).

Chapter 7: Summary and outlook for future experimental work on graphene spintronics, black phosphorus thermoelectric, black phosphorus photodetector (see List of Publications (3)) and black phosphorus spintronics.

CHAPTER 2 BASIC CONCEPTS

In this chapter I shall discuss on the fundamentals of graphene and black phosphorus, which will be the heart for each of the experiment/application discussed later on. I shall begin with a brief introduction, electronic band structure and key electronic properties of graphene followed by black phosphorus. Afterwards, I will give a brief account of the basic theory of electrical spin injection and detection (spintronics), basic concepts on spin-orbit coupling, theories on spin Hall Effect and followed by rudimentary properties of graphene that are significant for spintronics studies. Spin transport in the diffusive regime under Boltzmann theory will be discussed. Noteworthy to say that we are the pioneer in the experimental demonstration of spin Hall Effect in graphene; as shown in chapter 4 and 5. This is followed by discussion on concepts of thermal transport and application of thermoelectric in two-dimensional materials. We achieved state of the art figure of merit performance for the work we shown on black phosphorus. The following works were referred extensively and applied as guide in preparing this chapter: 1) F. J. Jedema PhD thesis, 2) N. Tombros PhD thesis, 3) D. Cooper et al. "Experimental review of graphene", 4) J. Balakrishnan PhD thesis, 5) A. Avsar PhD thesis.

2.1 GRAPHENE

2.1.1 INTRODUCTION

Graphene is an atomically thin hexagonally arranged two-dimensional array of carbon atoms[48–51]. Graphene is known as mother of all other carbon allotropes and thus it is vital for us to understand some of the fundamental remarkable properties of graphene:

1) Carbon has a low atomic number of 6; spin-orbit coupling in graphene is insignificant and thus would permit long distance spin transport in the order of micrometers even at room temperature.

2) Atomically thin, extremely large Young's modulus[52] and low bending rigidity[53]; graphene portrays itself as a perfect material both structurally and electronically for modifications (chemical and structural), thus allowing creation of new magnetic or superconducting systems.

3) At low energy, the carriers are massless Dirac fermions; under low energy excitations, graphene system imitates quantum electrodynamics physics for massless fermions.

2.1.2 ELECTRONIC STRUCTURE

Many of graphene remarkable properties including its band structure are due to its crystal structure; carbon atoms hexagonally arranged in a two-dimensional plane with a distance of 1.42 Å from its three nearest neighbors. Each of the carbon atom shares a σ bond with its three nearest neighbors and a fourth π bond perpendicularly oriented out of plane. This π orbital is often depicted as a pair of symmetric lobes oriented along the z axis with the carbon nucleus as the center. Every carbon atom on the two-dimensional plane has one of this π bond and each of them will contribute to form π band and π^* band. It is precisely these hybridized bands which cause most of the exotic electronic properties of graphene.

The hexagonal lattice of carbon atoms can be seen as two overlapping triangular lattices (see Figure 2-1). Electronic band structure is often studied by exploring the relationship between energy and momentum of the electrons within the system. Since our system is limited to two dimensions, the momentum space is also constrained to two dimensions.

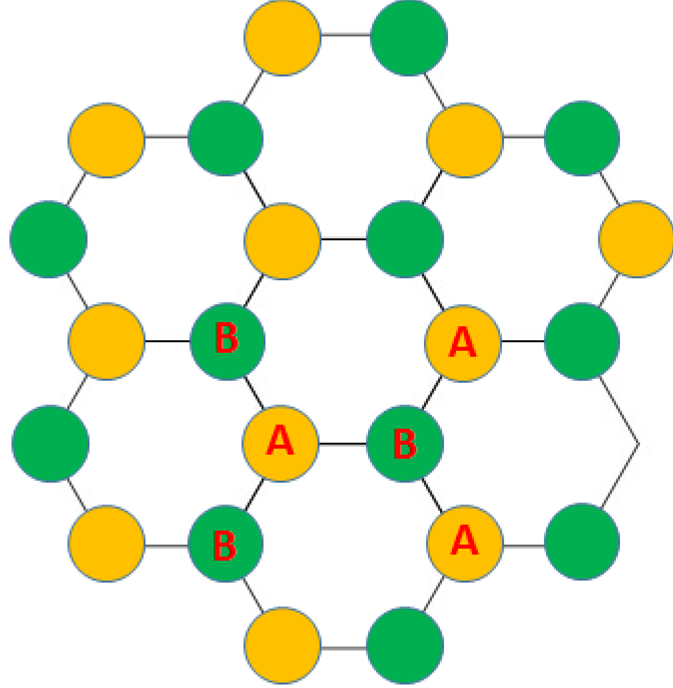

Figure 2- 1: The hexagonal lattice of carbon atoms showing carbon atoms on site A and B. The lattice can also be seen as two overlapping triangular lattices.

Graphene's band structure was first studied in 1947 by Wallace[49], by using tight binding model. The Hamiltonian of graphene system is given by the following expression[54]:

$$H_K = \begin{pmatrix} E_A & te^{i\boldsymbol{k}.\boldsymbol{a_1}} + te^{i\boldsymbol{k}.\boldsymbol{a_2}} + te^{i\boldsymbol{k}.\boldsymbol{a_3}} \\ C.C & E_B \end{pmatrix}. \tag{2.1}$$

Here E_A and E_B are the energies of carbon atoms on site A and B respectively as shown in Figure 2-1, t is the hopping energy between the nearest neighbor atoms, $\boldsymbol{a_1}=a(1,0)$, $\boldsymbol{a_2}=a(-0.5,\sin(\pi/3))$ and $\boldsymbol{a_3}=a(-0.5,-\sin(\pi/3))$ are the coordinates of the nearest neighbors and finally $C.C$ is the complex conjugate of the off diagonal matrix element. The eigenvalues for this Hamiltonian is as depicted in Figure 2-2 as a function of $\boldsymbol{k}=(k_x,k_y)$ whereby the z-axis corresponds to the energy and the horizontal plane axes represent the momentum space in the lattice system.

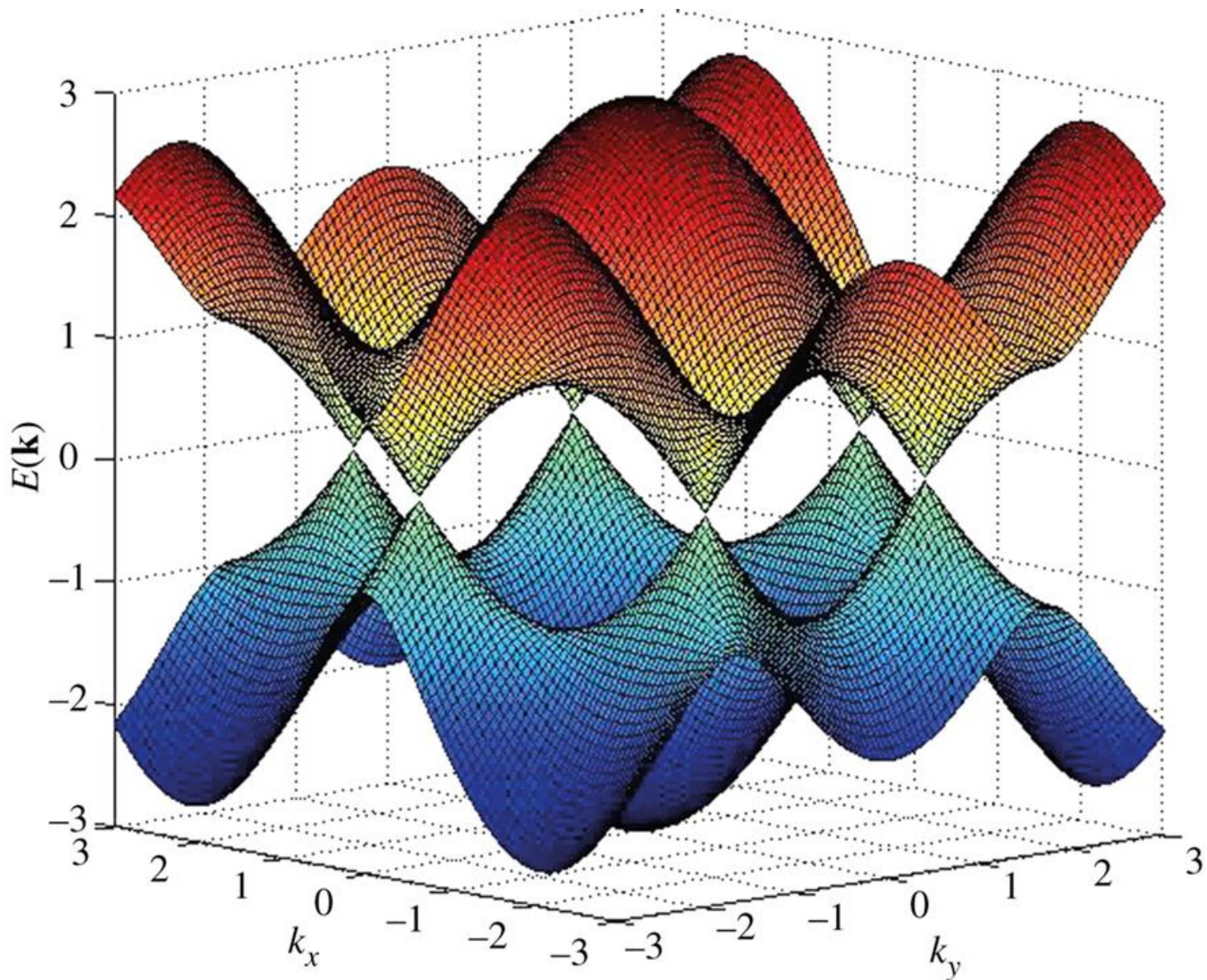

Figure 2- 2: The first Brillouin zone of graphene (adapted from Vozmediano[55]).

From the first Brillouin zone, as shown in the horizontal plane axes, we can see that the valence and conduction bands converge at a single point. These converging points are the K and K' points, and they are known as Dirac points (locations in momentum space on the edge of Brillouin zone). Graphene is a zero band gap semiconductor because the conduction and valence bands intersect at the Dirac points. In this first zone, there are two inequivalent groups of three Dirac Points and thus creating a valley degeneracy of $g_v=2$.

By inspecting closely at the region near one of the Dirac points (K or K'), the linear dispersion relation between and energy and momentum is evident. The Fermi energy for an ideal graphene is exactly at the Dirac point and electrons within ~1 eV of the Dirac point have a linear dispersion relation which is well described by the Dirac equation for massless fermions.

In this case, the effective mass of the carriers is zero and dispersion relation in the vicinity of the Dirac point can be expressed as:

$$E_{\pm}(k) \approx \pm \hbar v_F |k - K|. \tag{2.2}$$

This dispersion relation corresponds to the spectrum of the Dirac like Hamiltonian for low energy massless Dirac fermions, again described in the sub-lattice A and B. If we expand the tight binding Dirac Hamiltonian of equation (2.1) close to K and K' with $\hbar v_F = 3ta/2$, we will obtain:

$$H_K = \hbar v_F \begin{pmatrix} 0 & k_x - ik_y \\ k_x + ik_y & 0 \end{pmatrix} = \hbar v_F \boldsymbol{\sigma}.\boldsymbol{k} \tag{2.3}$$

$$H_{K'} = \hbar v_F \boldsymbol{\sigma}^{*}.\boldsymbol{k}. \tag{2.4}$$

Here, $\boldsymbol{\sigma}=(\sigma_x,\sigma_y)$ is the two dimensional vector of Pauli matrices (σ^* is the complex conjugate of σ), $\boldsymbol{k}$ is the wavevector and v_F is the Fermi velocity given by 10^6 ms^{-1}. The charge carriers in graphene lattice act as relativistic particles with an effective speed of light given by the Fermi velocity which causes most of the fascinating aspects and research attention in graphene.

We will now briefly describe on the chirality of graphene. Transport in graphene shows a novel chirality where each sub-lattice can be considered to be responsible for one side of the dispersion. These dispersions interact very weakly with one another and the existence of this chiral effect can be characterized by a pseudospin quantum number for the charge carriers. We can think of this quantum number as a number analogous to charge carrier's spin but their independent of each other. This pseudospin allows us to differentiate the contributions from different sub-lattices. The chirality of graphene can be understood from the Pauli matrix contributions in the Dirac like Hamiltonian described above.

Charge carriers described in a Dirac Hamiltonian cannot be confined by electrostatic potentials. For conventional semiconductors, if an electron strikes an energy barrier which is greater than its kinetic energy, the wavefunction of the electron will become evanescent in the

barrier and decay exponentially with distance further away from the barrier. Therefore the higher and wider the energy barrier is, the lower the probability of the electron quantum tunnels through the barrier. In the case of particles described by Dirac equation, the transmission probability is opposite of the traditional scenario. For example, a Dirac electron that hits a high energy barrier will transform to hole and propagate through the barrier until it reaches the other side, where it will transform back into an electron. This peculiar phenomenon is known as Klein tunneling.

I will end this sub-chapter by summarizing some of the intriguing properties of graphene as compared to conventional two-dimensional semiconductors.

1) Graphene is zero band gap semiconductor while conventional semiconductors have a finite band gap. For graphene, the charge carrier changes at the Dirac point from an electron to hole (or vice versa), the Fermi level of graphene is always within the conduction band or valence band.
2) Dispersion in graphene is chiral.
3) The dispersion relation in graphene at low energies is linear while in conventional semiconductors it is quadratic. Most of the fascinating electronic properties of graphene can be regarded to be results of this fact.
4) Graphene is atomically thin ~3 Å while traditional two-dimensional electron gas in hetero-structure or quantum well tend to have thickness around ~tenths of nanometer.
5) Graphene has been experimentally found to have a finite minimum conductivity even in the situation of vanishing charge carriers[56,57].

2.1.3 ELECTRONIC PROPERTIES

Graphene demonstrates many exotic and fascinating electronic properties owing to its linear dispersion relation between energy and momentum at low energies. Graphene is a zero band gap semiconductor, direct consequence of the valence band and conduction band intersecting at Dirac point. While this is a hindrance in terms of transistor functions, this property allows us to continuously tune the charge carrier concentration and even changing the charge carrier from electron to hole (vice versa) at the Dirac point. Electrostatic field tunes the Fermi energy of graphene via the following equation[48]:

$$\varepsilon_F = \hbar v_F \sqrt{\pi n}\,. \tag{2.5}$$

Here n is the charge carrier concentration and it can be continuously tuned by applying an electrostatic back gate voltage through an oxide gate (throughout this thesis in all the work performed, SiO_2 gate is used):

$$n = \frac{\varepsilon_0 \varepsilon V_g}{te}\,. \tag{2.6}$$

Here t is the thickness of the oxide gate, $\varepsilon_0\varepsilon$ is the permittivity of the oxide and V_g is the applied electrostatic back gate. For an ideal graphene, the Fermi level is located at the Dirac point and the conductivity σ of graphene increases with the application of back gate voltage. Positive (negative) back gate voltage tunes the Fermi level into conduction band (valence band) increasing the density of electron (hole) charge carriers. Electronic charge mobility μ can be calculated from the Drude formula[58]:

$$\mu = \frac{\sigma}{en}\,. \tag{2.7}$$

The charge carriers in the graphene devices discussed throughout this thesis are governed by diffusive transport characteristics where there charge diffusion coefficient D is given by the Einstein relation as:

$$D = \frac{\sigma}{e^2 \nu(E)}\,. \tag{2.8}$$

In the case of two-dimensional graphene, the density of states $v(E)$ is related to energy E as[59]:

$$v(E) = \frac{2\pi g_v g_s |E|}{h^2 {v_F}^2} . \tag{2.9}$$

Here $g_s = 2$ and $g_v = 2$ are the twofold spin and valley degeneracies. Energy E can be calculated from the number of charge carriers with the following equation:

$$E = h v_F \sqrt{\frac{n(E)}{g_v g_s \pi}} . \tag{2.10}$$

Therefore the charge diffusion coefficient D is finally given by the relation below:

$$D = \frac{\sigma}{2e^2} \frac{h v_F}{\sqrt{g_v g_s \pi n(E)}} . \tag{2.11}$$

From the charge diffusion coefficient, we can now calculate the momentum relaxation time τ_p via the following equation:

$$\tau_p = \frac{2D}{{v_F}^2} . \tag{2.12}$$

For the case of graphene, (graphene devices based on single layer graphene were used in the first part of this thesis) the momentum relaxation time τ_p is thus given by:

$$\tau_p = \frac{\sigma}{e^2} \frac{h}{v_F \sqrt{g_v g_s \pi n(E)}} . \tag{2.13}$$

2.1.4 ELECTRONIC TRANSPORT UNDER MAGNETIC FIELD

Classically if a conductor is placed under an electric field and magnetic field, the charge carriers in the system will experience a Lorentz force given by:

$$\boldsymbol{F} = \pm e(\boldsymbol{E} + \boldsymbol{v} \times \boldsymbol{B}) . \tag{2.14}$$

Depending on their velocities and carrier types, they will be deflected to opposite edges of the system. In a standard Hall bar configuration, this accumulation of charges with opposite

polarity on different sides of the system creates a transverse potential V_{xy}. The transverse resistivity ρ_{xy} in this case depends linearly with the perpendicularly applied magnetic field B_z via the following equation:

$$\rho_{xy} = \frac{V_{xy}}{I_{xx}} = \frac{B_z}{ne} = B_z R_H \ . \tag{2.15}$$

This measurement is typically performed in conducting system to determine the type of charge carriers present in the material where R_H is known as the Hall coefficient. This Hall Effect measurement can also be performed at low magnetic field to extract the Hall mobility of a conducting material. The Hall mobility can be calculated as $\mu = \frac{R_H}{\rho_{xy}}$.

The longitudinal resistivity on the other hand is independent of B_z and it is related to the longitudinal resistance only by the channel dimensions.

$$R_{xx} = \frac{\rho_{xx} L}{W} = \frac{V_{xx}}{I_{xx}} \ . \tag{2.16}$$

2.2 BLACK PHOSPHORUS

2.2.1 INTRODUCTION

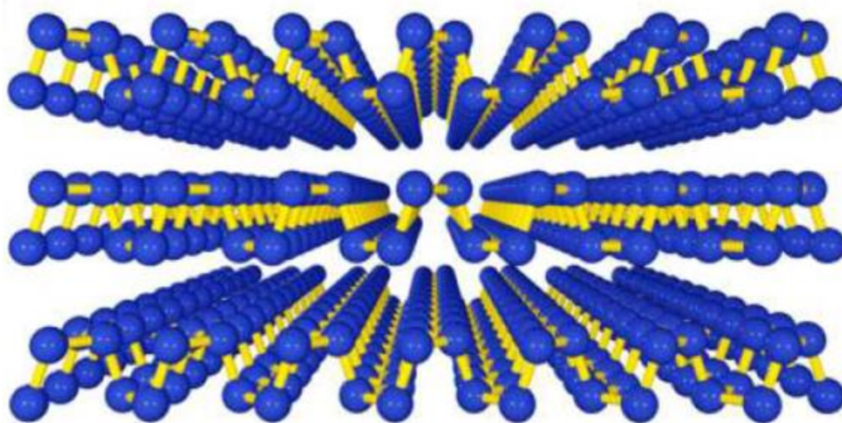

Figure 2- 3: Layered structure of black phosphorus with puckered honeycomb lattice (adapted from Liu et al.)[60].

Black phosphorus is a forthcoming two-dimensional material with vast potentials for industrial applications. Black phosphorus exhibits layered structure in which individual atomic thin layers are held together by weak van der Waals interactions much like in bulk graphite[61]. Within each layer, the phosphorus atom is covalently bonded to three adjacent phosphorus atoms exhausting all three valence electrons to form a rigged/puckered honeycomb lattice structure(see Figure 2-3)[62]. Therefore, unlike graphene, a single layer black phosphorus also termed as phosphorene is a semiconductor with a predicted direct band gap of ~2 eV at the Γ point of the Brillouin zone[63]. Black phosphorus has certainly became the leading two-dimensional material in present time due to the following:

1) Black phosphorus has a direct bandgap that persists from single layer up to bulk; the direct band gap reduces from ~2 eV for single layer down to ~0.3 eV for bulk.
2) Such a band structure provides a much needed band gap for application such as field effect transistor (FET) unlike graphene; the thickness dependent band gap can also lead to various potential optoelectronics applications.
3) Peculiar phase transitions observed in black phosphorus crystal structure; phase transition from semiconductor to metal[64] and superconductor at high pressure[65,66].
4) Highly anisotropic crystal structure of black phosphorus; optical and electronic properties of black phosphorus vary with orientation of crystal structure[60,67–69].

2.2.2 ELECTRONIC STRUCTURE

The energy band structure for black phosphorus was first calculated by Takao et al. in 1981 by using tight binding approach. Phosphorus can exist in many distinct allotropic modifications and it has been shown that phosphorus undergoes fascinating sequence of crystal structure transformation under high pressures. Black phosphorus changes from being a semiconductor to semimetal to metal as we increase the pressure. In its most

thermodynamically stable form at zero pressure, black phosphorus exhibits a layered structure made of rigged/puckered individual atomic layers.

As shown in Figure 2-3, assuming black phosphorus has a layered structure parallel to the x-y plane, the unit cell at the origin consists of four atoms which are located at:

$$\boldsymbol{\tau_1} = (uc, 0, vb),\ \boldsymbol{\tau_2} = -\boldsymbol{\tau_1},\ \boldsymbol{\tau_3} = \left(-[u-0.5]c, \frac{a}{2}, vb\right) \text{ and } \boldsymbol{\tau_4} = -\boldsymbol{\tau_3}\,. \tag{2.17}$$

Here a=3.314 Å, b=10.478 Å and c=4.376 Å are the lattice constants in orthorhombic system and u=0.08056 and v=0.10168 are crystal structure parameters[62]. In this structure, the first and second nearest neighbor distances (d_1=2.224 Å and d_2=2..244 Å) are very close to each other and bond angles β_1~96 ° (angle between two d_1) and β_2~102 ° (angle between d_1 and d_2) are very close to right angle[62]. This is a direct result of the primary bonding within each layer; the three covalent bonds of phosphorus atom due to the 3p-orbitals.

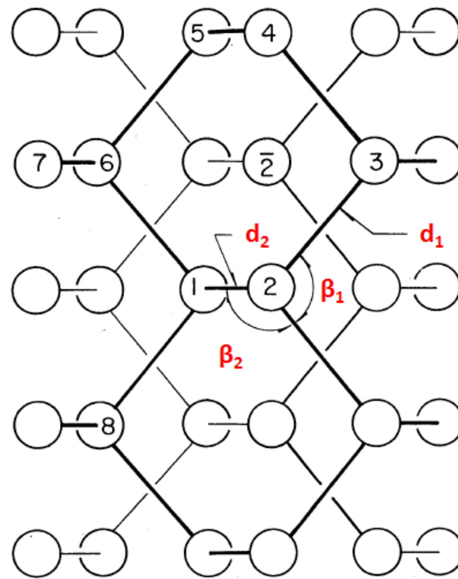

Figure 2- 4: Projection of two adjacent layers on x-y plane.

The projection of two continuous puckered layers on the x-y plane is as shown in Figure 2-4. The primitive translation vectors of the crystal are given by:

$$\boldsymbol{a_1} = c\hat{\boldsymbol{x}},\ \boldsymbol{a_2} = \left(\frac{a}{2}\right)\hat{\boldsymbol{y}} + \left(\frac{b}{2}\right)\hat{\boldsymbol{z}},\ \boldsymbol{a_3} = -\left(\frac{a}{2}\right)\hat{\boldsymbol{y}} + \left(\frac{b}{2}\right)\hat{\boldsymbol{z}}\,. \tag{2.18}$$

With this, the primitive cell, a parallelepiped which is edged by the primitive translation vectors consists of four atoms located at:

$$\pm(uc, 0, vb),\ \pm(uc, 0, -vb) + \left(\frac{c}{2}, 0, \frac{b}{2}\right). \tag{2.19}$$

The first three orders of nearest neighbor distance between successive layers are much larger than d_1 and d_2, showing that the bonding between two successive layers is of weak van der Waals' type. From Figure 2-5, the first Brillouin zone of black phosphorus is given by the bold sold lines and the light rectangle line shows the two-dimensional Brillouin zone of a single layer phosphorus.

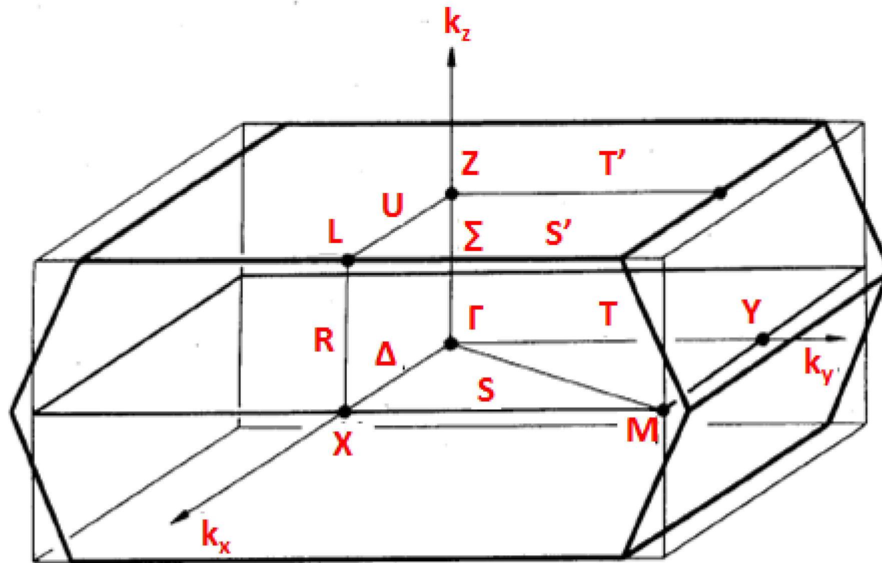

Figure 2- 5: First Brillouin zone of black phosphorus as given by the bold lines and the light rectangle line showing the Brillouin zone for a two-dimensional single layer black phosphorus.

Since the interlayer van der Waals force is weak, the electronic band structure of a single layer phosphorus can give a useful approximation for the band structure of bulk black phosphorus. The energy band structure can be obtained by solving the 16×16 secular equation:

$$\left|\left\langle\varphi_{ui}^{(\boldsymbol{k})}\middle|\boldsymbol{H}\middle|\varphi_{vj}^{(\boldsymbol{k})}\right\rangle - \varepsilon\left\langle\varphi_{vi}^{(k)}\middle|\varphi_{vj}^{(k)}\right\rangle\right| = 0 \tag{2.20}$$

where the Bloch sums for phosphorus 3s, 3px, 3py and 3pz within the layer are given by:

$$\varphi_{ui}^{(\boldsymbol{k})}(\boldsymbol{r}) = \left(\frac{1}{\sqrt{N}}\right)\sum_{l} e^{i\boldsymbol{k}.(\boldsymbol{l}+\tau_i)} \times \emptyset_u(\boldsymbol{r} - \boldsymbol{l} - \boldsymbol{\tau_i})\,. \qquad (2.21)$$

Here, i ranges from 1 to 4, u=s, x, y and z and $\emptyset_u$ is the atomic orbital. The matrix element of equation (2.20) can be evaluated by using Hückel method[70] for an eighth order nearest neighbor approximation. The calculated band structure for bulk black phosphorus by taking into account of the interlayer interactions is as shown in Figure 2-6 with the primitive cell consisting of 20 valence electrons occupying the lowest ten bands. The single layer black phosphorus is a semiconductor with a direct energy band gap at Γ of ~2 eV and for bulk black phosphorus the energy band gap reduces to ~0.3 eV at Z point.

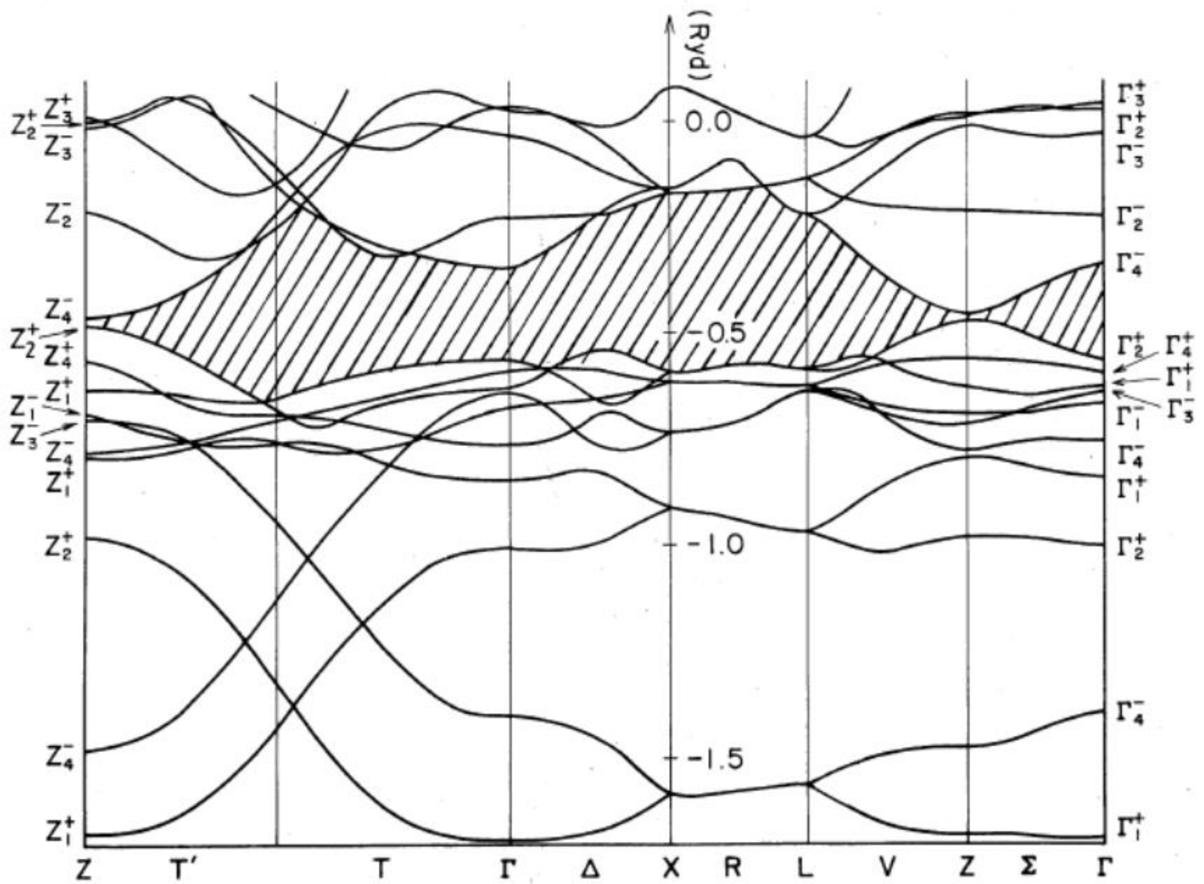

Figure 2- 6: Electronic band structure for bulk black phosphorus (adapted from Takao et al.)[63].

2.2.3 ELECTRONIC PROPERTIES

The calculated effective masses of charge carriers (electron and hole) are different for different directions[63]. The anisotropy of the effective masses reflects in the high anisotropic nature of black phosphorus physical properties. The calculated effective mass for hole is slightly larger than that of electron (m^* (hole)>m^* (electron)) but it has been found that black phosphorus is an intrinsic p-type semiconductor. Thus the deformation potential for electrons must be much larger than that of hole as to allow the intrinsic conduction to be of p-type. Figure 2-7 shows a typical transport behavior of few layers black phosphorus.

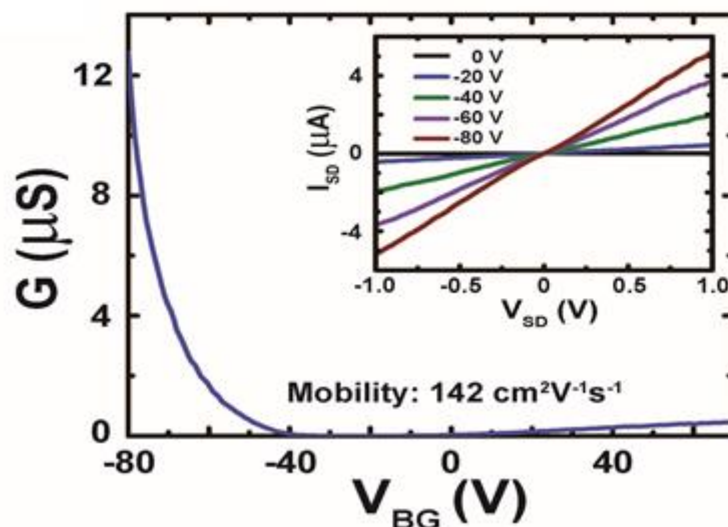

Figure 2- 7: Typical conductance of few layers black phosphorus as a function of back gate voltage with source drain voltage V_{SD}=0.1 V. Inset: I-V characteristics of the same junction with different applied back gate voltage.

2.3 SPINTRONICS

2.3.1 ELECTRICAL SPIN INJECTION AND DETECTION

The fundamental of electrical spin injection is by having non-equilibrium densities of the spin-up and spin-down currents. In the case of a ferromagnetic (FM) material, the Fermi velocity and density of states for spin-up and spin-down sub bands at the Fermi level are different. Therefore in a FM material, there are non-equilibrium spin-up and spin-down carriers with different conductivities[71–73]. In a one-dimensional system, the spin current density J is given by:

$$J_{\uparrow\downarrow} = \frac{\sigma_{\uparrow\downarrow}\partial\mu_{\uparrow\downarrow}}{e\partial x}\,. \tag{2.22}$$

Here $J_{\uparrow\downarrow}$ denotes the spin current density for spin-up and spin-down, $\sigma_{\uparrow\downarrow}$ denotes the electrical conductivity for spin-up and spin down carriers and $\mu_{\uparrow\downarrow}$ is the electrochemical potential for spin-up and spin-down. The electrical conductivity σ is related to diffusion coefficient D through the following relation:

$$\sigma_{\uparrow\downarrow} = e^2 N_{\uparrow\downarrow} D_{\uparrow\downarrow}\,. \tag{2.23}$$

Here $N_{\uparrow\downarrow}$ is the spin dependent density of states at the Fermi energy. The diffusion coefficient D is related to the mean free path l and Fermi velocity v_F via the equation:

$$D_{\uparrow\downarrow} = \frac{1}{2} v_{F\uparrow\downarrow} l_{\uparrow\downarrow}\,. \tag{2.24}$$

As before, $D_{\uparrow\downarrow}$ denotes the diffusion coefficient for spin-up and spin-down carriers, $v_{F\uparrow\downarrow}$ is the Fermi velocity for spin-up and spin-down carriers and $l_{\uparrow\downarrow}$ is the mean free path length for spin-up and spin-down carriers. With these equations, the total spin polarization of a FM material is defined by the following equation:

$$P = \frac{J_\uparrow - J_\downarrow}{J_\uparrow + J_\downarrow} = \frac{\sigma_\uparrow - \sigma_\downarrow}{\sigma_\uparrow + \sigma_\downarrow}\,. \tag{2.25}$$

Both the spin-up and spin-down current densities contribute to the total charge current, thus the total charge current density is given by:

$$J = J_{\uparrow} + J_{\downarrow}\,. \tag{2.26}$$

On the other hand, the net spin current is given by the difference between spin-up and spin-down current densities:

$$J_S = J_{\uparrow} - J_{\downarrow}\,. \tag{2.27}$$

With simple algebraic manipulation of equations (2.22), (2.25) and (2.26), the spin-up and spin-down current densities can be shown to be:

$$J_{\uparrow} = (1 + P)\frac{\sigma_{Total}}{2e}\frac{\partial \mu_{\uparrow}}{\partial x}\,, \tag{2.28}$$

$$J_{\downarrow} = (1 - P)\frac{\sigma_{Total}}{2e}\frac{\partial \mu_{\downarrow}}{\partial x}\,. \tag{2.29}$$

A quick inspection on these two spin current densities shows that indeed their different which means that a charge current that is driven through a ferromagnetic material will be spin polarized. At the interface of a ferromagnetic and non-magnetic material, this spin polarized current that arises from the charge current driven through the ferromagnetic material will create an accumulation of non-equilibrium spins in the non-magnetic material[15]. This accumulation of spins will decay exponentially with distance x away from the interface as described in the following equation:

$$\frac{D_S \partial^2 \Delta\mu}{\partial^2 x} = \frac{\Delta\mu}{\tau_S}\,. \tag{2.30}$$

In the equation above, D_s is spin diffusion constant, τ_s is spin relaxation time and $\Delta\mu = \mu_{\uparrow} - \mu_{\downarrow}$ is the electrochemical potential difference between spin-up and spin-down. This accumulated non-equilibrium spins can be detected via a second ferromagnetic material if the distance between injector and detector is less than that of the length where the non-equilibrium spin-up and spin-down currents exist. This length that we have described is commonly known as the spin relaxation length λ_s and is a key spin parameter in spintronics community. This spin relaxation length λ_s is defined as:

$$\lambda_S = \sqrt{\tau_S D_S}\,. \tag{2.31}$$

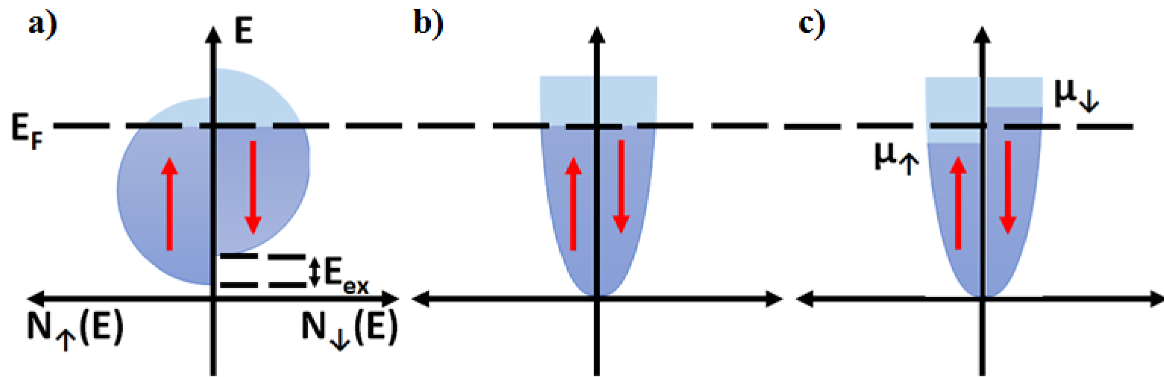

Figure 2- 8: Schematic illustration of the density of states in a) ferromagnetic material, b) un-polarized non-magnetic material and c) spin-polarized non-magnetic material.

Figure 2-8 shows the schematic illustration of the density of states of ferromagnetic material, un-polarized non-magnetic material and spin polarized non-magnetic material. Non-equilibrium accumulation of the spin-up and spin-down spins is created in the non-magnetic material due to an induced magnetization from the ferromagnetic material[74]. The accumulated spins at the interface travel in this non-magnetic material and will be detected by a second ferromagnetic material. The total measured resistance of such device made of two ferromagnetic materials connected with a non-magnetic channel depends on the relative polarization directions of the first/injector and second/detector ferromagnetic contacts. In general, two different configurations are possible; 1) parallel and 2) anti-parallel polarization configurations can be achieved by exploiting the shape anisotropy property of ferromagnetic materials. For this reason, ferromagnetic injector and detector contacts are usually assembled with different dimensions (width, thickness) in order to have different coercive fields for each of them[75,76]. Parallel and anti-parallel orientations of the injector and detector can be achieved by continuously sweeping the magnetic field in the direction of the easy axis of the ferromagnetic materials. In terms of device measurements, this will result in a resistance change (switch) since resistance in anti-parallel orientation of ferromagnetic contacts is higher as compared to the parallel orientation.

2.3.2 NON-LOCAL SPIN VALVE CONFIGURATION

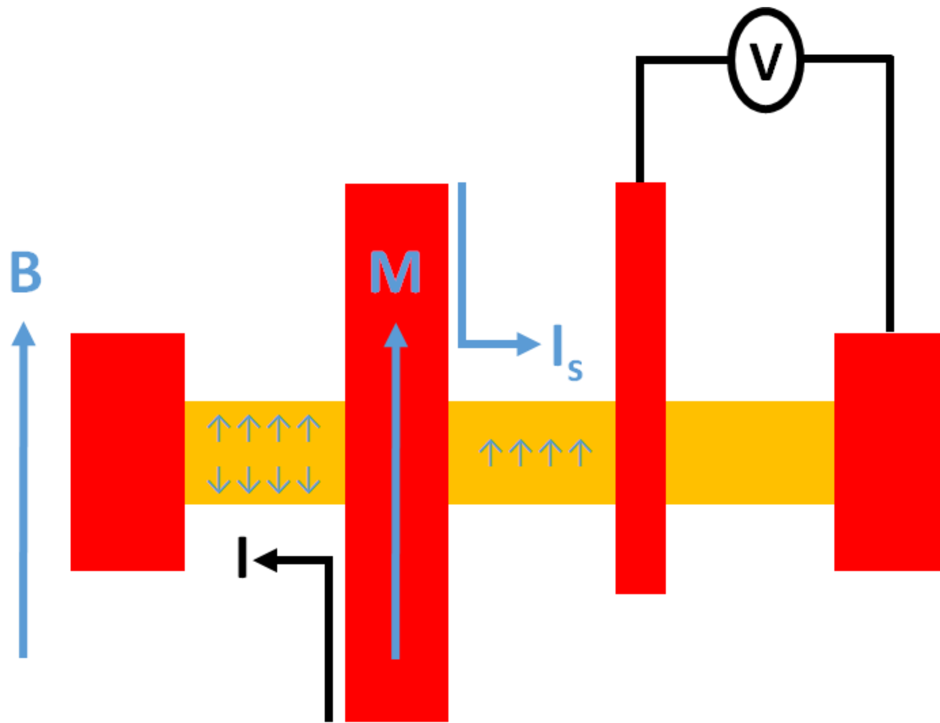

Figure 2- 9: Schematic diagram of a non-local spin valve geometry and measurement configuration. In this configuration, red contacts denote the ferromagnetic metal and yellow denotes the non-magnetic channel.

Following the previous sub-chapter, the configuration of ferromagnetic/non-magnetic/ferromagnetic can be employed to demonstrate at once spin injection, spin transport and spin detection phenomena. With this configuration, the charge and spin currents are not separated and they flow in the same path. Thus from a device point of view, the measured signal resistance includes the contribution from spin dependent resistance, contact resistance and also the non-magnetic material resistance. The percentage of the resistance due to spin to the total signal resistance measured is very small and this causes the measurements/observations of spin dependent transport to be almost impossible. Due to the charge and spin currents flowing in the same path, the spin signal measured cannot be separated

from many charge based phenomena such as Hall effect, interference effect and anisotropic magneto-resistance effect[31]. For us to measure pure spin resistance signal, a non-local spin valve configuration is used. Figure 2-9 shows the schematic of a non-local spin valve geometry and measurement configuration. In this device configuration which consists of four metal contacts with the two center ferromagnetic contacts acting as spin injector and detector. In this non-local configuration, a charge current is first driven from the injector ferromagnetic contact to the reference outer contact (the black arrow in Figure 2-9 represents the charge current direction). The charge current that is driven through the ferromagnetic contact is spin polarized upon reaching the interface with the channel. The accumulated spin current diffuses and decaying exponentially on both sides of the injector along the channel. With this measurement technique, we can create a pure spin signal since there is no net charge current flowing outside the channel between injector and outer reference contact. We can quantify this accumulated pure spin signal by measuring the spin dependent electrochemical potential via the ferromagnetic detector and the second outer reference contact. As discussed, the measured resistance signal depends on the relative polarization orientations of the injector and detector ferromagnetic metals. The polarization orientations of the injector and detector electrodes can be manipulated by sweeping an in-plane magnetic field along the easy axis of the contacts.

There are many drawbacks that prevent easy measurements of spin signal by using this technique, one of them is the spin injection efficiency. The injection efficiency depends on the relative conductivities of the ferromagnetic metal and the non-magnetic channel[77]. In order to have a more effective spin injection, the resistance of the interface between the ferromagnetic metal and non-magnetic channel has to be smaller than the resistivity of both ferromagnetic material and non-magnetic material with the resistivity of the two materials to be comparable. In the case of graphene acting as the non-magnetic channel, there is a huge mismatch between the conductivities of ferromagnetic material and graphene. To solve this, a thin Al_2O_3 tunnel

barrier was inserted by Van Wees' group at the interface between the ferromagnetic metal and graphene[31]. The introduction of Al_2O_3 tunnel barrier resulted in an increase of spin injection efficiency of up to ~10 %. Besides Al_2O_3, MgO can also be used as tunnel barrier for spin injection, motivated by the crystalline nature of MgO[78]. Graphene based non-local spin valves used in this thesis are made with MgO tunnel barrier.

A typical graphene-based non-local spin valve measurement is as shown later on in Figure 5-7 in chapter 5. The resulting spin signal depends on a number of parameters: 1) spin injection efficiency (P), 2) spin relaxation length (λ_S), 3) the interface area (A), 4) the conductivity of the channel (in the case of this thesis is graphene) (σ) and finally 5) the separation between injector and detector contacts (L) with the following equation[31]:

$$R_{NL} = \frac{P^2 \lambda_S}{2A\sigma} exp\left(\frac{-L}{\lambda_S}\right) . \tag{2.32}$$

The non-local pure spin resistance (R_{NL}) decays exponentially with the distance between injector and detector ferromagnetic contact. While A, σ and L are parameters that are known, P and λ_S are values that can be estimated from L dependence measurements.

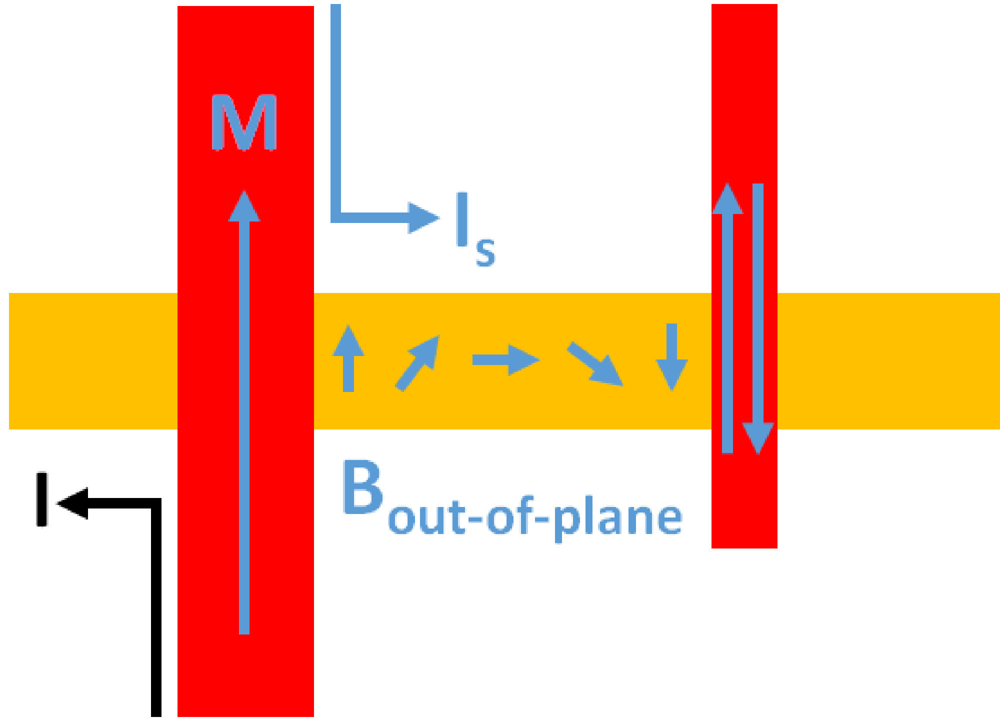

Figure 2- 10: Electrical spin precession of the injected spins under an applied out-of-plane magnetic field.

There is another way where non-local spin signal can be manipulated with an external applied magnetic field; that is through a perpendicularly applied magnetic field (see Figure 2-10). Previously, the applied magnetic field along the easy axis of ferromagnetic contacts (in-plane magnetic field) is used to polarize the magnetization orientations for the contacts. A perpendicular magnetic field will exert a torque on the spins and this creates an electrical spin precession with frequency given by:

$$\boldsymbol{\omega_L} = \frac{-g\mu_B \boldsymbol{B}_{\perp}}{\hbar}. \tag{2.33}$$

Here, μ_B is the Bohr magneton, $\hbar$ is the Planck constant and g is the Landé factor for electron. Similarly, the total non-local spin signal will show a maximum (minimum) resistance depending on whether the magnetization orientation of the injector and detector is parallel or anti-parallel before any application of perpendicular magnetic field. With an increasing perpendicular magnetic field, the total non-local spin signal will reduce (increase) to zero at

90 ° precession angle. However, in our graphene based non-local spin-valve, the transport characteristic is governed by diffusive transport. Thus while the spins are precessing, they are also decaying and relaxing, resulting in the damping of total spin signal at higher applied perpendicular magnetic field. The dynamics of the spins is given by the Bloch equation and it has the following form:

$$D_s \frac{\partial^2 \boldsymbol{\mu}}{\partial^2 x} - \frac{\boldsymbol{\mu}}{\tau_s} + \boldsymbol{\omega_L} \times \boldsymbol{\mu} = 0\,. \tag{2.34}$$

The first term in the Bloch equation describes the spin diffusion transport, the second term denotes the spin relaxation and finally the last term is the spin precession transport under a perpendicular magnetic field.

Figure 5-7 in chapter 5 shows a typical spin precession measurement of a graphene based non-local spin valve device. First of all, the magnetization directions of the injector and detector are made parallel (anti-parallel) to each other by applying an in-plane magnetic field along the easy axis of the contacts. Now by increasing the magnetic field in the perpendicular direction (perpendicular to the plane), the spin signal will decrease (increase) with a damping of the signal at higher magnetic field. The resulting curve can be fitted with the magnetic field dependence non-local signal to extract key spin parameters such as diffusion coefficient D_s, spin relaxation time τ_s and spin relaxation length λ_s via equation (2.35)[31]:

$$R_{NL} \propto \int_0^\infty \frac{1}{\sqrt{4\pi D t}} e^{\frac{-L^2}{4Dt}} e^{\frac{-t}{\tau_s}} \cos(\omega_L t)\, dt\,. \tag{2.35}$$

2.3.3 SPIN-ORBIT COUPLING

Spin-orbit interaction (SOI) or spin-orbit coupling (SOC) is an interaction of a particle's motion with its spin. It can be seen as the interaction between an electron's linear momentum with its spin angular momentum[79]. With this interaction, the electron spins can be

tuned/controlled/manipulated without the need for an external magnetic field. In addition with this coupling, strength of the interaction can determine the spin relaxation mechanism in the system. These are the fundamental principles for the realization of spin Hall Effect, which rely on the spin dependent scattering created by the enhanced SOC in the system. In this sub-chapter I will discuss briefly on the atomic picture of spin-orbit coupling followed by spin-orbit coupling in solids. Finally, some discussion on spin dependent scattering induced by this interaction as we prepared for the major work in this thesis in chapter 4 and 5 later on.

Atomic picture:

For electrons orbiting around a nucleus in an atom, the total energy of the system is given by its Hamiltonian H which consists of the electrons' kinetic energy due to the momentum of electrons and the electrons' potential energy due to the Coulomb interaction with the nucleus[71,79]:

$$H = \frac{\boldsymbol{p}.\boldsymbol{p}}{2m} - eV(r) = \frac{-\hbar^2}{2m}\boldsymbol{\nabla}.\boldsymbol{\nabla} - \frac{Ze^2}{r} \tag{2.36}$$

where m is the rest mass of electron and Z is the atomic number. Let us take Z=1 (hydrogen) for simplicity purpose. In the electron point of view (rest frame of electron), its orbital motion around nucleus can be seen as the nucleus orbiting around it with a velocity given by $\boldsymbol{v_n}=-\boldsymbol{p}/2m$. This orbital motion of nucleus produces a magnetic field that will be felt by the electron:

$$\boldsymbol{B_{SOC}} = \frac{\boldsymbol{v_n}}{c} \times \boldsymbol{E}(\boldsymbol{r}) = \frac{-e}{2mc}\frac{\boldsymbol{p}\times\boldsymbol{r}}{r^3}\,. \tag{2.37}$$

Interaction of the electron with magnetic moment $\boldsymbol{\mu_s}$ with this induced magnetic field is known as Zeeman interaction:

$$H_{SOC} = -\boldsymbol{\mu_s}.\boldsymbol{B_{SOC}} = \frac{e}{2mc}\boldsymbol{\mu_s}.\frac{\boldsymbol{p}\times\boldsymbol{r}}{r^3}\,. \tag{2.38}$$

Here the magnetic moment is given by $\boldsymbol{\mu_s}=-g\mu_B\boldsymbol{S}/\hbar$, where $\boldsymbol{S}$ is the spin angular momentum and $\boldsymbol{L}=\boldsymbol{r}\times\boldsymbol{p}$ is the orbital angular momentum. Finally H_{SOC} can be written as:

$$H_{SOC} = \frac{g\mu_B^2}{\hbar^2}\frac{\boldsymbol{S}.\boldsymbol{L}}{r^3} = \lambda_{SOC}\boldsymbol{\sigma}.(\boldsymbol{k} \times \boldsymbol{\nabla}V(\boldsymbol{r})) \tag{2.39}$$

This final form clearly shows the interaction of electron's motion (orbital angular momentum) with its spin (spin angular momentum) in vacuum and this is known as spin-orbit coupling where λ_{SOC}=-3.7×10^{-6} Å^2 is the vacuum spin-orbit coupling strength, $\boldsymbol{\sigma}$ is the Pauli spin matrices and $\boldsymbol{k}=\boldsymbol{p}/\hbar$ is the electron wave vector.

Let us now discuss briefly on how the SOC strength depends on the atomic number Z (we assumed Z=1 in the previous section). First of all, the Coulomb potential is proportional to Z and average value for the factor r^{-3} is proportional to Z^3. Thus from equation (2.37), the total spin-orbit interaction will depend on the atomic number as Z^4.

Spin-orbit interaction in solids:

Let us now generalized the discussion to include the interaction in solids. For a system without any magnetic impurities, the spin-orbit interaction in the system can be governed by the following equations[71]:

$$H_{SOC}(r) \propto \boldsymbol{\sigma}.\boldsymbol{B_{total}}(\boldsymbol{r}) \propto \frac{\boldsymbol{\sigma}.(\boldsymbol{p}\times\nabla V_{total}(\boldsymbol{r}))}{emc}\,. \tag{2.40}$$

In this system the total potential V_{total} is given by the summation of V_r (normal impurity potential) and V_{SOC} (spin-orbit potential). Here the total induced magnetic field B_{total} includes the contribution from impurities existing in the system and also the system band structure. Therefore we can attribute this effective induced magnetic field to two distinct mechanism: 1) extrinsic mechanism that arises from the impurities in the system and 2) intrinsic mechanism that arises from the spin related band structure of the system.

Extrinsic spin-orbit coupling:

In the extrinsic mechanism, the spin dependent scattering of electrons arises from the presence of impurities, defects or other artifacts in the system. This mechanism can be further classified into two different scattering types: 1) skew scattering and 2) side jump scattering.

Skew scattering:

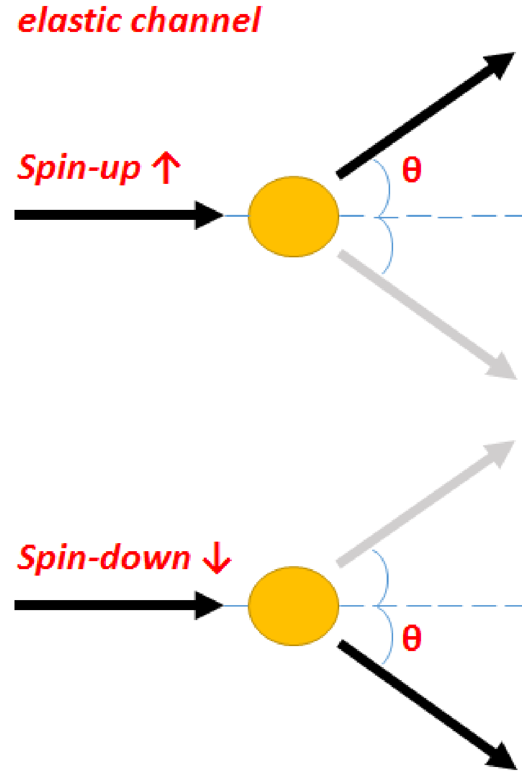

Figure 2- 11: Schematics showing the trajectory of spin-up and spin-down electrons after skew scattering process. The angle θ denotes the deflection angle of the electrons.

It was first studied by Nevil Mott back in 1929, the scattering of an incoming wave of electrons by nuclei[80]. It was shown that for an incoming spin polarized electrons, detectors placed at opposite sides of the incoming beam will measure different scattering rates. This investigation has provided an unambiguous evidence on the existence of electron's spin and is thus known as skew scattering[80,81]. For simplicity, this scattering can be understood from collision theory (electron-impurity collision). An electron moving through an impurity potential $V(\boldsymbol{r})$ with a velocity $\boldsymbol{v}$ experiences an effective magnetic field $\boldsymbol{B}_{eff}=-(\boldsymbol{v}\times\boldsymbol{E})/c^2$ in the rest frame of the electron. This spin-orbit induced magnetic field generates a spin dependent force which is given by the following equation:

$$\boldsymbol{F} = 2\mu_B \nabla(\mathbf{S}.\mathbf{B}) \tag{2.41}$$

From this equation, the force on one side will be slightly greater than the opposing side, thus leading to an orthogonal spin current. In this case, the rate of spin scattering is proportional to the rate of collision between the incoming electrons and impurities. In other words, the skew scattering resistivity is proportional to the Drude resistivity ($\rho_{skew} \propto \rho_{xx}$). Figure 2-11 illustrates the schematics for skew scattering mechanism where θ is the deflected angle of the electrons from with respect to their incoming path due to spin dependent scattering. Note that this scattering mechanism will not result in a charge separation in the orthogonal direction in a non-magnetic material due to the equal population of spin-up and spin-down electrons. However this spin accumulation in the orthogonal direction will lead to spin Hall Effect (SHE).

Side jump scattering:

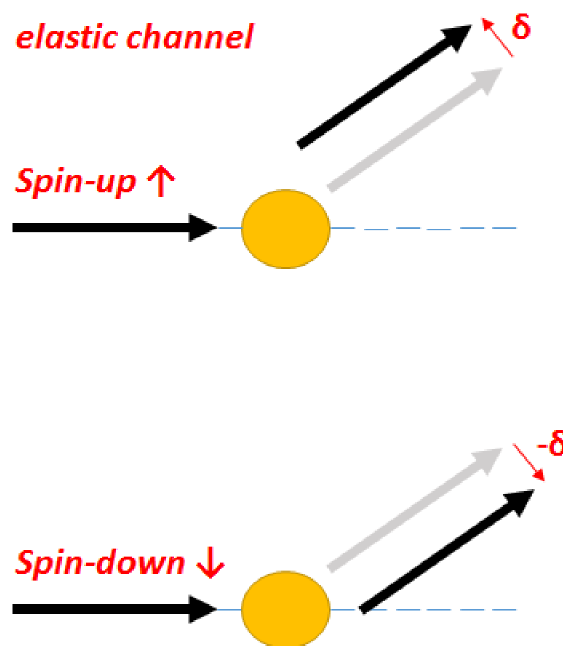

Figure 2- 12: Schematics showing the trajectory for both spin-up and spin-down electrons after side-jump scattering process. The vector δ denotes the sideway displacement for both spin-up and spin-down electrons.

Another extrinsic mechanism for spin dependent scattering is the side jump scattering first proposed by Berger back in 1970[82]. Figure 2-12 illustrates the schematics for a side jump

mechanism. The foundation of the side jump scattering mechanism is the anomalous velocity operator in systems with spin-orbit interaction. The center of mass of an electron wave packet will undergo a side way displacement upon collision with an impurity[83]. The Hamiltonian in this system can be expressed as[71]:

$$H = \sum_{k,\sigma} \varepsilon_k a_{k\sigma}^{\dagger} a_{k\sigma} + \sum_{k,k'} \sum_{\sigma,\sigma'} V_{totalk,k'}^{\sigma,\sigma'} a_{k'\sigma'}^{\dagger} a_{k\sigma} \ . \tag{2.42}$$

The first term denotes the kinetic energy term with electron energy ε_k and the second term is the total impurity potential. The impurity potential can be rewritten in the form:

$$V_{totalk,k'}^{\sigma,\sigma'} = V_{impurity}\left[\delta_{\sigma'\sigma} + i\lambda_{SOC}^{eff} \boldsymbol{\sigma}_{\boldsymbol{\sigma'\sigma}} . (\boldsymbol{k} \times \boldsymbol{k}')\right] \sum_i e^{i(\boldsymbol{k}-\boldsymbol{k}').\boldsymbol{r}_i} \ . \tag{2.43}$$

The velocity of the electron under the influence of this impurity potential can be expressed by using the operator equation whereby in the momentum space the operator for $\boldsymbol{r}$ is $i\boldsymbol{\nabla}_{\boldsymbol{k}}$:

$$\widehat{\boldsymbol{v}} = \frac{dr}{dt} = \frac{-i}{\hbar}\left[\widehat{\boldsymbol{r}}, \widehat{\boldsymbol{H}(\boldsymbol{k})}, \right] . \tag{2.44}$$

With this operator, we can now calculate the velocity by taking the matrix elements for the scattering states $|\boldsymbol{k}^{\dagger}\sigma>$:

$$\boldsymbol{v}_{\boldsymbol{k}}^{\sigma} = \langle \boldsymbol{k}^{\dagger}\sigma | \widehat{\boldsymbol{v}} | \boldsymbol{k}^{\dagger}\sigma \rangle = \frac{\hbar \boldsymbol{k}}{m} + \omega_{\boldsymbol{k}}^{\sigma} \ . \tag{2.45}$$

The second term in equation (2.45) is the anomalous velocity as discussed and is given by:

$$\omega_{\boldsymbol{k}}^{\sigma} = \frac{\lambda_{SOC}^{eff}}{\hbar} \sum_i \langle \boldsymbol{k}^{\dagger}\sigma | \boldsymbol{\sigma} \times \boldsymbol{\nabla} V(\boldsymbol{r} - \boldsymbol{r_i}) | \boldsymbol{k}^{\dagger}\sigma \rangle \ . \tag{2.46}$$

By integrating the equation (2.46) we can obtain the side jump displacement and the given displacement is along the direction of $\boldsymbol{\sigma} \times \boldsymbol{\nabla} V(\boldsymbol{r} - \boldsymbol{r_i})$. The direction of the displacement clearly depends on the spin and in this case the side jump resistivity varies quadratically with Drude resistivity ($\rho_{side\ jump} \propto {\rho_{xx}}^2$).

The difference in the Drude resistivity dependence of these two extrinsic mechanisms can be used to pin-point the dominant mechanism in a given system. In general skew scattering

mechanism dominates when the Drude resistivity is small and also at low temperatures and at low impurity concentration. As the Drude resistivity increases, the side jump mechanism starts to dominate, usually at higher temperatures and at higher impurity concentrations. Nonetheless in a real life experiment, both mechanisms may be present and the measured transverse resistivity would be a linear combination of both mechanisms:

$$\rho_{xy} = C_{skew}\rho_{xx} + C_{side\ jump}\rho_{xx}^{2}\ . \tag{2.47}$$

Intrinsic spin-orbit coupling (Dresselhaus and Rashba spin-orbit interaction):

Intrinsic spin-orbit coupling was first used to describe the observed anomalous Hall Effect in ferromagnetic system by Karplus and Luttinger in 1954[84]. This is known as the intrinsic effect due to its relation with spin dependent band structure of the system and this effect is strongest in system with inversion asymmetry. There are two distinct inversion asymmetry; 1) the Dresselhaus that arises from bulk inversion asymmetry and 2) the Rashba that arises from structural inversion asymmetry. In a two-dimensional system, the Hamiltonian for a linear interaction of Dresselhaus and Rashba can be expressed as:

$$H_{Dresselhaus} = \frac{\hbar^2 k^2}{2m} + C_{Dresselhaus}(k_x\sigma_x - k_y\sigma_y) \tag{2.48}$$

$$H_{Rashba} = \frac{\hbar^2 k^2}{2m} + C_{Rashba}\left(k_x\sigma_y - k_y\sigma_x\right) \tag{2.49}$$

It is important to note that for Rashba interaction, the induced effective magnetic field $\boldsymbol{B_{eff}}$ is perpendicular to $\boldsymbol{k}$. On the other hand for Dresselhaus interaction, the effective magnetic field has a non-straightforward dependence.

2.3.4 SPIN HALL EFFECT

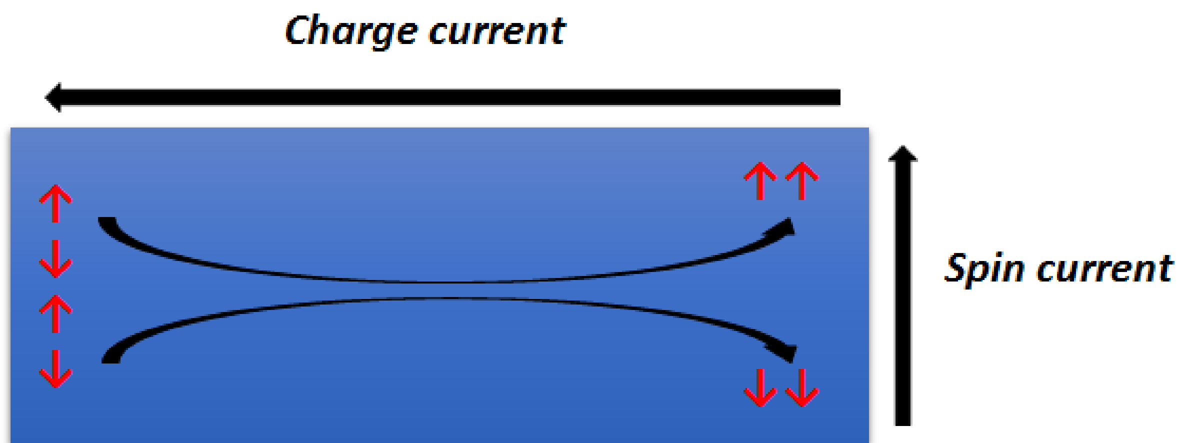

Figure 2- 13: Schematic showing the orthogonally aligned charge and spin currents; the longitudinal charge current induces a transverse spin current under spin Hall Effect due to an accumulation of spin-up and spin-down electrons on the opposite sides.

In the previous sub-chapter, we have discussed briefly the spin-orbit interaction in solids which can introduce spin dependent scattering of electrons. Two main physical phenomena that can be attributed to spin-orbit interactions in solids; 1) the anomalous Hall Effect (AHE) that occurs in ferromagnetic materials[85,86] and (2) the spin Hall Effect (SHE) in paramagnetic materials[26,27]. These Hall Effects could be due to the extrinsic spin-orbit interactions (skew scattering mechanism or/and side-jump scattering mechanism) or the intrinsic spin-orbit interactions which arise due to the spin dependent band structure contribution. In chapter 4 and 5 of this thesis, extensive work on SHE has been performed on graphene based hall bar devices. Thus we will focus on the discussion of SHE in paramagnetic systems in this sub-chapter. In a paramagnetic system, an un-polarized charge current will flow under an applied electric field. Due to the spin-orbit interaction, this applied electric field creates a spin Hall current in the orthogonal direction and causes spin accumulation in the paramagnetic system in a direction perpendicular to the charge current (see Figure 2-13).

The idea of manipulating/separating/orienting the spins with an electric field (SHE) was first discussed theoretically by M. I. D'yakonov and V. I. Perel in 1971[26] and later separately by Hirsch in 1999[27]. However not until recently, the first experimental measurements of SHE have been reported. In 2004, Kato et al. demonstrated the first experimental results of SHE in n-doped GaAs and InGaAs thin films[28]. In this work, the detection of the spin accumulation was achieved by optical Kerr rotation spectroscopy. The key message from this experiment is, with their observations, they clearly demonstrated that the spin Hall Effect observed in the strained films depended weakly on the crystal orientations and proposed the significance of extrinsic spin-orbit interaction for the observed SHE. After this pioneer work, SHE was also observed in p-doped GaAs using an electroluminescence method[29]. In this case the observed SHE was attributed to intrinsic spin-orbit interaction since the effect varies weakly on the defects of the system. Following these findings, SHE in n-doped GaAs[87] and n-type ZnSe[88] have been demonstrated by the pioneer group.

For detection of SHE in metallic systems where the spin relaxation length is much shorter, the optical methods utilized in semiconductors are not ideal. Large optical beams with spot sizes in the order of micrometers are unable to resolve the spins accumulation because in a metallic system the spin relaxation length is typically in the order of tens of nanometer. For metallic systems we have to rely on the inverse spin Hall Effect; as the name suggests, it is directly the opposite of SHE, where the spin current induces an orthogonal un-polarized charge current which can then be detected as a Hall voltage.

Here we will re-visit again the two common methods of injecting spins into a metallic system and detection by the inverse SHE. The first method is spin injection by using a magnetized ferromagnetic metal. This method has been described previously in the non-local spin valve sub-chapter. The device configuration is as shown in Figure 2-14. The spin polarized current from the ferromagnetic contact (charge current driven through a ferromagnetic material

will be spin polarized) diffuses into the non-magnetic metal and as a consequence there will be an electrical voltage generated due to the inverse spin Hall effect in the adjacent pair of contacts. This observation/measurement was first demonstrated in non-magnetic system aluminum by Valenzuela and Tinkham[15,89–91].

The second method that we will introduce is by having the configuration of non-local H-bar geometry which will be used extensively throughout the thesis. In this configuration, the spin current is first generated by the spin Hall Effect (as discussed above) and the detection of the introduced spins in the non-magnetic material is achieved by the inverse spin Hall effect (see Figure 2-15)[92–94]. In this case, the injected spins will subsequently create an un-polarized orthogonal charge current that can be detected in the adjacent pair of contacts. These measurements have been demonstrated by Molenkamp's group in system of HgTe quantum wells[95,96].

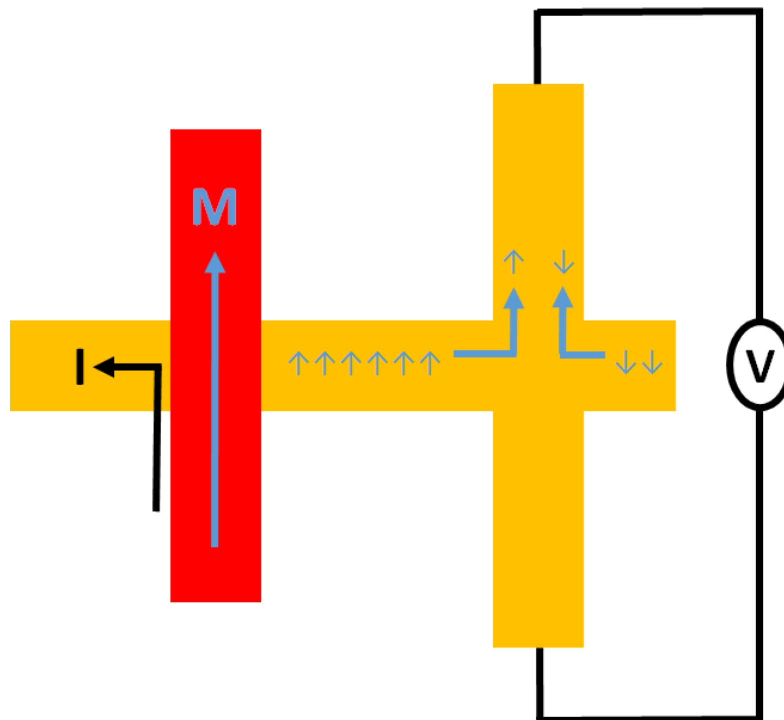

Figure 2- 14: Schematic showing the measurement configuration for the detection of non-equilibrium spins via the non-local inverse spin Hall Effect. In this case, the spin accumulation is injected into the non-magnetic system via a ferromagnetic metal with magnetization M.

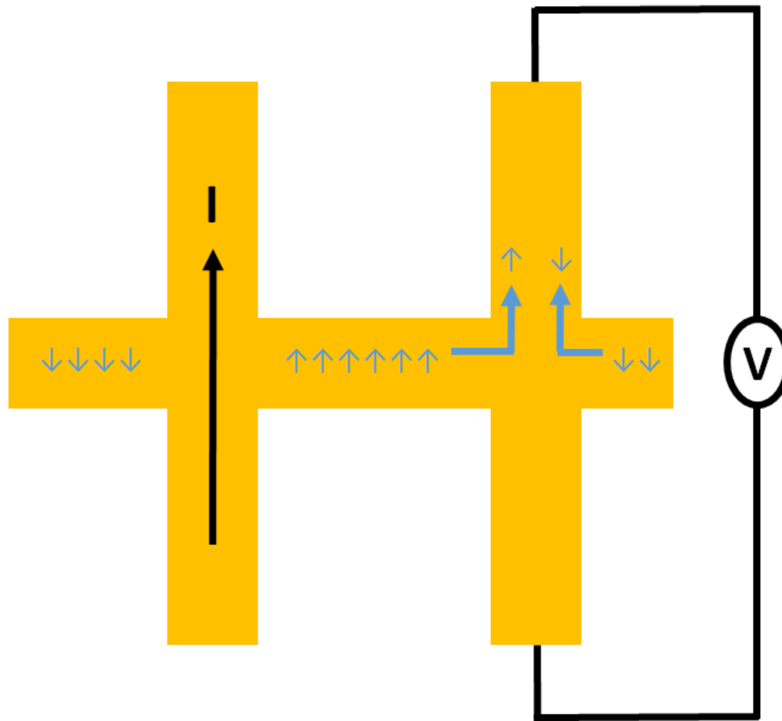

Figure 2- 15: Schematic showing the non-local H-bar measurement configuration for the detection of non-equilibrium spins via the inverse spin Hall Effect. In this case, the spin accumulation is injected into the non-magnetic system via the spin Hall Effect.

Non-local spin detection in the diffusive regime (H-bar configuration):

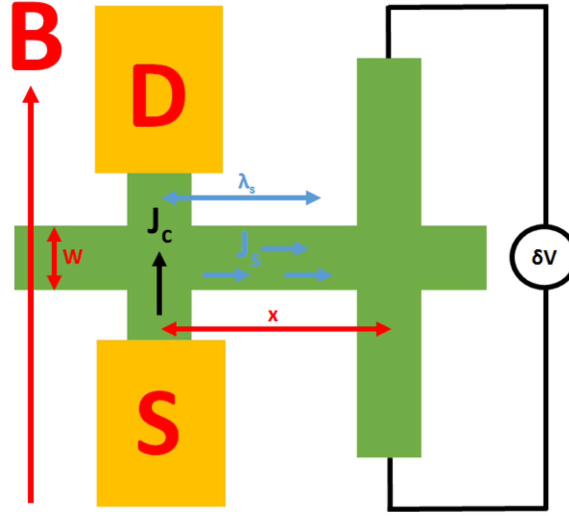

Figure 2- 16: Schematic showing non-local spin detection in the diffusive regime (H-bar configuration). Black arrow denotes the direction of charge current which is perpendicular to the spin current (blue arrow) and the corresponding system dimensions. In the case of precession measurement, the in plane magnetic field is applied in the direction as shown.

For simplicity, let us consider an infinitely narrow strip with width W such that $-\infty<x<+\infty$ and $-0.5W<y<0.5W$ (see Figure 2-16). Assuming $\lambda_s>>W$ and without loss of generality, the source and drain leads are narrow and placed at $(0,\pm 0.5W)$. In this system, the generated spins in-equilibrium are governed by the diffusive equation via the following relation[93]:

$$D_s\partial^2 s(x,y) - S_{SHE}(x,y) - \frac{1}{\tau_s}s(x,y) = 0\,. \tag{2.50}$$

Here S_{SHE} is the source term describing the spin current arising from SHE effect and s if the spin density in the z component. In the scenario of extrinsic SHE where the k-linear Dresselhaus and Rashba terms in the system are negligible, the source term can be expressed in terms of the spin hall conductivity σ_{SHE} as[93]:

$$S_{SHE}(x,y) = \sigma_{SHE}\delta(y-0.5W)E_{x,+}(x) - \sigma_{SHE}\delta(y+0.5W)E_{x,-}(x) \tag{2.51}$$

where $E_{x,\pm}(x)$ is the electric field at the boundaries of the system. These equations can be solved by using the inverse Fourier transform technique and noting that the source term is an odd function of x to obtain the total spin current in the system:

$$J_S(x) = \frac{IW\sigma_{SHE}}{2\sigma\lambda_s} e^{-|x|/\lambda_s} \,. \tag{2.52}$$

This spin current $J_S(x)$ in turn creates a non-local voltage across an adjacent detector pairs via the inverse SHE and the non-local voltage can be given by:

$$\delta V(x) = \frac{\gamma J_S(x)}{\sigma} = \frac{IW\gamma\sigma_{SHE}}{2\sigma^2\lambda_s} e^{-|x|/\lambda_s} \tag{2.53}$$

where $\gamma=\sigma_{SHE}/\sigma$ is the spin Hall coefficient. Finally the non-local signal can be expressed as a transverse resistance by dividing the equation (2.53) with I:

$$R_{non-local} = \frac{\delta V(x)}{I} = \frac{\gamma^2 W}{2\sigma\lambda_s} e^{-|x|/\lambda_s} \,. \tag{2.54}$$

From the final expression of the non-local signal, it is evident that the by studying the dependence of this non-signal with respect to W and x, key spin parameters such as spin relaxation length λ_s and spin Hall coefficient γ can be estimated. Note, the non-local signal decays exponentially with length x for a fixed width W and varies linearly with width W for a fixed x.

Non-local signal under the influence of an external magnetic field:

If the system is subjected to an external in-plane magnetic field, the spin diffusion equation has an additional term that describes the spin precession around the magnetic field[93]:

$$D_s\partial^2 \boldsymbol{s} - \boldsymbol{S_{SHE}} - \frac{s}{\tau_s} + [\boldsymbol{\omega_B} \times \boldsymbol{s}] = 0 \tag{2.55}$$

where $\boldsymbol{\omega_B}=g\mu_B\boldsymbol{B}$ is the Larmor precession frequency. This magnetic field dependence diffusion equation can be solved to obtain the total spin current in the channel:

$$J_S(x) = \frac{IW\sigma_{SHE}}{2\sigma} Re\left[\left(\frac{\sqrt{1+i\omega_B\tau_S}}{\lambda_S}\right) e^{-\left(\frac{\sqrt{1+i\omega_B\tau_S}}{\lambda_S}\right)|x|}\right] . \tag{2.56}$$

and subsequently the transverse resistance:

$$R_{non-local} = \frac{\delta V(x)}{I} = \frac{\gamma^2 W}{2\sigma} Re\left[\left(\frac{\sqrt{1+i\omega_B\tau_s}}{\lambda_s}\right) e^{-\left(\frac{\sqrt{1+i\omega_B\tau_s}}{\lambda_s}\right)|x|}\right]. \quad (2.57)$$

At the first glance on this equation, it certainly does not inform us on how the non-local resistance changes under the influence of an external in-plane magnetic field. However at higher magnetic fields, the equation (2.57) can be simplified to:

$$R_{non-local} = \frac{\gamma^2 W}{2\sigma}\sqrt{\omega_B\tau_s}\,\sin\left(\frac{\sqrt{\omega_B\tau_s}|x|}{\sqrt{2}\lambda_s} + \frac{\pi}{4}\right) e^{-\left(\frac{\sqrt{\omega_B\tau_s/2}}{\lambda_s}\right)|x|}. \quad (2.58)$$

With this simplified equation, it is clear that the application of this external in-plane field varies the non-local resistance with multiple sign changes in addition to the damping effect. Therefore, the oscillatory behavior of this non-local SHE resistance is a direct evidence that this effect is indeed originated from spins.

2.3.5 GRAPHENE SPINTRONICS

Here in this sub-chapter, we will briefly discuss on spintronics in graphene. Graphene as we know comprises of carbon atoms with an atomic number of 6. With this low atomic number, the intrinsic spin-orbit interaction which is proportional to Z^4, is very weak (see sub-chapter on spin-orbit coupling). This results in a very weak spin dependent scattering due to the intrinsic spin-orbit interaction. Therefore, the accumulated spins in such system should persist for very long distance and the spin relaxation length λ_s should be comparatively large[97–99]. In addition, graphene has very weak or negligible hyperfine interactions due to a miniscule amount of C13 isotope (which possesses the nuclear spin) among the carbon atoms ~1 %. The effect of nuclear spins on graphene spin transport is thus negligible. Based on theoretical calculations, spin relaxation length λ_s in graphene is estimated to be in the order of 100 μm[98]. However, there is a huge discrepancy between the theoretical prediction and experimental findings. Initial measurements in graphene spin transport result in spin relaxation length λ_s in

the order of ~1 μm. Efforts have been devoted to understand this anomaly and this difference can be attributed to additional spin dephasing mechanism due to factors such as 1) the presence of impurities like hydrogen atoms and 2) contributions from the surface optical phonons from the underlying substrate[59,98,100,101]. Recently there have been results demonstrating a spin relaxation length λ_s in the order of ~10 μm by employing substrate engineering (boron nitride)[102,103]. Notably, Fert's group has demonstrated that the predicted theoretical predicted spin relaxation length λ_s of 100 μm could be achieved in an ultra-clean high mobility epitaxial graphene device[34]. Before we dwell into the spin relaxation mechanisms in graphene, let us first look at the two important spin scattering mechanisms that have been repeatedly discussed in graphene.

Spin relaxation mechanism (Elliot-Yafet):

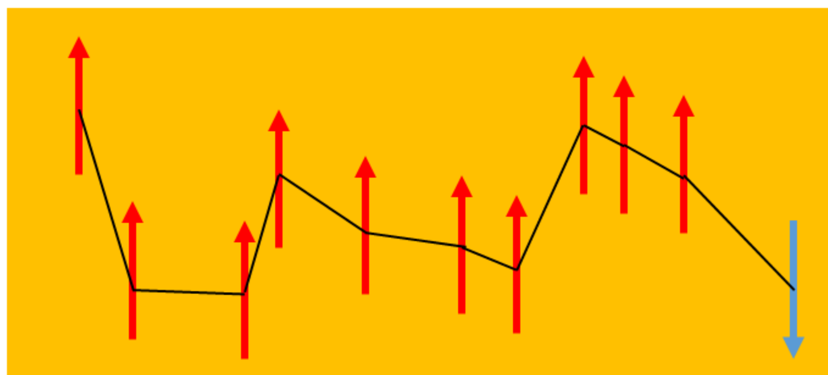

Figure 2- 17: Schematics for Elliot-Yafet spin relaxation mechanism. The momentum scattering by impurities or phonons has a finite probability to flip the electron spin.

Within the theory of Elliott-Yafet (EY)[104,105], the spin scattering arises due to the momentum scattering of the conduction electrons with phonons or impurities. Owing to the spin-orbit interactions, the eigenstates of the electron wave-functions are a combination of both spin-up and spin-down states. The probability of electron's spin flipping increases with each momentum scattering, hence the faster the rate of momentum scattering the faster the rate of

relaxation of spins. That is for EY mechanism, the spin relaxation rate is proportional to the momentum relaxation rate:

$$\tau_s \propto \tau_p \,. \qquad (2.59)$$

Spin relaxation mechanism (D'yakonov-Perel):

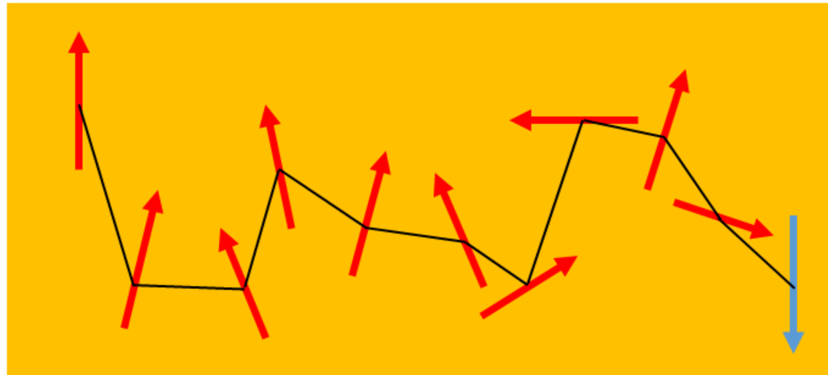

Figure 2- 18: Schematic for D'yakonov-Perel spin relaxation mechanism. Electron spin flip occurs via electron spin precession about the momentum dependent magnetic field.

The D'yakonov-Perel[106] is the dominant scattering mechanism in semiconductor systems without a centre of symmetry such as GaAs which has a zinc blende type crystal structure. In this system, the inversion symmetry is broken due to the occupation of two different atoms in the Bravais lattice. The absence of inversion symmetry results in the momentum states for both spin-up and spin-down electrons to be non-degenerate. This spin splitting created by the inversion asymmetry causes a momentum dependent magnetic field $B(k)$. The precession of electron's spin about this induced magnetic field proceeds with a Larmor frequency given by $\Omega(k)=(e/m)B(k)$. This intrinsic magnetic field arises from the spin-orbit interaction in the system. This momentum dependent magnetic field changes both in direction and magnitude as the electron gets scattered by impurities or phonons. In other words, the electron spins precession axis and direction varies and the spin relaxation occurs in between the momentum scattering events. Therefore, the higher the momentum scattering rate, the less the spin relaxation rate:

$$\tau_s \propto \frac{1}{\tau_p} \,. \tag{2.60}$$

Now we are in a better position to discuss on spin relaxation mechanisms in graphene. However, the task of identifying the spin scattering mechanism in graphene has proven to be extremely challenging. Initial spin transport experiments in graphene have pointed out the significance of EY spin scattering mechanism in both single layer graphene and multilayer graphene[31,59,107,108]. Soon after, experiments on bilayer graphene concluded an absolutely different result; the dominant scattering mechanism is DP[75,108]. Due to the different experimental outcomes, theoretical models have been developed and they suggest that indeed the DP mechanism could be the main factor along with the influences of EY and also spin-orbit interactions from random Rashba fields. An absolute and[98,109] detailed understanding of the dominant spin scattering mechanism in graphene is still absence as of today. In general for discussion purpose, the spin scattering rate can be modelled and written as a summation of both EY and DP mechanisms as follows:

$$\frac{1}{\tau_s} = \frac{1}{\tau_s^{EY}} + \frac{1}{\tau_s^{DP}} \,. \tag{2.61}$$

Here, the spin relaxation rate for EY and DP can be expressed in terms of spin-orbit coupling strength as:

$$\frac{1}{\tau_s^{EY}} = \frac{\Delta_{EY}^2}{\varepsilon_F^2}\frac{1}{\tau_p} \tag{2.62}$$

and

$$\frac{1}{\tau_s^{DP}} = \frac{4\Delta_{DP}^2}{\hbar^2}\tau_p \,. \tag{2.63}$$

In these equations, $\frac{1}{\tau_s^{EY}}$ and $\frac{1}{\tau_s^{DP}}$ are the spin scattering rate for EY and DP mechanism respectively and Δ_{EY} and Δ_{DP} are the corresponding spin-orbit coupling strengths. By substituting these two equations into equation (2.61), we obtain:

$$\frac{\varepsilon_F^2 \tau_p}{\tau_s} = \Delta_{EY}^2 + \frac{4\Delta_{DP}^2}{\hbar^2} \varepsilon_F^2 \tau_p^2 \, . \tag{2.64}$$

The above equation which includes both spin scattering mechanisms can be used to model experimental results on spin transport in graphene based devices to determine the dominant spin scattering mechanism[102]. In this thesis, we will focus our effort in understanding the spin transport studies in graphene by enhancing its otherwise weak spin-orbit interaction by chemical functionalization and also by adatom induced spin-orbit coupling.

2.4 THERMOELECTRIC

2.4.1 SEEBECK-PELTIER-THOMSON EFFECT

Thomas Johann Seebeck was the first person who studied the relation between heat gradient on dissimilar metals and induced electrical voltage[37]. In 1821, he discovered that a temperature difference created on two distinct materials will induce an electrical voltage or vice versa. At the atomic scale, the created temperature bias diffuses the carriers in the system from the hotter end to the colder end. As a result, the chemical potential of the charge carriers will be modified changing the concentration of carriers along the system and thus inducing an electrical voltage. The study of thermoelectric includes three independently discovered effects: 1) Seebeck effect[37], 2) Peltier effect and 3) Thomson effect[38].

Seebeck effect:

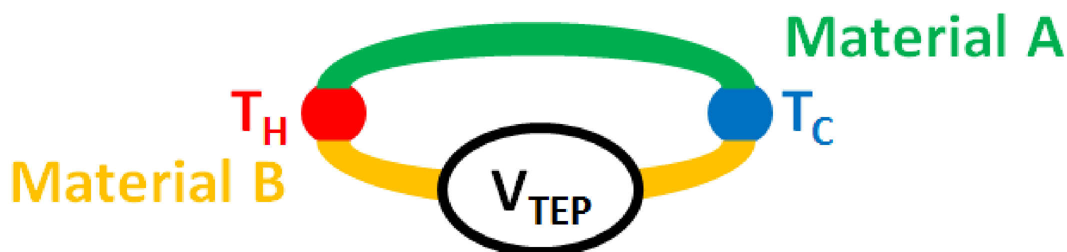

Figure 2- 19: Schematics illustrating Seebeck effect with two junctions formed by two dissimilar materials subjected to a temperature gradient.

Figure 2-19 shows the schematics illustrating Seebeck effect. A temperature gradient between the junctions formed by two dissimilar materials will induce an electrical voltage between the junctions. The Seebeck effect can be described as the following equation:

$$S = -\frac{V_{TEP}}{\Delta T}, \tag{2.65}$$

where S is known as the Seebeck coefficient, V_{TEP} is the thermoelectric voltage and ΔT is the temperature bias.

Peltier effect:

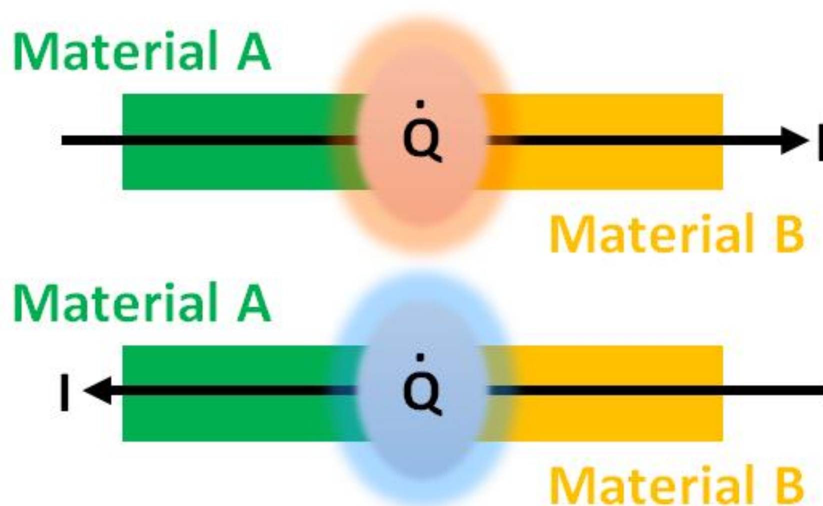

Figure 2- 20: Schematics showing Peltier effect whereby heat can be generated or removed in a junction between two distinct materials depending on the direction of the applied electrical current.

Peltier effect describes the phenomenon whereby when an electrical current is driven through a junction formed by two distinct materials, heat maybe generated or removed from the junction (see Figure 2-20). The heat is generated (to warm) or removed (to cool) depending on the intrinsic properties of the materials forming the junction. In the case of Peltier effect, the heat energy is proportional to the driven electrical current and thus it is fundamentally different from Joule heating. The Peltier effect can be described with the following equation:

$$\dot{Q} = (\Pi_A - \Pi_B)I\ , \qquad (2.66)$$

where $\dot{Q}$ is the rate of heat energy generated, Π_A and Π_B are the Peltier coefficients for the materials used.

Thomson effect:

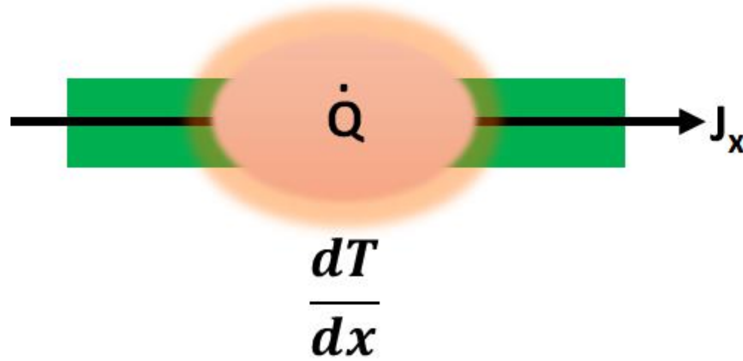

Figure 2- 21: Schematics showing Thomson effect; combination of Seebeck and Peltier effects in a single material whereby a temperature gradient creates a variation of Seebeck coefficient and in turn causes a continuous Peltier effect.

In 1851, William Thomson combined both Seebeck and Peltier effects to become Thomson effect and later on became the governing equation for thermoelectric. For many materials, Seebeck coefficient depends on the temperature; thus a spatial variation of temperature bias can result in a spatial variation of Seebeck coefficient. This variation of Seebeck coefficient in turn creates a continuous Peltier effect in the same material. The Thomson effect can be described as:

$$\dot{Q} = -\beta \boldsymbol{J}.\boldsymbol{\nabla T}\ , \qquad (2.67)$$

where $\beta = T(dS/dT)$ is the Thomson coefficient and $\Pi = TS$; showing the close relation between these effects.

2.4.2 THERMOELECTRIC TRANSPORT IN SOLIDS

Heat capacity of free electron gas:

One of the main difficulties in the early stage of developing the electron theory is the modelling of heat capacity of conduction electrons. Based on classical statistical mechanics, a free particle has a heat capacity of $3k_B/2$, where k_B is the Boltzmann constant. If a system contains N atoms whereby each atom contributes one valence electron to conduction, then the heat capacity of the system is simply $3k_BN/2$. However there is a huge discrepancy between this simplified classical theory with experimental value at room temperature; the latter being usually ~<0.01 of $3k_BN/2$. The inconsistency lies in the following argument; when the system is heated from absolute zero, not every electron gains an equal energy of $\sim k_BT$ as predicted classically, but only the electrons within an energy of $\sim k_BT$ of Fermi level are excited thermally. Therefore only a fraction of electrons T/T_F can be thermally excited at temperature T since only these electrons lie within an energy range of the order of k_BT of the energy distribution. Each of these electrons (NT/T_F) has a thermal energy of k_BT and thus the total electronic thermal kinetic energy is given by:

$$U_{electron} = \frac{NT}{T_F} \times k_BT \; . \qquad (2.68)$$

From equation (2.68), we can then obtain the electronic heat capacity via:

$$C_{electron} = \frac{\partial U}{\partial T} \approx Nk_B \frac{T}{T_F} \; . \qquad (2.69)$$

At room temperature, the electronic heat capacity given by equation (2.69) can be a fraction of 0.01 or less than the classical value of $3k_BN/2$ for T_F is the Fermi temperature$\sim 5\times10^4$ K.

Heat transport in metal:

In a metallic system, if we again assume that each atom contributes one free electron for conduction, we can obtain the Thomson coefficient (see sub-chapter on Thomson effect) from the combination of classical thermodynamics and Maxwellian distribution as:

$$\beta \approx \frac{C_{electron}}{Ne} = \frac{3}{2}\frac{k_B}{e} \,. \tag{2.70}$$

A quick glance at equation (2.70), it shows that the Thomson coefficient given by the equation is a constant. This means that different metallic systems should have the same Thomson coefficient; however this contradicts the experimental observations. If we now introduce the argument presented in the previous section; for quantum theory, only a fraction of total electrons can contribute to the heat conduction, the electronic heat capacity can be shown to be[110]:

$$C_{electron} = \frac{1}{2}\pi^2 \frac{Nk_BT}{T_F} \,. \tag{2.71}$$

The improved equation shows a linear proportionality between the electronic heat capacity and temperature, however still it does not describe accurately the experimental results because in this ideal model, the electrons in the metallic system are treated as rigid particles and thus all scatterings involved are assumed to of elastic in nature. For real systems, where scattering processes include inelastic scattering and scattering by phonons, additional concerns and parameters need to be included to give a more accurate representation of electronic heat capacity. Phonons can be generated in the system if there exists a temperature gradient and the phonon-electron interactions are often termed as phonon-drag effect. The contribution to Seebeck effect from phonons can be expressed as[111]:

$$S_v \approx \frac{1}{3}\frac{C_v}{N_v e}\alpha \,. \tag{2.72}$$

Here C_v is the electronic heat capacity per unit volume, N_v is density of the electrons and α is a parameter that describes the phonon-electron scattering ($0<\alpha<1$). By including all contributions from different scattering mechanisms and assuming a Fermi-Dirac distribution for the electrons in the metallic system, the Seebeck coefficient can be expressed as[111]:

$$S = \frac{\pi^2 {k_B}^2 T}{3e\varepsilon_0}\left(\frac{\mathrm{dln}n(E)}{dE} + \frac{\mathrm{dln}v^2(E)}{dE} + \frac{\mathrm{dln}\tau(E)}{dE}\right)\Big|_{E=\varepsilon_0} \tag{2.73}$$

In equation (2.73), $\varepsilon_0 = \frac{h^2}{8m}(\frac{3n_0}{\pi})^{\frac{2}{3}}$ is the Fermi energy at 0 K, $n(E)$ is the density of states, v^2 is the mean square velocity and τ is the relaxation time. From this equation we can obtain the famous Mott formula[111]:

$$S = \frac{\pi^2 {k_B}^2 T}{3e\varepsilon_0}\left(\frac{d\ln\sigma(E)}{dE}\right)|_{E=\varepsilon_0}\,, \tag{2.74}$$

by noting that $\sigma(E) = An(E)v^2\tau$ is scattering cross section. It is worthy to note that, for metallic system at room temperature, the phonon-electron scattering is very weak. Phonon-phonon scattering will dominate because phonon contributions will increase as we increase the temperature. For most metallic systems, phonon-drag effect can only be seen at lower temperatures. From equation (2.74), we can see that the Seebeck coefficient (thermopower) depends not only on the charge carriers but also on the Fermi surface and band structure of metals ($ln\sigma(E)$).

Heat transport in semiconductor:

For a semiconducting system, the carrier density is much smaller as compared to a metallic system. The carrier density in a semiconductor system has an Arrhenius type temperature dependence, $N \propto e^{-\frac{E_g}{k_B T}}$ where E_g is energy band gap. The Thomson coefficient can be shown for a semiconducting system as[111]:

$$\beta = \frac{k_B}{e}\left(\frac{3}{2} - \frac{TdN}{NdT}\right) = \frac{k_B}{e}\left(\frac{3}{2} - \frac{U}{k_B T}\right). \tag{2.75}$$

The contribution from phonon-drag is much stronger in a semiconductor system due to the lower carrier density, equation (2.72). For semiconductors, this effect could give Seebeck coefficient in the orders of tenths of mVK^{-1} approximately three orders of magnitude higher than in metals; as we shall see later in chapter 6. By substituting Maxwell distribution in place of Fermi-Dirac, the Seebeck equation can be modified to be[111]:

$$S = \frac{k_B}{e}\left(\frac{5}{2} + \frac{d\ln\tau(E)}{d\ln E} - \frac{\varepsilon}{k_B T}\right). \tag{2.76}$$

Here $\frac{\varepsilon}{k_B T} = \ln\left(\frac{1}{2} N_V h^3 (2\pi m k_B T)^{\frac{-3}{2}}\right)$ and N_v is the carrier density; this equation gives Seebeck coefficient in the order of few ~k_B/e.

Umklapp scattering process:

The phonon-electron scattering proceeds with two different scattering interactions: 1) normal scattering and 2) Umklapp scattering. If an electron starts from an initial state $\boldsymbol{k}$ and scatters to an end state $\boldsymbol{k'}$ while emitting a phonon with energy $\hbar$v with lattice wave vector $\boldsymbol{q}$, we can obtain the following equation based on momentum conversation and boundary condition:

$$\boldsymbol{k} - \boldsymbol{k}' = \boldsymbol{q} + \boldsymbol{g}\,. \tag{2.77}$$

Here $\boldsymbol{g}$ is the reciprocal lattice vector. We characterize this scattering as normal if $\boldsymbol{g}$=0. This scattering process can be depicted as shown in Figure 2-22; the scattering occurs in a single Brillouin zone. In this normal scattering, $\boldsymbol{q}$ is parallel with $\Delta\boldsymbol{k} = \boldsymbol{k} - \boldsymbol{k}'$ which means that both phonon and electron are travelling in the same direction. This normal scattering mechanism of phonon-drag results in a negative contribution to Seebeck coefficient.

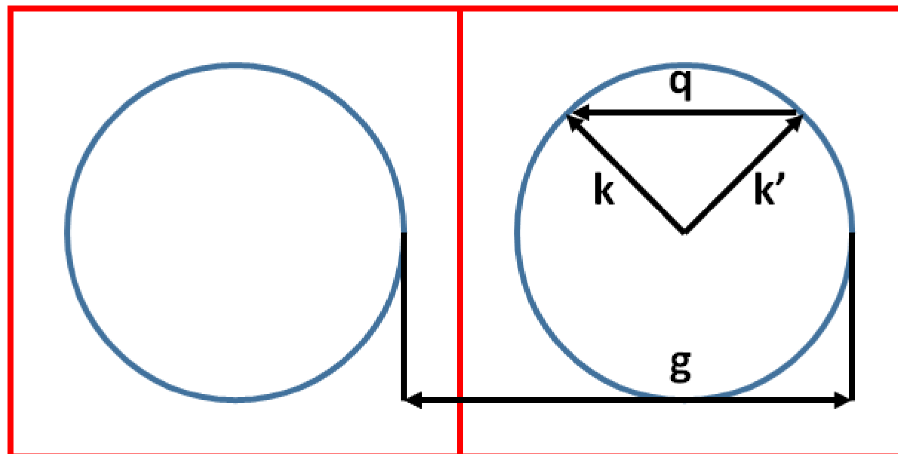

Figure 2- 22: Schematics showing normal scattering with **q** being parallel to **Δk**.

We characterize this scattering as an Umklapp process when $\boldsymbol{g} \neq 0$; scattering proceeds in different Brillouin zones (see Figure 2-23). Umklapp scattering is not limited to phonon-drag effect but also occurs in phonon-phonon scattering. The reciprocal lattice vector $\boldsymbol{g}$ is usually a

very large vector, hence $\boldsymbol{q}$ would be antiparallel with $\Delta\boldsymbol{k} = \boldsymbol{k} - \boldsymbol{k}'$, which means that in this case phonon and electron travel in the opposite direction. This process turns out to be of significant importance because Umklapp scattering results in positive contribution to the Seebeck coefficient.

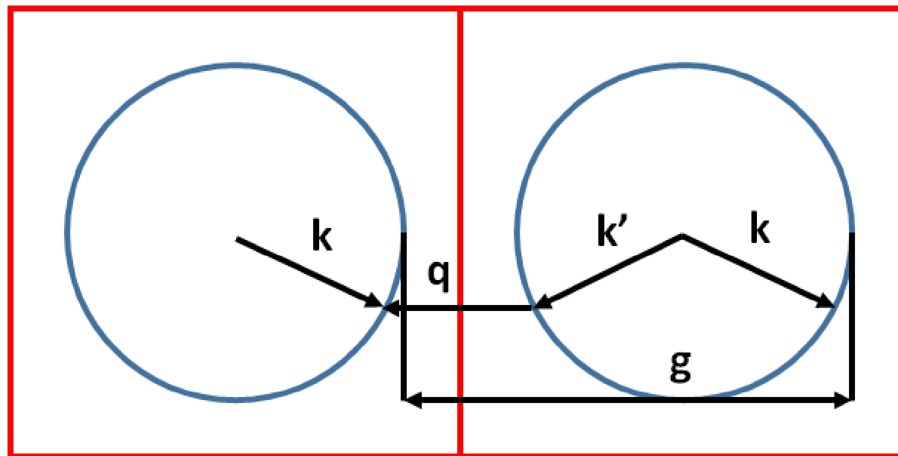

Figure 2- 23: Schematics showing Umklapp scattering process with **q** being antiparallel to **Δk**.

The contribution to Seebeck coefficient from phonon-drag effect is the summation of these two mechanisms. From equation (2.77) we see that the Umklapp scattering is related closely to the reciprocal lattice vector $\boldsymbol{g}$. Therefore this scattering is very sensitive to lattice structure and also on the Fermi surface.

Thermoelectric devices/materials and efficiency:

Thermoelectric devices can be seen as solid-state energy converters which rely on its thermal, electrical, and semiconducting properties to recycle waste heat into useful electricity or vice versa. Recently the increasing importance of the thermal properties of materials is demonstrated both in practical application needs and fundamental science understandings[112]. Waste heat removal has become an unavoidable problem for continuous progress in the electronic industry due to increased levels of power dissipations. Continuous search for perfect thermoelectric materials has become essential; to incorporate to next generation of integrated electronic circuits. Thermoelectric energy conversion necessitates materials that have a highly

suppressed thermal conductivity[42]. Thermal conductivity of a material depends strongly on its atomic structure and thus by studying the thermal properties we can better understand the characteristics of the material.

The universal figure of merit that governs the performance of a thermoelectric material is given by:

$$ZT = \frac{\sigma S^2 T}{\kappa}\,. \tag{2.78}$$

Here σ and κ are the electrical and thermal conductivities respectively. However in an actual thermoelectric device for application whereby two distinct materials are used, the maximum efficiency of the device is given by[113]:

$$\eta = \frac{\Delta T}{T_H}\frac{\sqrt{1+Z\bar{T}}-1}{\sqrt{1+Z\bar{T}}+T_C/T_H}\,. \tag{2.79}$$

Here $Z\bar{T} = \frac{\left(S_p - S_n\right)^2}{\left[(\rho_n\kappa_n)^{\frac{1}{2}}+(\rho_p\kappa_p)^{\frac{1}{2}}\right]^2}\left(\frac{T_H+T_C}{2}\right)$. Figure 2-24 shows the schematics for single thermoelectric couple based on black phosphorus and subsequent integration into a thermoelectric module in an energy harvesting system.

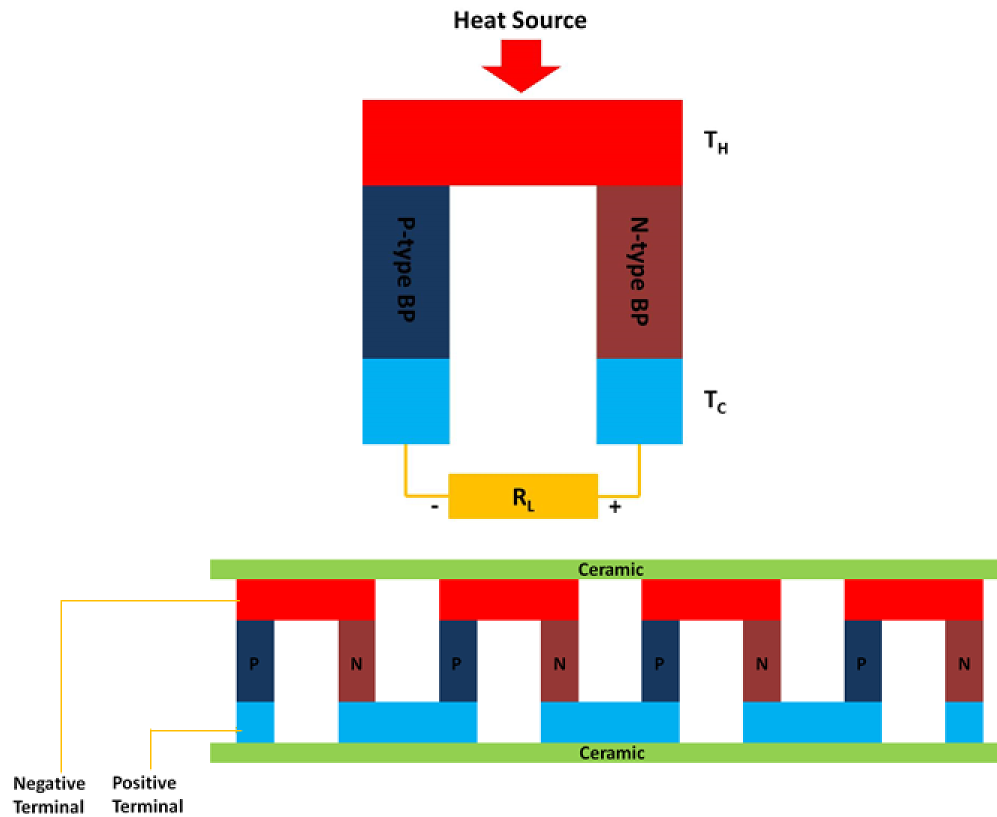

Figure 2- 24: Schematics showing a single thermoelectric couple for thermoelectric power generation. In this case black phosphorus can be doped to p-type and n-type to be incorporated into a single thermoelectric couple device. Multiple of these thermoelectric couples can then be connected electrically in series and thermally in parallel to create a thermoelectric module for energy harvesting system.

CHAPTER 3 EXPERIMENTAL TECHNIQUES

In this chapter, the detailed fabrication processes of graphene and black phosphorus based devices are described. For graphene, both mechanically exfoliated and chemically grown crystals were used; whereas for black phosphorus, only mechanically exfoliated crystals were used. Prior to further fabrication processes, standard characterization methods such as Optical Microscopy, Atomic Force Microscopy (AFM) and Raman Spectroscopy were employed to opt for the most ideal crystals for the given experiment. Next, measurement contacts were made by conventional electron beam lithography, employing poly(methyl methacrylate) (PMMA) as the electron beam resist and metal deposition using both electron beam evaporation and thermal evaporation. All final devices were electrically characterized with different measurement configurations with or without magnetic field depending on the type of experiment in a vacuum cryostat chamber.

3.1 FROM BULK TO 2D

3.1.1 GRAPHENE

Fabrication processes starts with cleaning of Si/SiO_2 substrates; as purchased Si/SiO_2 6-inch Nova Wafers with a resistivity of ~0.01 Ωcm and a dry chlorinated thermal oxide thickness of 300 nm were cubed into size of 1 cm by 1 cm before the standard cleaning procedures. The diced wafers were ultra-sonicated in an acetone bath for approximately ~15 minutes followed by IPA bath for another ~15 minutes to remove unwanted particles. Then, the wafers were blown dry by nitrogen N_2 gas.

Graphene crystals were acquired by the following simple steps, first discovered by the group in Manchester back in 2004[50]:

1. Uniformly thick pieces of highly oriented pyrolytic graphite (HOPG) were carefully placed onto an adhesive tape (Nitto-BT-150E-KL).
2. Graphite flakes were slowly thinned down (almost transparent) by repeated peelings of the adhesive tape.
3. The adhesive tape with almost transparent graphite flakes was pressed onto the cleaned Si/SiO_2 substrates.
4. Upon removing the tape, graphite crystals with varying thicknesses and sizes (average ~1500-2500 μm^2) were left on the substrates.
5. Finally, Optical Microscopy, Atomic Force Microscopy and Raman Spectroscopy were used to select the best crystals for the desired experiment.

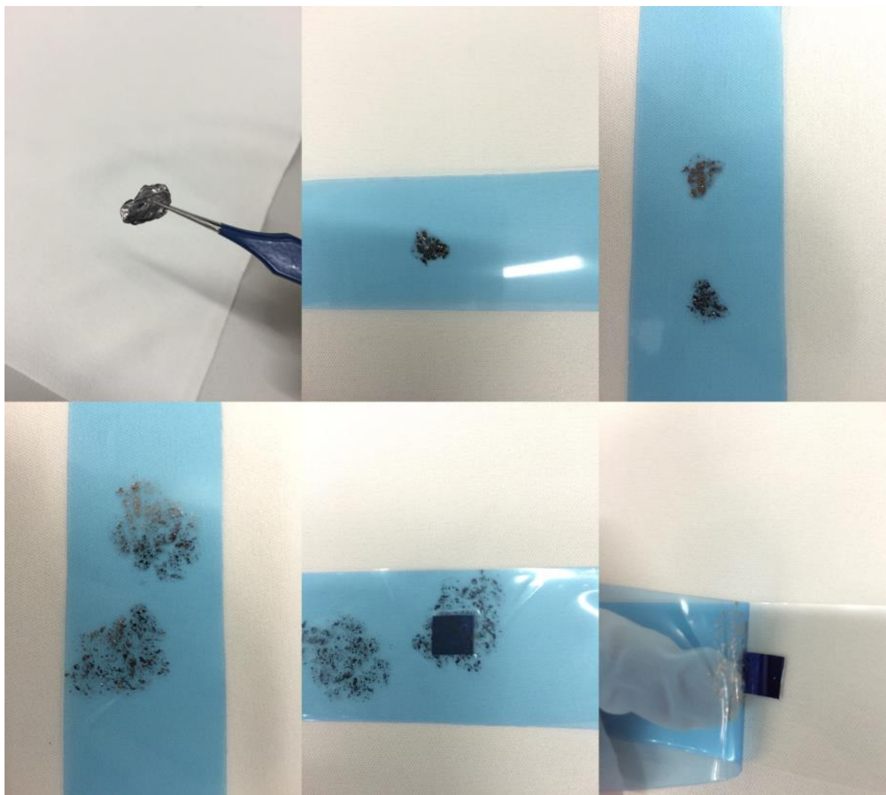

Figure 3- 1: Optical images showing the different steps in obtaining exfoliated graphene via micro-mechanical exfoliation method with scotch tape.

It is surprising, graphene being the thinnest material in the world can be identified under the optical microscope. This is in fact due to the combination of its optical transparency of ~98

%[114] and the specific oxide thickness (SiO_2) of 300 nm which results in a contrast, visible enough to be seen under the optical microscope[115]. For a more precise characterization, AFM can be used to determine exactly the number of graphene layers and in addition its surface morphology[116]. Another powerful tool commonly used to characterize graphene is Raman Spectroscopy. Raman characterization is a non-destructive method which can provide us additional details about the graphene crystals such as percentage of strain, concentration of defects and doping level[117]. For graphene crystals (single, bi or multilayers), the two major Raman peaks occur at ~1580 cm^{-1} (G band) and ~2690 cm^{-1} (2D band); careful studies of the intensity ratio between these peaks, full width half maxima of these peaks and position of the 2D band give information on the number of layers of the crystals. Meanwhile the relative shift in position of these peaks is a sign of doping and strain in graphene. There is an additional D band which occurs at ~1370 cm^{-1} for graphene with defects but absent in high quality graphene crystals.

3.1.2 BLACK PHOSPHORUS

Black phosphorus crystals were obtained similarly like graphene with the exception that these crystals are highly sensitive to ambient environment[118], thus extra care needs to be carried out while doing the mechanical exfoliation. The black phosphorus crystals were cleaved in an inert environment in a glove box (Argon atmosphere) to prevent degradation of these crystals. As cleaved black phosphorus reacts when exposed to ambient air and forms a layer of oxide on the top surface. To protect the crystals, electron beam resist PMMA can be spin-coated soon after locating the desired crystals in a glove box.

3.2 CHEMICAL VAPOUR DEPOSITION GRAPHENE

3.2.1 PREPARATION

In the previous sub-chapter, mechanical exfoliation of bulk graphite and black phosphorus to produce ultrathin 2D crystals have been discussed. Even though the method of mechanical exfoliation has been known to produce high quality crystals, the main limitation of this approach is the dimensions of the crystals obtained. With this method, the maximum size of the crystals is limited to ~80-100 µm and the yield varies from substrate to substrate. In order to integrate graphene into future industrial applications, the size of these crystals has to be considerably scaled up with a much higher production yield[119]. One of the most promising methods to grow high quality large area graphene with high coverage is by chemical vapor deposition (CVD)[119,120].

In this method, large area graphene films are grown on a metal catalyst such as Copper (Cu) and Nickel (Ni). During the growth, the metal is first heated to high temperature ~1000 °C in the chamber followed by an introduction of gas precursors in the form of methane CH_4 and hydrogen H_2 for approximately half an hour. After the growth process, the substrate is cooled down to room temperature under a hydrogen filled environment.

First of all, to take advantage of the large area CVD grown graphene, the graphene film has to be first transferred onto Si/SiO2 substrate by employing the methods listed below (CVD graphene grown on Copper film):

1. Electron beam resist PMMA is spin coated on the good surface of copper film to protect the graphene film while the graphene on the back side is etched away with Reactive Ion Etching (RIE) O_2 plasma treatment under vacuum ~10^{-3} mbar (Power: 50 W, Duration: 5 minutes, Flow: 50 sccm). Note: Graphene film grows on both sides of metal substrates.

2. After removing one side of graphene film, the resulting stacked structure of PMMA/Graphene/Copper is placed in an ammonium persulfate (APS) solution with a concentration of ~2 % (20 g of ammonium persulfate powder diluted in 1000 ml of DI water). Keeping the PMMA surface facing upward, the layers are placed in the solution for ~12 hours (overnight) until the copper film has been completely etched away.
3. After etching of the copper film, the resulting stacked structure of PMMA/Graphene is transferred into a clean DI water bath with the aid of a glass slide. The layers are kept in the DI water bath for ~2 hours to remove any unwanted APS residues and this procedure is repeated once more with a new DI water bath.
4. Finally, the stacked structure of PMMA/Graphene is transferred onto clean Si/SiO2 substrate and dried slowly on a hot plate set at ~80 °C for ~10 minutes. To remove the PMMA protective layer, few drops of anisole is placed onto the dried substrate to re-dissolute the cured PMMA. This step is crucial as it will enhance the adhesion of CVD graphene onto the substrate and reduce the amount of cracks on the graphene film. The sample is then left in acetone solution for ~30-60 minutes followed by IPA bath for ~15 minutes before finally dried with nitrogen N_2 gas.

3.3 GRAPHENE SPIN HALL EFFECT DEVICES

Chapter 4 and 5 in this thesis are dedicated to published work performed on graphene based spin Hall Effect devices and occupied large part of this thesis. Therefore, in the following sub-chapters, detailed fabrication processes of exfoliated graphene spin Hall Effect devices and CVD grown graphene spin Hall Effect devices are discussed.

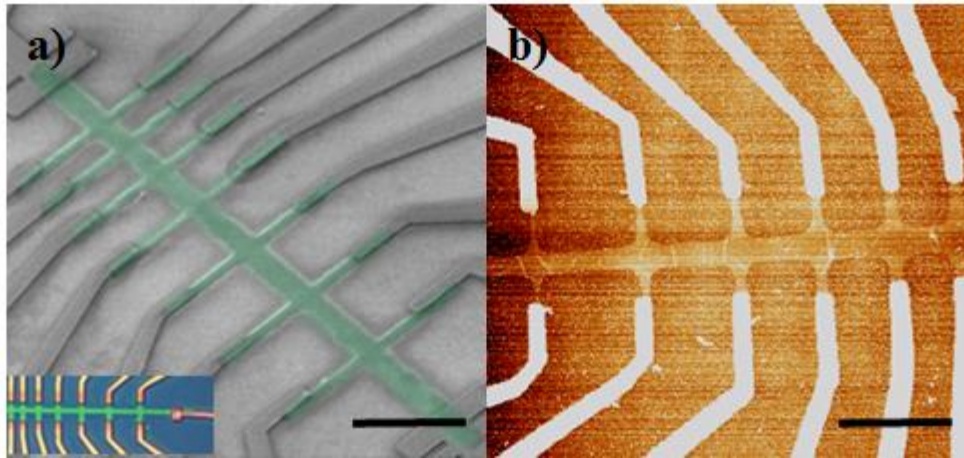

Figure 3- 2: a) Scanning electron microscope (SEM) image with false color of a hydrogenated exfoliated graphene hall bar device with varying junction lengths. Inset: Optical microscope image of the same device. b) Atomic force microscopy (AFM) image of a CVD grown graphene hall bar device with varying junction lengths. Scale bar is 2 μm.

3.3.1 EXFOLIATED GRAPHENE DEVICES

First of all, graphene crystals were obtained by mechanical exfoliation method as described above. Clean, isolated graphene crystals with the dimensions of at least 5 μm by 15 μm were selected for device fabrications. In this thesis, PMMA polymer is used as the electron beam lithography resist. The wafers are spin coated with dual PMMA layer for lithography patterning following the recipe below:

1. First layer of PMMA A3 (%3, 450 K) spun at 2000 rpm for 80 seconds (twice).
2. Hot plate baking at 170 °C for 10 minutes.
3. Second layer of PMMA A5 (%5, 950 K) spun at 4000 rpm for 80 seconds.
4. Hot plate baking at 180 °C for 2 minutes.

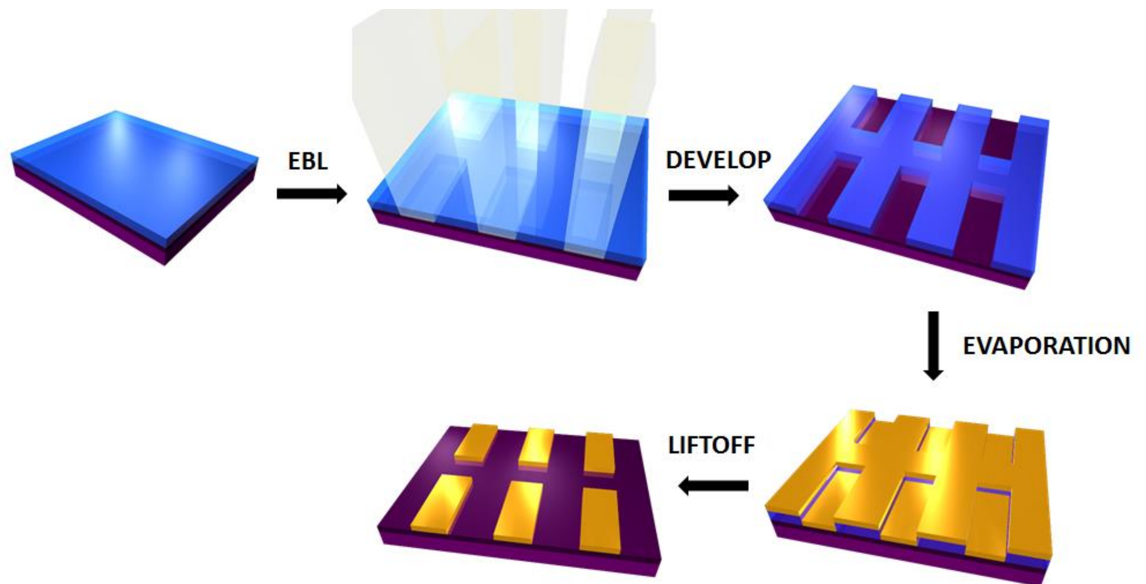

Figure 3- 3: Schematic diagrams showing the device fabrication steps involved by using positive electron beam resist such as PMMA.

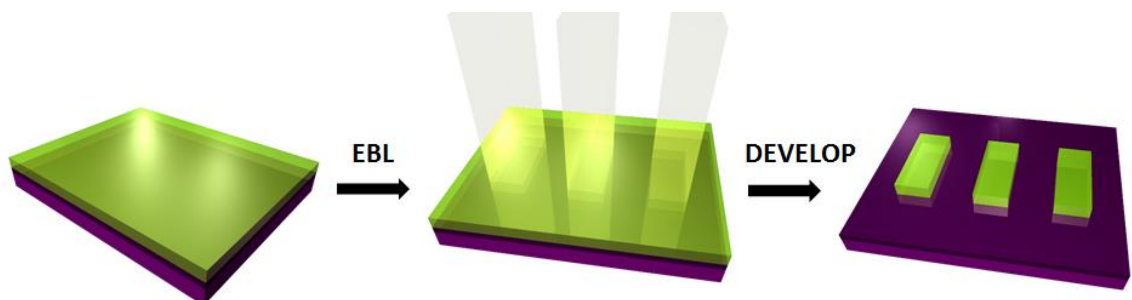

Figure 3- 4: Schematic diagrams showing the device fabrication steps involved (up to development) by using negative electron beam resist such as HSQ.

Following these steps, a total PMMA thickness of ~450 nm is obtained. With dual PMMA layer, the liftoff process time is reduced and results in a better yield as well. Electron beam (FEI Nano SEM 230 electron beam lithography) is used to define the desired patterns depending on the type of devices needed. The beam is accelerated with a voltage of 30 kV and an area dose of 450 μC/cm^2 is used for all patterning purposes. The mixture of Methyl isobutyl ketone (MIBK) and Isopropyl alcohol (IPA) in the ratio of 1:3 is used as developer for PMMA

resist and acetone is used for PMMA removal. Below are the steps involved in making a standard graphene hall bar device:

1. Spin coat sample with dual PMMA layer following the recipe listed above. Patterning of alignment markers with electron beam lithography. Development with the mixture of MIBK and IPA for 1 minute followed by IPA bath for another minute.
2. Designing graphene hall bar device with Design CAD which includes electrodes and etch mask for graphene with the aid of images obtained from optical microscopy.
3. Patterning of device electrodes together with additional alignment markers. Development with the mixture of MIBK and IPA for 1 minute followed by IPA bath for another minute.
4. Deposition of chromium (Cr)/gold (Au) metal under high vacuum ~10^{-7} Torr by using a thermal evaporator to form device electrodes. Both Cr and Au sources are out gassed before the actual deposition of the device. Approximately ~5 nm of Cr is evaporated at a deposition rate of 0.05 nm/s followed by ~80 nm of Au at a deposition rate of 0.1 nm/s. (Note: Cr is evaporated to create a better adhesion between Au contact and graphene).
5. Liftoff process in hot acetone bath ~65 °C for 1-2 hours followed by IPA bath for 1-2 minutes. Spin coat sample with dual PMMA layer again for second electron beam lithography step to define graphene etch mask.
6. Patterning of graphene etch mask to define the hall bar structure. Development with the mixture of MIBK and IPA for 1 minute followed by IPA bath for another minute. Unwanted graphene area is etched by using Reactive Ion Etching (RIE) O_2

plasma treatment under vacuum ~10^{-3} mbar (Power: 20 W, Duration: 20 seconds, Flow: 20 sccm).

7. Finally the removal of PMMA resist in acetone bath for 15 minutes followed by IPA bath for 1-2 minutes.

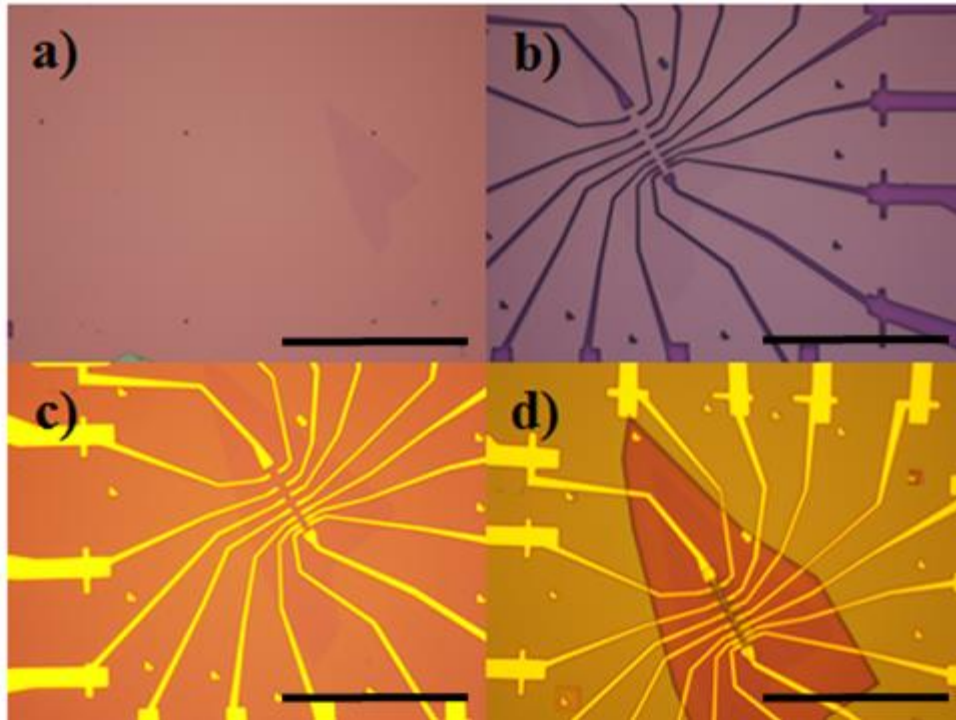

Figure 3- 5: Optical images of graphene taken after a) patterning of alignment markers (graphene is area with darker contrast), b) patterning of device electrodes with the aid of the patterned alignment markers, c) thermal evaporation of Cr/Au metals and liftoff process and d) patterning of etch mask to define the unwanted area of graphene to be etched away. Scale bar in a) is 100 µm and in b), c), and d) is 50 µm.

3.3.2 CVD GRAPHENE DEVICES

The fabrication of CVD graphene devices starts with the preparation of CVD graphene as discussed above. After CVD graphene has been transferred onto Si/SiO2 substrate, clean and crack free areas are selected for further fabrication processes. Next, the device fabrication

steps are similar to exfoliated graphene device with the exception of etch mask patterning. For CVD graphene devices, the fabrication processes start with patterning of alignment markers and subsequent deposition of chromium (Cr)/gold (Au) metal by using thermal evaporation to create permanent alignment markers. These metal alignment markers are crucial because it enable us to select clean and crack free area for further fabrication processes. In this case, these permanent markers can be used for both etch mask patterning and device electrodes patterning subsequently.

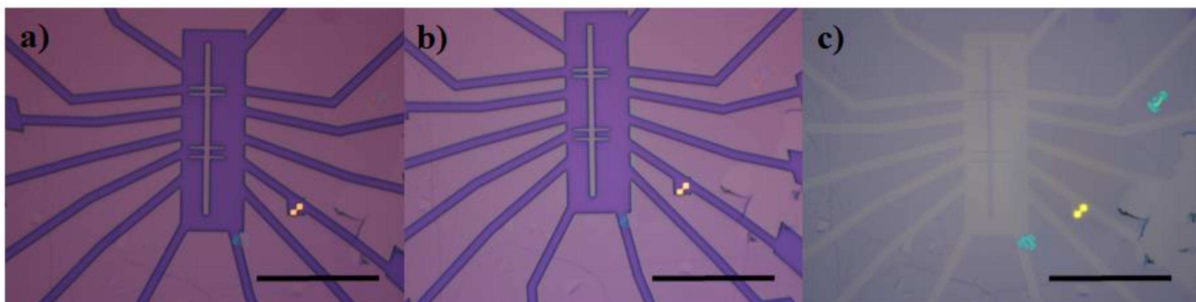

Figure 3- 6: Optical images of CVD graphene taken after a) patterning of etch mask with metal alignment markers, b) RIE O2 plasma of unwanted areas of CVD graphene (to define CVD graphene device channel) and c) liftoff of PMMA resist layers in acetone. Scale bar denotes 20 µm.

3.4 BLACK PHOSPHORUS DEVICES

Chapter 6 and 7 in this thesis are dedicated to submitted work performed on black phosphorus based thermoelectric devices and black phosphorus based photodetector devices. The following sub-chapters will discuss some of the key differences in terms of device fabrication processes as compared to graphene based devices. It is worthy to note that most of the fabrication processes are similar with the main exception that black phosphorus crystals are highly sensitive to ambient environment. Thus, the exfoliation of black phosphorus crystals was performed under inert argon environment in a glove box. All subsequent fabrication

processes external to the glove box were performed with extra care so as to reduce the exposure of these crystals to ambient surroundings. The design of device electrodes with respect to the crystals was prepared accordingly depending on the objective and type of experiments. Instead of employing chromium (Cr)/gold (Au) metal as device contacts, the combination of titanium (Ti)/gold (Au) was used in all black phosphorus based devices[118]. All experiments were performed on black phosphorus crystals with thickness varying from 5 µm to <20 µm.

3.4.1 THERMOELECTRIC

First of all, black phosphorus crystals were obtained by mechanical exfoliation technique as described by the above mentioned method for graphene crystals. Due to the high reactivity of black phosphorus crystals with ambient environment, the mechanical exfoliation of black phosphorus crystals was performed under inert argon environment in a glove box[118]. By using the optical microscope in the glove box, clean and isolated black phosphorus crystals with dimensions of at least 5 µm by 15 µm were selected for further device fabrications. Subsequent device fabrication processes are similar to exfoliated graphene based devices apart from the design of the device electrodes and in the case for this experiment, no etch mask pattering was required.

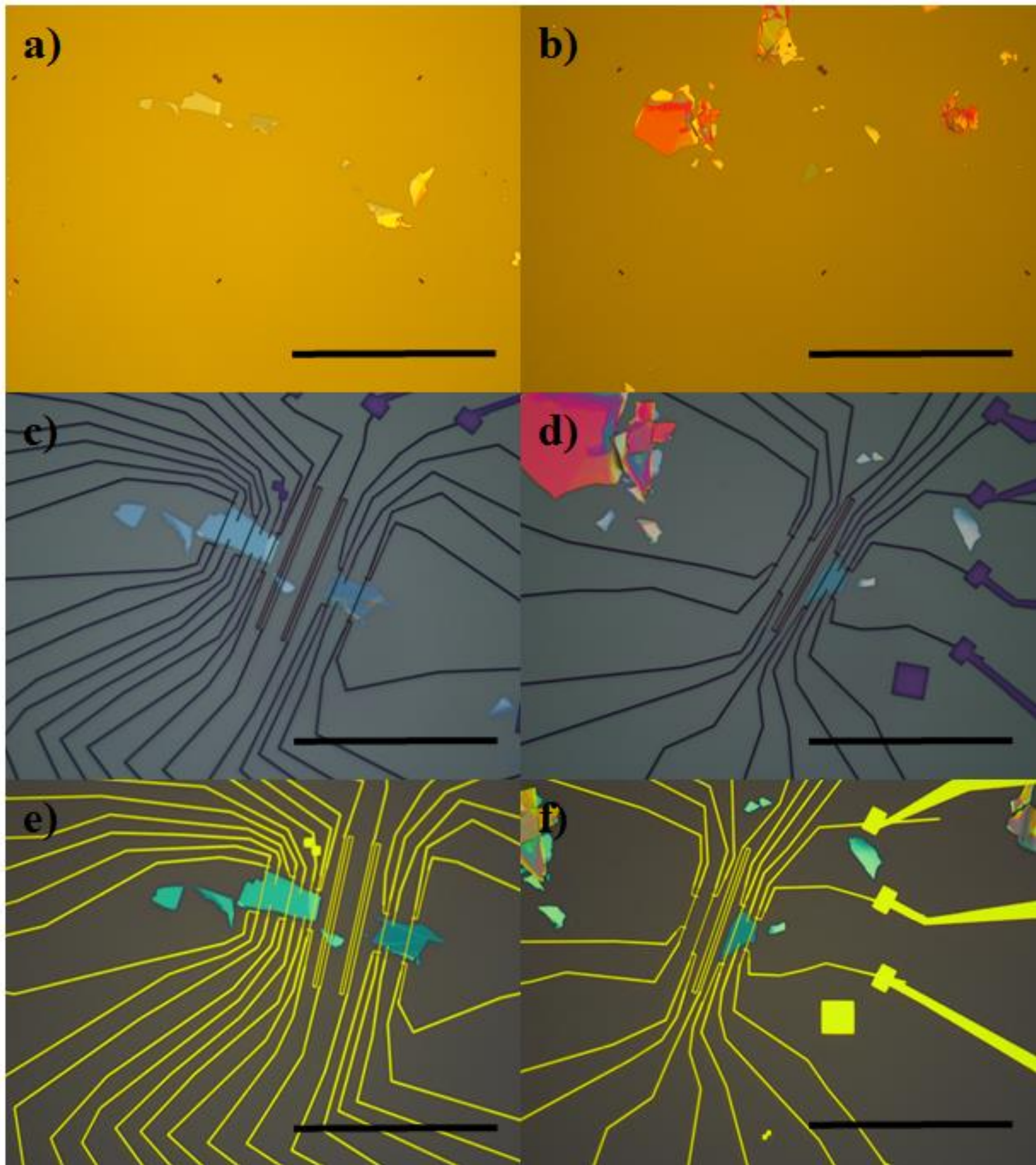

Figure 3- 7: Optical microscope images of few layers black phosphorus taken after a), b) patterning of alignment markers c), d) patterning of device electrodes with the aid of the defined alignment markers and e), f) thermal evaporation of Ti/Au metals and liftoff process. Scale bar in a) and b) is 100 µm and in c), d), e) and f) is 50 µm.

3.4.2 PHOTODETECTOR

The preparation procedures of black phosphorus based photodetector devices were similar to black phosphorus based thermoelectric devices apart from the selection of crystals. For this experiment, a simple two-contact device is sufficient for all measurement purposes. Thus, the selection of crystals can be less stringent in terms of dimensions, in this case a crystal with dimensions of 5 µm by 5 µm can be chosen to make a photodetector device.

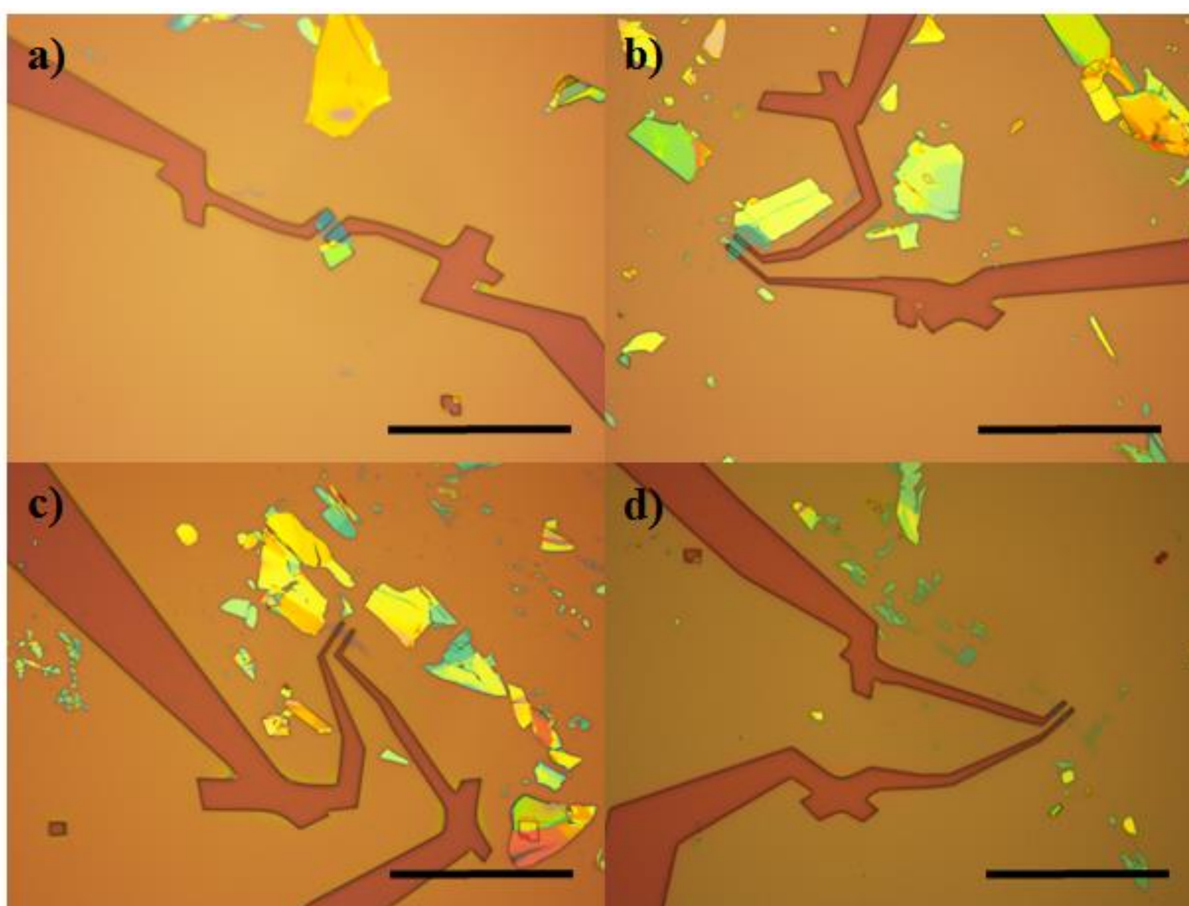

Figure 3- 8: Optical microscope images of four different black phosphorus crystals with patterned electrodes (2-probe devices). Scale bar is 20 µm.

3.5 MEASUREMENT SET-UPS AND TECHNIQUES

This sub-chapter will be dedicated to the description of measurement set-ups and different measurement techniques for different experiments. The measurement protocols for different experiments differ depending on the ultimate objective of each experiment. Some experiments involve low temperature measurements with or without an external magnetic field and others may just need a simple room temperature characterization under high vacuum condition. Thus the following sub-chapters are divided based on the different type of experiments to provide a better understanding for the reader.

3.5.1 MEASUREMENT SET-UPS

Following the completion of device fabrication processes, each device wafer will be pasted onto a 44-pin chip carrier with the aid of silver paste. For the spin Hall Effect devices, additional care has to be implemented in positioning the device with respect to the chip carrier. This is due to the fact that the chip carrier will be finally placed in the cryostat for measurements under external magnetic field. In particular, for spin precession measurements, the direction of the magnetic field with respect to the channel of graphene is important. To create the connection between device electrodes and metal pads on the chip carrier, aluminum wires were used (West bond wire bonder). Device mounted on the chip carrier can then be loaded into a measurement probe for room temperature transport characterization. The choice of measurement probes depends on the type of experiments; whether the experiment needs variable temperature characterizations (1.6 K to 400 K) or parallel/perpendicular external magnetic field (0 T to 16 T). The measurement probe can be pumped down to high vacuum ~$1x10^{-6}$ Torr. For variable temperature measurements, the probe can be inserted to variable temperature insert (VTI) cryostat after room temperature characterizations. The following are the standard measurement equipment used in the electronic characterization of devices; lock-in (SR830) for ac measurements with varying frequencies, lock-in amplifier, Keithley 6430

mainly used for application of gate voltage, Keithley 6221 and Keithley 2400. All measurements are automated and controlled by Python and LabView measurement software.

3.5.2 ELECTRICAL CHARGE TRANSPORT MEASUREMENTS FOR GRAPHENE BASED DEVICES

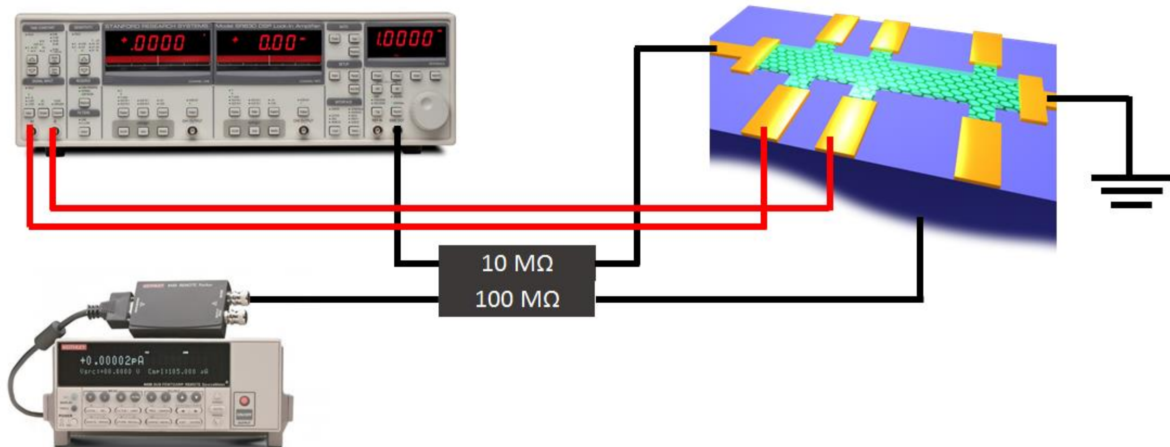

Figure 3- 9: Schematics showing the measurement configurations for local transport, two-probe or four-probe measurements.

Prior to any complex electrical transport characterizations, two-probe measurement technique is applied to characterize the contact resistances of the device electrodes. In this measurement configuration, a constant current is driven into the device channel through the source and drain electrodes. The potential difference between the same pair of electrodes is probed in this configuration. In the case of two-probe measurement, the total potential difference (or resistance, potential divided by the constant current) includes the contribution from the wire resistances, source/drain electrodes and device channel. Typical Cr/Au or Ti/Au metal contacts have resistances in the order of ~1 kΩ. Next, four-probe measurement technique is implemented to measure the channel resistance excluding contributions from contacts and wires by using the standard four terminal configuration. Similar to two-probe measurement, a current is driven into the device through the source and drain electrodes but the potential

difference is detected now via the third and fourth contact, fabricated between the source and drain electrodes. The measurement configurations are illustrated in Figure 3-9.

3.5.3 ELECTRICAL SPIN HALL EFFECT MEASUREMENTS FOR GRAPHENE BASED DEVICES

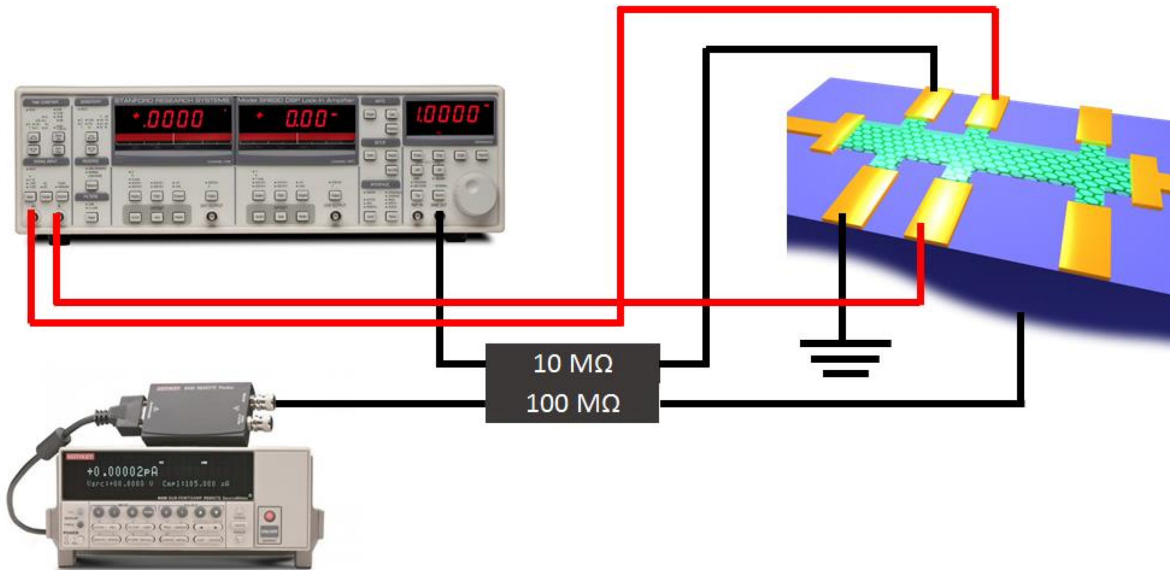

Figure 3- 10: Schematics showing the measurement configuration for non-local transport, spin Hall measurement.

Spin Hall Effect (SHE) is an innovative method to create spin current without the need of a magnetic contact. In SHE measurements, an ac charge current (1-10 μA) is driven from a non-magnetic source contact to the opposite drain contact. A non-local voltage is then measured with the adjacent contact pairs as shown in Figure 3-10. Prior to SHE measurements, the resistivity of graphene channel has to be probed via both the upper and lower contact pairs to ensure the homogeneity of device channel. Detailed measurement procedures will be discussed later on in Chapter 4 and Chapter 5 whereby the experiments rely heavily on SHE measurements.

3.5.4 THERMOELECTRIC MEASUREMENTS FOR BLACK PHOSPHORUS BASED DEVICES

Thermometry:

The thermometry of black phosphorus based thermoelectric devices is characterized by measuring the resistance of the Ti/Au electrodes in a four-probe configuration for temperatures between 10 K and 300 K. These measurements serve as resistive thermometers for determining the local temperature in black phosphorus under a heat gradient, with resolution of about ~10 mK for temperatures above 20 K. By using the thermometry of two pair of Ti/Au electrodes, we can obtain the thermal difference ΔT.

Thermal conductivity:

In addition to the standard thermometry which gives us the local temperature in black phosphorus channel, we have also devised a method which allows us to measure the thermal conductivity of black phosphorus channel. For this we have included in some of our devices, an additional 'ghost device', an electrode structure (without any black phosphorus channel) which mirrors the electrode structure contacting the black phosphorus channel on the opposite side of the heater element. By measuring the local temperature of equivalent thermometers on opposite sides of the same heater element; that is on the black phosphorus channel device and ghost device, we performed a comparative measurement to detect a change in temperature profile due to thermal transport via the black phosphorus channel.

Thermoelectric:

For the thermoelectric measurements, we applied a low frequency ($\omega/2\pi < 5$ Hz) ac signal to the heater element to produce an alternating heat gradient and measured the 2ω thermopower response in black phosphorus due to Joule heating. The thermopower is then obtained as $S = \frac{\sqrt{2}V_{2y}}{\Delta T}$, where V_{2y} is the second harmonic signal, with 90° phase shift, measured

using a lock-in technique with an input impedance of 100 MΩ that allows a large signal to noise ratio (ref).

In Chapter 6, a more detailed measurement procedures on the black phosphorus based thermoelectric devices will be discussed, in all the different aspects of thermal measurements; thermometry, thermal conductivity and thermoelectric.

3.5.5 PHOTODETECTION MEASUREMENTS FOR BLACK PHOSPHORUS BASED DEVICES

All electronic characterizations involved were two-probe measurements, performed at room temperature and under high vacuum condition ~10^{-7} mbar. The resistance of black phosphorus crystals varies from ~1 MΩ to ~1 GΩ, thus dc electrical measurements were better equipped to characterize the charge transport of these devices. For this experiment, dc electrical measurements were supplied by Agilent B2912A. The excitation light source applied throughout the experiments was provided by a monochromatic Xenon light source with tunable wavelengths (see Summary and Future Work).

CHAPTER 4 SPIN HALL EFFECT IN FUNCTIONALIZED GRAPHENE

Graphene[50] the first two-dimensional crystal, is a wonder system with large Young's modulus[52] and low bending rigidity[53]. Its remarkable in-plane mechanical strength permits huge perpendicular strain, even down to the atomic scale. This allows a variety of chemical functionalization, which are not feasible with other two-dimensional systems[35,121,122]. The perpendicular distortion of the in-plane carbon bonds is unique to graphene and may allow for a large enhancement in its otherwise weak intrinsic spin-orbit interaction strength[100].

This enhancement is unlike the spin-orbit (SO) enhancement in metals[123] and semiconductors[29], and is even distinct from the curvature induced SO coupling in carbon nanotubes[124,125]. As the sp3-bond angle depends strongly on the graphene substrate interaction, the functionalization of graphene allows for a controllable SO strength ranging from a few tens of μeV up to 7 meV[100]. This allows the manipulation of electron/hole spins in graphene through spin Hall Effect (SHE)[28,29,89,96,126,127], thus eliminating the need for any magnetic elements or externally applied (local) magnetic fields in the device architecture. The primary objective in this work is to enhance graphene's SO interaction by chemical functionalization of graphene (hydrogenation/fluorination) in order to study the spin transport in this system via SHE.

In this chapter, I will start with the discussion of published work (with me as an equally contributing author) on spin Hall Effect in weakly hydrogenated graphene. This is followed by work in progress on spin Hall Effect in fluorinated graphene.

4.1 COLOSSAL ENHANCEMENT OF SPIN-ORBIT COUPLING IN WEAKLY HYDROGENATED GRAPHENE

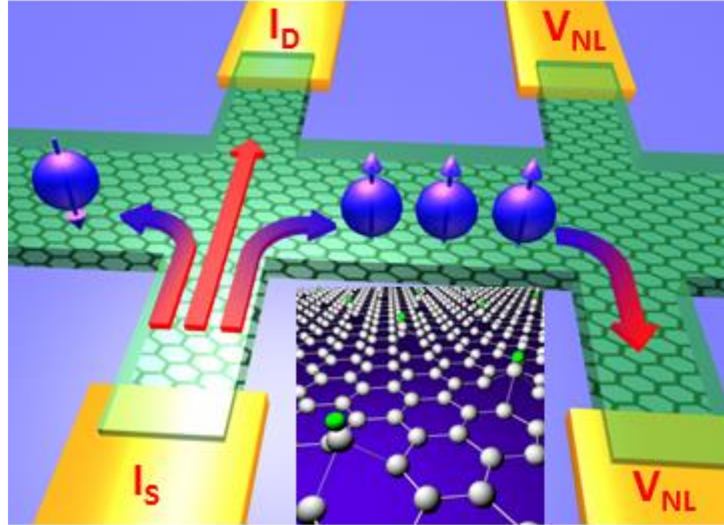

Figure 4- 1: Schematics showing the measurement configuration of non-local spin Hall Effect. Inset: the deformation of graphene lattice from sp2 to sp3 due to hydrogenation.

One of the many shortcomings of graphene is its extremely small intrinsic SO coupling[100]. This prevents many of the fascinating phenomena such as topological/quantum spin Hall states[97,128] and the spin Hall effect[27] (SHE) to be seen in graphene. Recently, it was predicted[36,100,129,130] that the introduction of adatoms in graphene would enhance the SO interaction through the conversion of sp2 to sp3 bonds. However, introducing impurities while keeping graphene metallic, that is, without creating Anderson localization[131], is experimentally demanding. Here, we show that the controlled addition of small amount of covalently bonded hydrogen atoms is adequate to induce a colossal enhancement of the SO interaction by three orders of magnitude. This results in a SHE at zero external magnetic fields at room temperature, with non-local spin signals up to 100 Ω; orders of magnitude larger than in metals[132]. This is, further, directly confirmed by Larmor spin-precession measurements. From this and the length dependence of the non-local signal we extract a spin relaxation length of ~1 μm, a spin relaxation time of ~90 ps and a SO strength of 2.5 meV.

4.1.1 HYDROGENATION OF EXFOLIATED GRAPHENE

We created covalently bonded hydrogen atoms on graphene lattice through the dissociation of hydrogen silsesquioxane (HSQ) resist[133] (see Figure 4-2). The percentage of hydrogenation is determined by Raman spectroscopy[134,135] and gives ~0.01-0.05 % hydrogenation for a HSQ dose in the range 0.4-5 $mCcm^{-2}$ (see Figure 4-3).

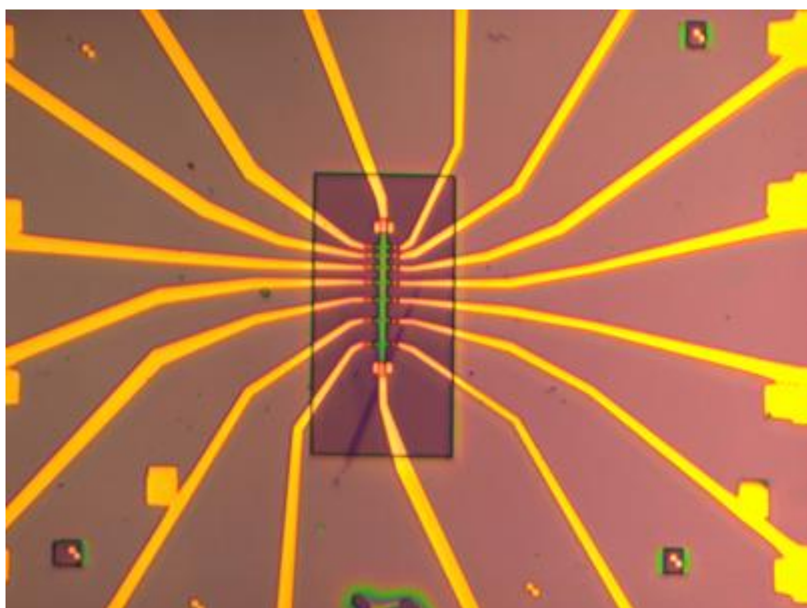

Figure 4- 2: Optical microscope image of an exfoliated graphene device (after thermal evaporation) with hydrogen silsesquioxane (HSQ) resist as etch mask to define the desired Hall bar graphene channel.

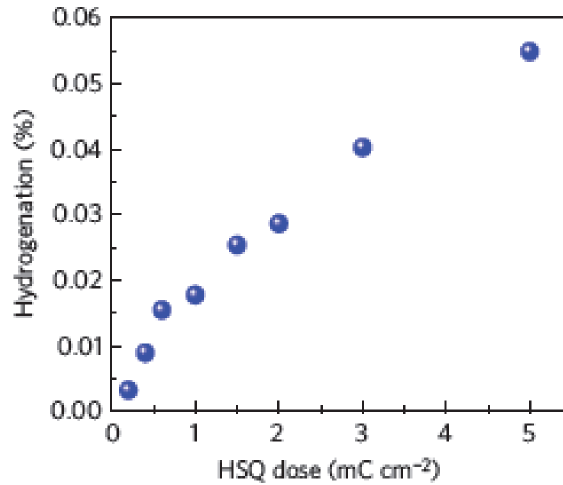

Figure 4- 3: Hydrogenation percentage as a function of irradiation dose of HSQ as obtained from Raman measurements.

Device fabrication and hydrogenation characterization:

The graphene crystals are prepared by mechanical exfoliation of graphite onto a Si/SiO_2 substrate, similar to steps discussed in the previous chapter. The monolayer graphene flakes are first distinguished from their optical contrast, which is then confirmed by Raman spectroscopy. The devices are then fabricated using standard electron beam lithography (EBL). After successful lift-off, a second EBL step is performed to etch the graphene into a Hall bar (or using HSQ resist, see Figure 4-2). For hydrogenation, we introduce small amounts of covalently bonded hydrogen atoms in graphene by coating a graphene Hall bar device with HSQ resist followed by EBL induced dissociation of HSQ resulting in the basal plane hydrogenation of graphene[133]. This approach has a number of advantages over the hydrogenation of graphene using radio frequency (RF) hydrogen plasma[121,134]; 1) provides hydrogenation without introducing vacancies, 2) degree of hydrogenation can be precisely controlled and kept minimal and 3) enables EBL controlled local hydrogenation in the sub-micron range. The evolution of the D peak in the Raman spectrum (see Figure 4-4) is a clear

indication for the progressive hydrogenation of graphene with increasing EBL dose. To study the increase in hydrogenation percentage, the device is exposed to varying doses of EBL (1-8 $mCcm^{-2}$).

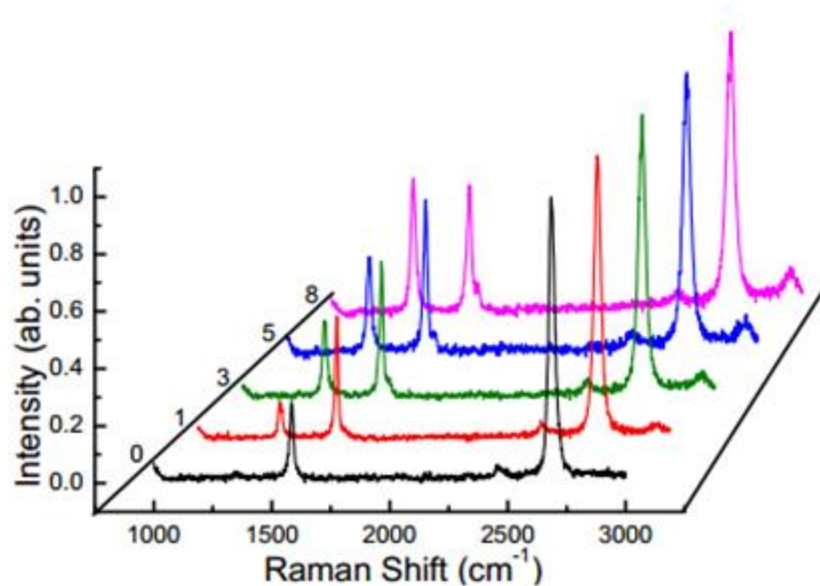

Figure 4- 4: The evolution of D peak in the Raman spectrum showing progressive hydrogenation percentage in graphene with increasing irradiation dose of HSQ.

The hydrogenation of the underlying graphene can be confirmed; 1) from the decrease in the intensity of the Si-H peak due to the dissociation of hydrogen from HSQ with EBL and 2) from the change in the I_D/I_G ratio of the Raman peaks with annealing in argon ambient[133]. Figure 4-5 a) shows the Si-H peak intensity for as coated HSQ and HSQ samples irradiated with EBL doses 400 μCcm^{-2} and 1000 μCcm^{-2}. The gradual decrease in the Si-H peak intensity with EBL dose is a clear sign of the dissociation of the hydrogen. This coupled with the increase of the D-peak intensity with EBL dose indicates to the hydrogenation of the graphene lattice. Moreover, a decrease in the I_D/I_G ratio after annealing at 250 °C in argon environment for 2 hours also confirm that the effect of EBL irradiation of HSQ is primarily in the hydrogenation of graphene and the introduction of vacancies is negligible (see Figure 4-5 b)).

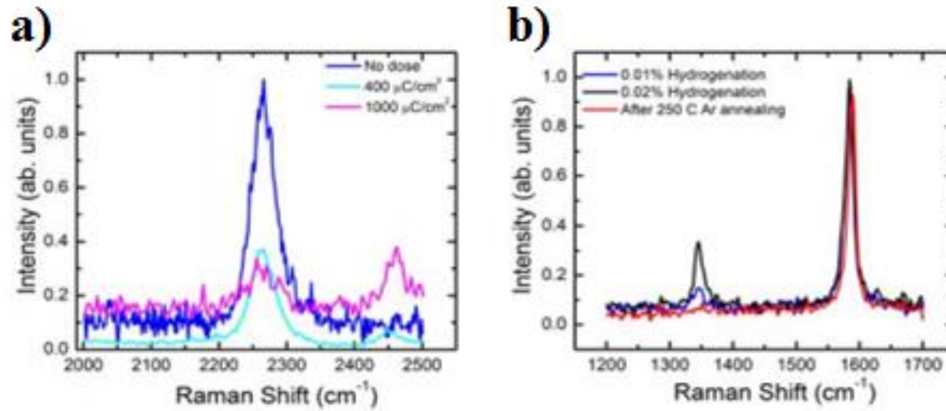

Figure 4- 5: a) Change of Si-H peak at 2265 cm^{-1} as a function of irradiation dose. The peak intensity decreases with increasing dose indicating the dissociation of hydrogen from HSQ. b) Raman spectrum of a hydrogenated graphene SHE device showing the reversibility of hydrogenation upon annealing in argon environment at 250 °C for 2 hours. Constant gas flow of argon was maintained during annealing process ~0.3 lmin^{-1}. The disappearance of D peak after annealing shows that HSQ irradiation creates minimal vacancies/defects to graphene lattice.

Estimation of impurities concentration:

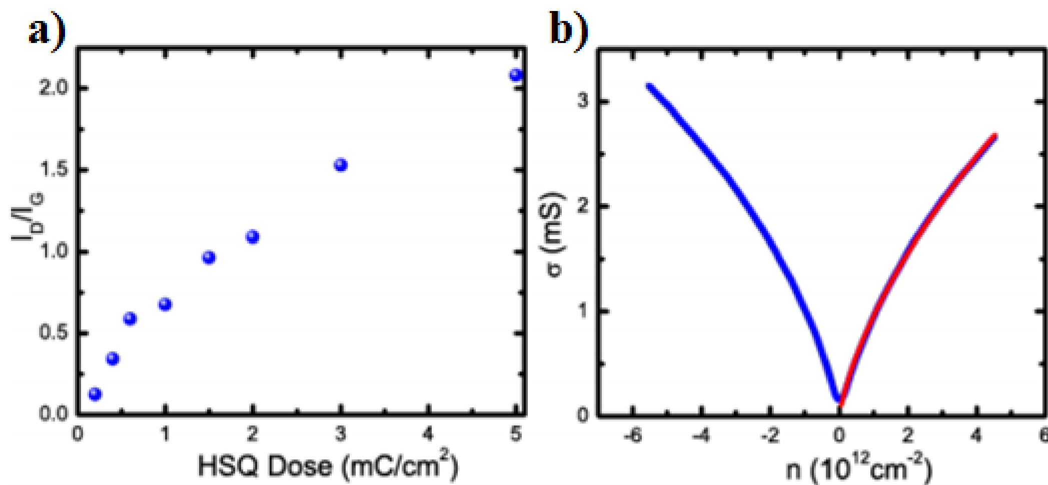

Figure 4- 6: a) Increment of I_D/I_G Raman peak ratios of graphene coated with HSQ irradiated with increasing EBL dose. b) σ versus n plot for one of these devices irradiated with EBL dose

of 1 mCcm^{-2}. The red curve is a fit to the plot with resonant scatters which gives an impurity density of 1×10^{12} cm^{-2}.

The concentration of the hydrogen can be estimated via two methods: 1) from the Raman spectroscopy or 2) from the transport characterization. We start with the estimation from Raman data. The concentration of impurities n_{imp} can be estimated from the I_D/I_G ratio (see Figure 4-6 a)) of the Raman peaks evaluated by irradiating the graphene/HSQ sample with different EBL dose. From the I_D/I_G ratio and the spacing between the hydrogen atoms, the impurities concentration can be calculated using the relations[135]:

$$L_D^2(nm^2) = (1.8 \pm 0.5) \times 10^{-9} \lambda_L^4 \left(\frac{I_G}{I_D}\right), \quad (4.1)$$

$$n_{imp}(cm^{-2}) = \frac{10^{14}}{\pi L_D^2}, \quad (4.2)$$

Here, L_D is the separation between hydrogen atoms, $\lambda_L = 514\ nm$ is the wavelength of the Raman excitation laser, I_G and I_D are the Raman G-peak and Raman D-peak intensities respectively.

The I_D/I_G ratio for 1 mCcm^{-2} and 3 mCcm^{-2} of HSQ dose, gives L_D ~13 nm and 9 nm, n_{imp} ~0.9×10^{12} cm^{-2} and ~1.6×10^{12} cm^{-2} respectively. We can also estimate the fraction of hydrogen impurities via the following equation:

$$\%\ hydrogenation = \left(\frac{3\sqrt{3}}{\pi}\right)\left(\frac{a}{L_D}\right)^2 \times 100. \quad (4.3)$$

Using the values of L_D for 1 mCcm^{-2} and 3 mCcm^{-2} of HSQ dose, the calculated percentages of hydrogen impurities are 0.02 % and 0.05 % respectively. In order to verify the validity of these results, we can also estimate the percentage of hydrogenation through the transport data. Figure 4-6 b) shows the conductivity versus n data for the HSQ graphene sample with EBL irradiated dose of 1 mCcm^{-2}. The conductivity due to resonant scatterers in graphene is given by the following equation:

$$\sigma = \left(\frac{4e^2}{h}\right)\left(\frac{k_F{}^2}{2\pi n_{imp}}\right) ln^2(k_F R), \tag{4.4}$$

where $k_F = \sqrt{\pi n}$ is the Fermi wave vector, n_{imp} is the impurity concentration and R is the impurity radius.

By fitting the data with this equation we can obtain n_{imp} ~1.2×10^{12} cm^{-2} and ~2×10^{12} cm^{-2} for 1 mCcm^{-2} and 3 mCcm^{-2} HSQ dose respectively. Next, the percentage of hydrogenation can be calculated from ~$\left(\frac{n_{imp}}{n_c}\right) \times 100$. The percentages obtained are 0.025 % and 0.05 % for lower and higher EBL irradiation dose respectively, which are consistent with the above values estimated from Raman characterization.

Our studies focus on samples that are only weakly hydrogenated, because hydrogen atoms are predicted to cluster at higher densities[136]. In such samples, our spin-transport measurements both at room temperature and low temperatures show a large non-local signal in the absence of any externally applied magnetic fields. By studying the length, width, impurities density and in-plane magnetic field dependence of the spin signal, we can estimate the SO coupling strength Δ_{SO}, the spin relaxation length λ_s and the spin relaxation time τ_s.

4.1.2 ELECTRICAL CHARGE AND SPIN CHARACTERIZATION

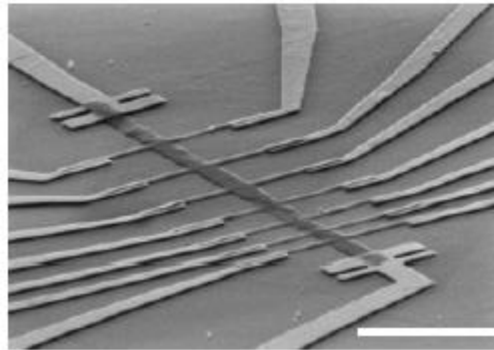

Figure 4- 7: Scanning electron micrograph of a hydrogenated graphene hall bar device showing multiple junctions with different lengths. Scale bar denotes 5μm.

Charge and spin transport are characterized in graphene Hall bar devices. The scanning electron micrograph of one such device with multiple Hall bar junctions is shown in Figure 4-7. The room-temperature local resistivity ρ and the non-local resistance R_{NL} measurements for the exfoliated pristine graphene device with length L=2 μm and width W=1 μm are shown in Figure 4-8.

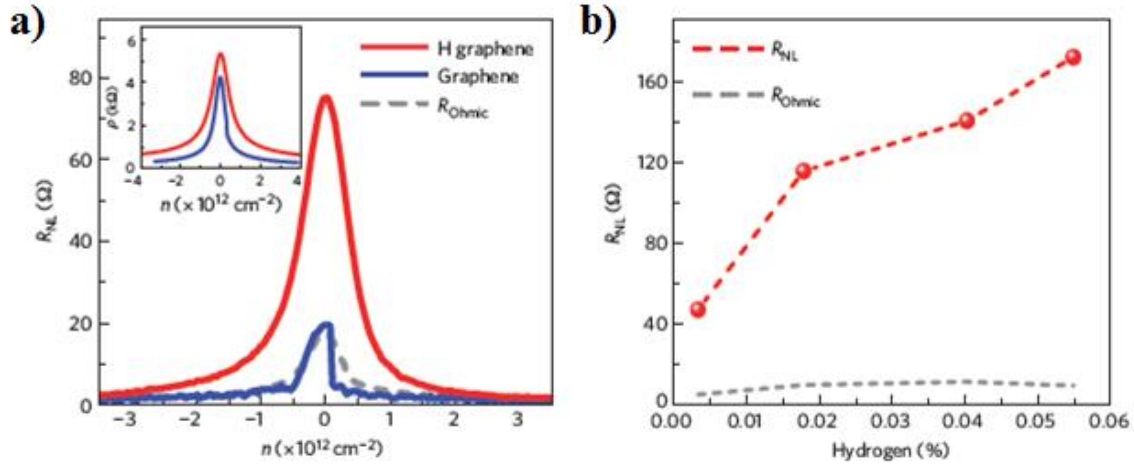

Figure 4- 8: a) Non-local signal versus n for pristine graphene sample and hydrogenated graphene sample at room temperature. The dashed grey line denotes the ohmic contribution to the measured signal. Inset: resistivity versus n for pristine and hydrogenated graphene. b) Non-local signal dependence on hydrogenation percentage. The dashed grey line denotes the calculated ohmic contribution for this device.

The presence of a finite R_{NL} at zero fields is not intriguing, because it is comparable to the estimated ohmic contribution R_{Ohmic}[92,93]:

$$R_{Ohmic} = \rho e^{\frac{-\pi L}{W}}. \tag{4.5}$$

However, already after very weak hydrogenation ~0.02 %, we observe a ~400 % increase in R_{NL} (Figure 4-8 a)), well above what can be accounted for by R_{Ohmic}. With increasing hydrogenation the measured R_{NL} shows a steep increase, reaching 170 Ω at 0.05 % hydrogenation (Figure 4-8 b)). A strong increase of the R_{NL} is observed even at charge densities

>1×10^12 cm^-2. These results are reproduced consistently in ~20 junctions in 5 different devices. As the ohmic contribution to R_{NL} remains negligible over the entire hydrogenation rate (Figure 4-8 b)), the only plausible explanation for the observed physical phenomenon (in the absence of an applied field and at room temperature) is the SHE.

4.1.3 MAGNETIC FIELD MEASUREMENTS

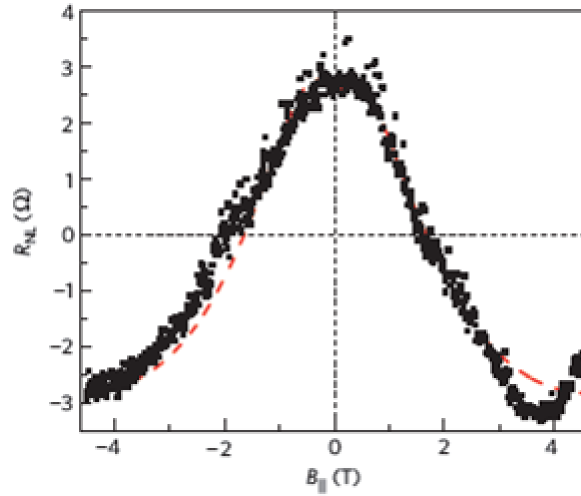

Figure 4- 9: Parallel field precession curve for device with L/W=5 and mobility of ~20,000 $cm^2V^{-1}s^{-1}$. The red dashed line is the fit to measurement data.

Next we study the in-plane magnetic field sweeps, where only the presence of spin-polarized current can give an oscillating signal[93]. For this configuration the non-local signal has been predicted to oscillate in a magnetic field range given by the Larmor frequency $\omega_B = \Gamma B \leq \left(\frac{D_s}{W^2}\right)$, where Γ is the gyromagnetic ratio, B is the applied magnetic field, D_s is the spin diffusion coefficient and W is the width of the sample.

For this, devices with higher mobility (higher D) and smaller W are selected so that the condition $W<\lambda_s$ is satisfied and the variation in the spin polarization across the strip is negligible[93]. Figure 4-9 shows the in-plane field dependence of R_{NL} for the device with 0.01 %

hydrogenation at T=4 K (mobility~20,000 $cm^2V^{-1}s^{-1}$ and *L/W*=5). We can obtain many important spin parameters by fitting this non-local oscillation with the following equation[93]:

$$R_{NL} = \frac{1}{2}\gamma^2 \rho W Re\left[\left(\frac{\sqrt{1+i\omega_B\tau_s}}{\lambda_s}\right) e^{-\left(\frac{\sqrt{1+i\omega_B\tau_s}}{\lambda_s}\right)|L|}\right], \quad (4.6)$$

where γ is the spin Hall coefficient.

From the fitting (see Figure 4-9), we obtained λ_s~1.6 μm and γ~0.18 and it should be noted that such an oscillatory behavior is absent for clean pristine graphene devices. Therefore, the oscillatory behavior of R_{NL} is a direct proof of both the SHE arising from the hydrogenation of the graphene lattice and the enhancement of an otherwise negligible SO coupling of graphene.

4.1.4 ADDITIONAL NON-LOCAL STUDIES AND SPIN-ORBIT COUPLING STRENGTH

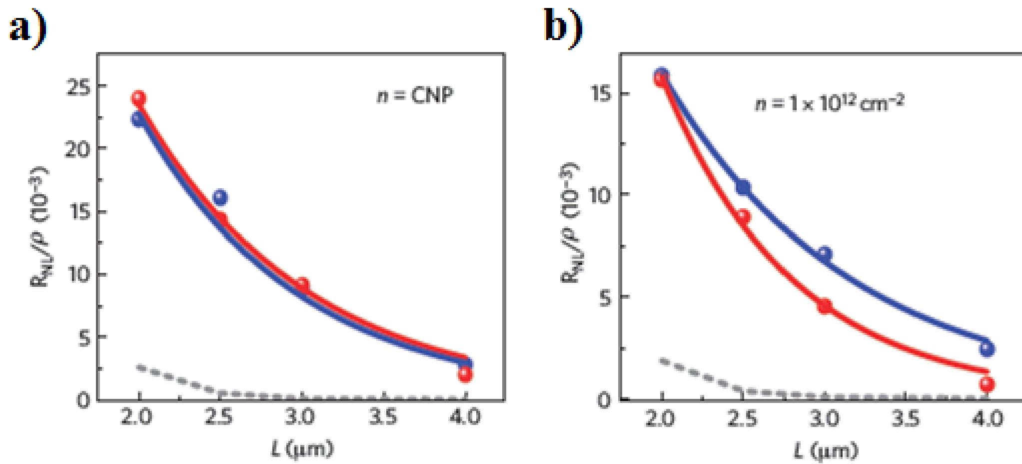

Figure 4- 10: Length dependence of non-local signal at room temperature (red solid circle: 0.02 % hydrogenation and blue: 0.05 % hydrogenation). a) At CNP. b) At n=1×10^{12} cm^{-2}. The solid lines are the fit for the measurement data and dashed grey line is the calculated ohmic contribution.

Further to the magnetic field dependence, we also employed the length and the width dependence to confirm that the origin of the non-local signal in weakly hydrogenated graphene samples is due to the SHE. We first discuss the length dependence by keeping W=1 μm constant. Figure 4-10 a) and b) show the length dependence of R_{NL}/ρ, both at the charge neutrality point (CNP) and at $n=1\times10^{12}$ cm^{-2}, for the same sample hydrogenated first to 0.02 % and then to 0.05 %. This graphene device has mobilities of 1600 $cm^2V^{-1}s^{-1}$ and 900 $cm^2V^{-1}s^{-1}$ for 0.02 % and 0.05 % hydrogenation respectively. At zero applied magnetic field the equation for the oscillation of non-local signal, for a device with length L and width W, becomes[92,93]:

$$R_{NL} = \frac{1}{2}\gamma^2\rho\frac{W}{\lambda_s}e^{\frac{-L}{\lambda_s}}. \quad (4.7)$$

By fitting the R_{NL}/ρ versus L curve using this simplified equation, we determine λ_s~(0.95±0:02) μm and γ~0.58 at CNP and λ_s~(1.12±0:06) μm and γ~0.45 at n=1×10^{12} cm^{-2}. These results are consistent with the results from conventional lateral spin-valve[31,75,76] devices for hydrogenated graphene with ferromagnetic contacts[137].

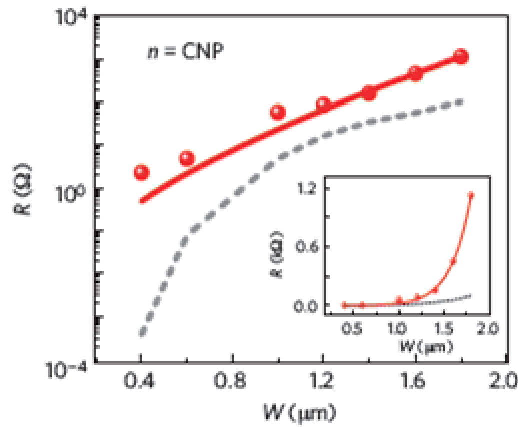

Figure 4- 11: Width dependence of non-local signal at room temperature. Length L=2 μm, red solid line is the fit to the measurement data and dashed grey line is the calculated ohmic contribution. Inset: width dependence on a linear scale.

Next we study the width dependence of the non-local signal at a fixed length L=2 μm (see Figure 4-11). After 0.01 % of hydrogenation, this device shows a mobility of 14,000 cm^{2}V^{-1}s^{-1} at room temperature. In high mobility samples, the width dependence of the SHE signal shows a power-law dependence. The R_{Ohmic}, on the other hand, depends on the width as $exp(-\pi L/W)$ and is orders of magnitude smaller. The distinction between R_{NL} and R_{Ohmic} is most apparent at the smallest width (400 nm). This is in good agreement with the theoretical prediction for narrow channels[93]. The observed width dependence can also be well described by the theoretical model for clean quantum wires[138], that is, for high-mobility devices in the limit $W<\lambda_{SO}$, where λ_{SO} is the spin-precession length. For most of the devices, the width of the graphene channel ranges from 0.4 μm to 1.8 μm; this requirement is easily fulfilled, because in our devices λ_{so}~8 μm.

Further explanation on width dependence data:

The width dependence of the non-local signal (see Figure 4-12) in higher mobility devices shows a super-linear dependence. In such samples the finite width W is related to the spin relaxation length λ_s through:

$$\lambda_s(W) = \frac{{\lambda_{SO}}^2}{W}, \tag{4.8}$$

where λ_{SO} is the spin precession length.

Spin precession length is defined as the length scale in which an electron spin precesses a full cycle in a clean ballistic two-dimensional electron system[138]. This length scale λ_{SO} remains constant as long as the width W of the wire is less than λ_{SO}[138]. For such devices, the relation for the non-local signal can be written as:

$$R_{NL} = \frac{1}{2}\gamma^2\rho\frac{W^2}{{\lambda_{SO}}^2}e^{\frac{-LW}{{\lambda_{SO}}^2}}. \tag{4.9}$$

For the case of $W<<\lambda_{SO}$, the expression can be Taylor expanded in W to:

$$R_{NL} = \frac{1}{2}\gamma^2\rho\frac{W^2}{{\lambda_{SO}}^2}\left[1 - \frac{LW}{{\lambda_{SO}}^2} + \cdots\right]. \tag{4.10}$$

The non-local signal has a power law dependence in W and a log-log plot of R_{NL} versus W should give a straight line. Figure 4-12 shows the log plot for the same data shown in Figure 4-11. The figure clearly shows that the measured signal follows the expected linear dependency for non-local signal and the fitting gives a self-consistent value for λ_{SO}~8 μm. It should also be noted that if the dominant signal came from ohmic contribution, we should have seen a non-linear grey curve.

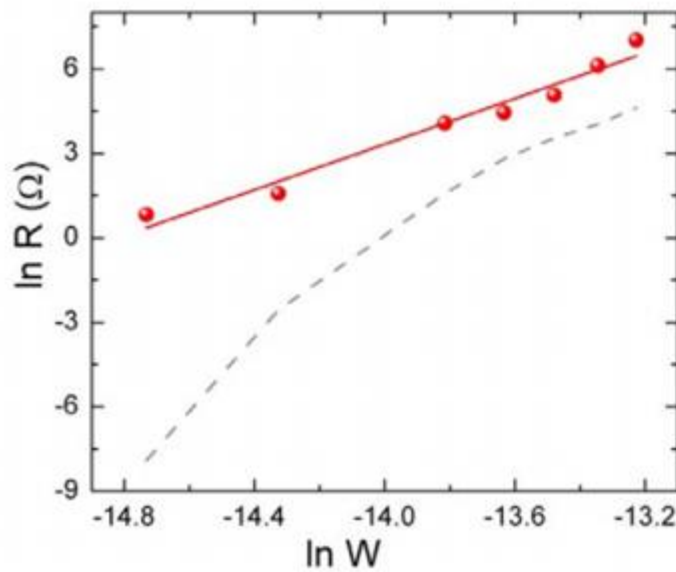

Figure 4- 12: A plot of ln R versus ln W showing the power law dependence of the measured non-local signal with width W. This power law dependence signifies that the measured signal is due to SHE. The dashed grey line denotes calculated ohmic contribution.

We next evaluate other important spin parameters such as the τ_s and the Δ_{SO}. In hydrogenated graphene, the dominant spin relaxation is predicted to be the spin dephasing due to Elliott-Yafet scattering[100]. In the Elliott-Yafet mechanism, spin relaxation time is defined as[101,139]:

$$\tau_s = (\frac{\varepsilon_F}{\Delta_{SO}})^2 \tau_p, \tag{4.11}$$

where ε_F is the Fermi energy and τ_p is the momentum relaxation time.

By substituting the value for τ_p, $\tau_s = \frac{{\lambda_s}^2}{D} = 90\, ps$ (D is the diffusion coefficient obtained from the R versus n curve) and ε_F at n=1×10^{12} cm^{-2}, we estimate Δ_{SO} to be ~(2.5±0.2) meV for hydrogenated graphene. Remarkably this is three orders of magnitude higher than the value predicted for pristine graphene.

Finally, we identify the dominant scattering mechanism for the observed spin Hall Effect[71]. For the side-jump mechanism the spin Hall resistivity ρ_{SHE} is independent of n_{imp}, whereas for the skew-scattering mechanism $\rho_{SHE} \propto n_{imp}$. The spin Hall resistivity ρ_{SHE} is estimated from:

$$\gamma = (\sigma_{SHE}/\sigma) = \left(\frac{\rho}{\rho_{SHE}}\right). \quad (4.12)$$

The value of ρ_{SHE} changes from 12.9 kΩ to 14.2 kΩ for 0.02 % and 0.05 % hydrogenation respectively. The value of ρ_{SHE} thus, depends weakly on n_{imp} (n_{imp}~0.9×10^{12} cm^{-2} for 0.02 % hydrogenation and ~1.6×10^{12} cm^{-2} for 0.05 % hydrogenation). From these values, they suggest that the dominant mechanism in these hydrogenated graphene device is the side-jump mechanism[71].

We have demonstrated that the SO strength in pristine graphene can be greatly enhanced by introducing a small percentage of covalently bonded hydrogen atoms, without a significant suppression of the conductivity. Hydrogenated graphene has been used as a model system to demonstrate that this leads to a strong SHE. This is confirmed by the non-monotonic oscillatory behavior of the non-local signal in an applied in-plane magnetic field and also by the length, width and impurities density dependence of the non-local signal. From the length dependence of the non-local signal, we extract a spin relaxation length of ~1 μm, a spin relaxation time of ~90 ps and a SO coupling strength of ~2.5 meV for 0.05 % hydrogenated graphene devices. These findings are crucial for the development of graphene-based spintronics applications, as the need for magnetic elements is eliminated from the device

architecture. Last but not least, the demonstration of the non-local SHE due to impurity atoms in graphene is a major step in the realization of a robust 2D topological states[36] and a SHE based spin transistor at room temperature.

4.2 SPIN HALL EFFECT IN SEMI-IONIC FLUORINATED GRAPHENE

Similar to the previous sub-chapter, spin Hall Effect in functionalized graphene has been studied and in this case the system we will be looking at is fluorinated graphene. Promising results from published work on hydrogenated graphene has led us to further study this effect in fluorinated graphene, and also since the latter has larger spin-orbit coupling induced band splitting due to larger intrinsic spin-orbit coupling of fluorine atom[130].

Brief background:

Graphene has enticed extensive scientific research due to its remarkable electronic and mechanical characteristics resulting from hexagonally arrayed sp2-hybridized atomically thick carbon lattice[56,140]. Technologically, graphene has been introduced in applications such as transistors and flexible transparent electrodes[56,141]. Graphene can be changed from being an insulator to semimetal by decoration/re-decoration of adatoms/molecules on the surface. One of the first derivatives of graphene is “graphane”, which has a compressed stoichiometric crystal structure with hydrogen atom attached to every carbon atom. Graphane exhibits metal-insulator transition and mid-gap states as a function of (1/T)[121]. Theoretical predictions show that not only hydrogen but also fluorine is a potential candidate for creation of bandgap in graphene[122]. Geim et al. reported that fluorographene is a high-quality insulator (resistivity > 10^{12} Ω) with an optical gap of 3 eV and is stable up to 400 °C under ambient conditions[122]. Other researchers have shown similar electrical insulating properties of fluorographene through atomic fluorine exposure. The resistivity of fluorographene was significantly changed by

fluorination/de-fluorination processes[142] but the proposed techniques require long process times[122,142]. Most importantly, after the de-fluorination process, reduced fluorographene possessed poor conducting property (> 10^5 Ω/sq) similar to reduced graphene oxide[142–146] due to strong covalent C-F bonds which can cause the defect during de-fluorination.

In this experiment, we introduced an innovative "semi-ionic" C-F bond to graphene which consists of strong covalent C-F bond and easily controllable ionic C-F bond[147]. The semi-ionically fluorinated graphene (s-FG) film was synthesized by one-step functionalization process. The thin s-FG film device shows a diametrical property in electrical investigation through selective ionic C-F bonds elimination.

4.2.1 PREPARATION OF FLUORINATED GRAPHENE

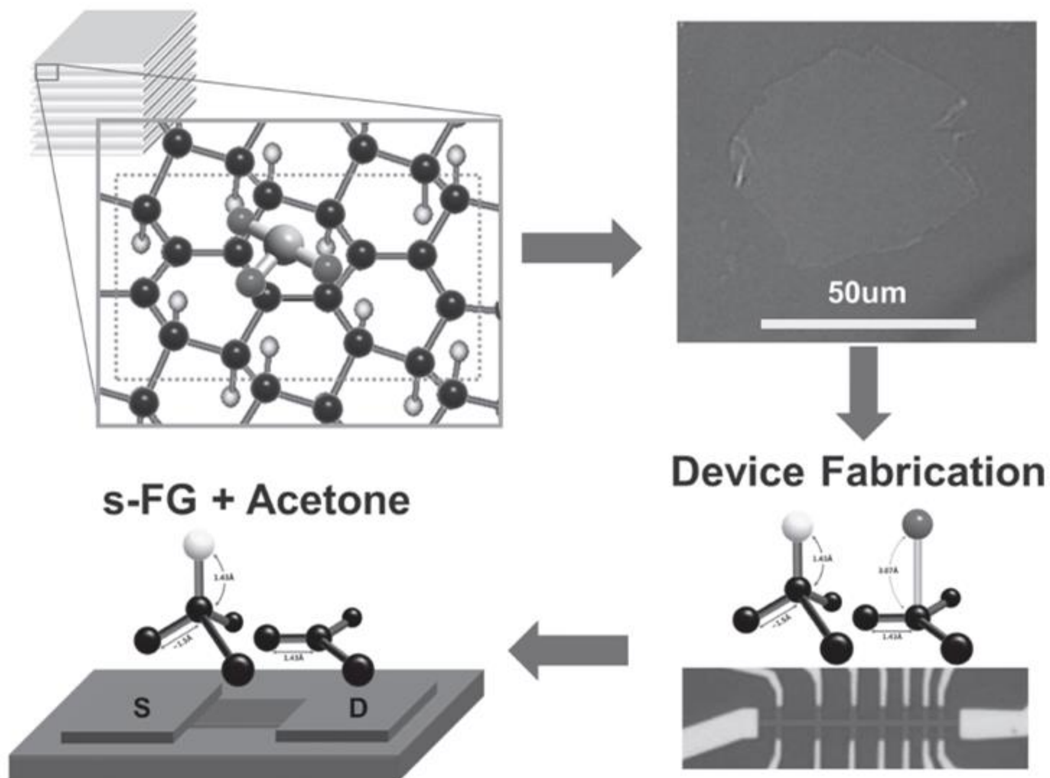

Figure 4- 13: Schematics representation of the s-FG based device fabrication and reduction process; schematics of s-FG and reduced s-FG strucures. Scale bar is 50 μm.

Figure 4-13 summarizes the experimental procedures used to fabricate the s-FG based device for transport measurements. The s-FG was synthesized using the single functionalization and intercalation process with ClF_3. The s-FG contains inorganic volatile intercalating agent ClF_3 with molecular formula $C_2F.nClF_3$ as reported elsewhere[148]. Five grams of pure natural graphite was added to cold liquid ClF_3 in a Teflon reactor and kept for intercalation and fluorine functionalization for 5 h. Later, excess ClF_3 was removed, and the graphite compound with a composition of $C_2F.0.13ClF_3$ was obtained. The obtained s-FG is golden in color and the composition in mass % is C 44.22; F 44.79; Cl 12.49. Using the mechanical exfoliation method, we have succeeded in obtaining s-FG films of several tens of micrometers in size onto the p-type doped silicon substrates covered with a thermally grown 300 nm thick SiO_2 layer. After s-FG transfer, hall-bar geometry devices were fabricated followed by the reduction process with acetone at room-temperature.

4.2.2 ELECTRICAL CHARGE CHARACTERIZATION

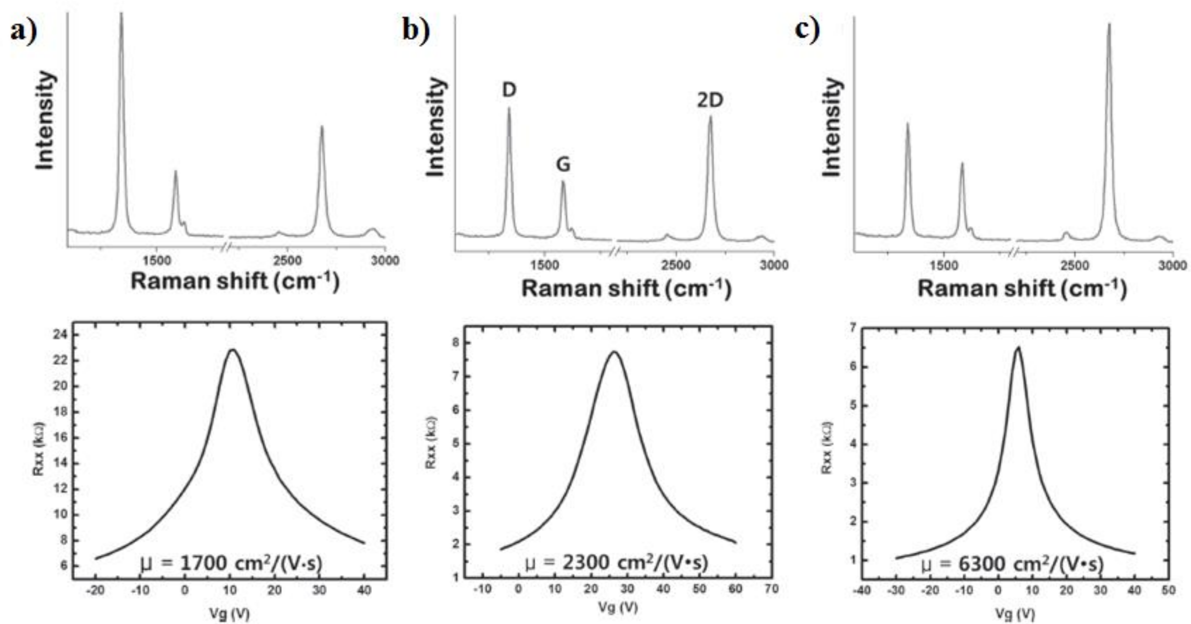

Figure 4- 14: Raman characteristics and resistance versus back gate voltage of reduced single layer s-FG device, a) as prepared, b) intermediate reduction and c) one week reduction.

For systematic charge transport studies, we fabricated hall bar devices of single-layered s-FG using electron beam lithography (EBL) technique. All transport measurements are performed with a four-probe ac lock-in technique under room temperature and vacuum environment. The mobility of single layered s-FG depends on its fluorination state. The mobility increases with increasing ratio of I_{2D}/I_D intensity peaks in Raman spectra (see Figure 4-14).

4.2.3 ELECTRICAL SPIN CHARACTERIZATION

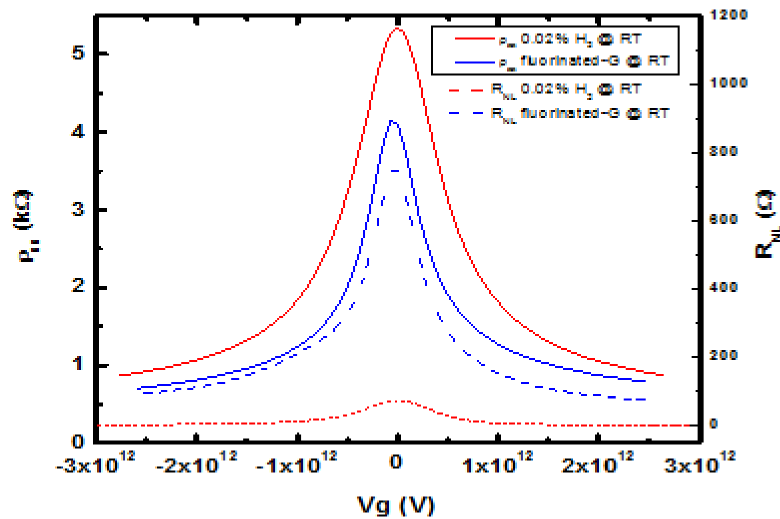

Figure 4- 15: Local (solid line) and non-local (dashed) signal dependence on back gate voltage V_g at room temperature. For comparison both hydrogenated graphene (red) and fluorinated graphene (blue) are plotted. Both devices have length to width ratio of L/W=1.5.

Prior to SHE measurements, these devices are first characterized by using local charge transport experiments to confirm the homogeneity of these flakes. Local charge transports are performed for top and bottom electrodes in a single hall bar junction. These measurements are then extended to the entire device; selecting only the junctions that show similar top and bottom local contributions. Figure 4-15 shows the back gate voltage V_G dependence of the local s-FG

resistivity ρ as determined by $\rho = \frac{Rw}{l}$ where w is the width of graphene channel and l is the spacing between the electrodes. From these measurements, field effect mobility of these flakes is calculated to be in the range of μ~4,000-11,000 $cm^2V^{-1}s^{-1}$ depending on the degree on fluorination. To measure the SHE, we employed the non-local measurement configurations on the homogeneous junctions selected. The non-local resistance R_{NL} as a function of back gate voltage V_G is also shown in Figure 4-15. The fact that we are able to detect a non-local signal is not at all surprising because it has been shown previously that in pristine graphene, this signal is equal to the ohmic leakage contribution[1] $R_{NL} = \rho e^{-\frac{\pi L}{W}}$. In this s-FG device, the non-local signal increases up to about 800 Ω at the charge neutrality point (CNP), orders of magnitude higher than the leakage contribution. The presence of this non-local signal at room temperature and zero magnetic field can only be due to SHE.

Initial SHE results on fluorinated graphene have been promising and further experiments such as length/width dependence and spin precession under parallel external magnetic field have to be performed before we can discuss on spin-orbit coupling strength Δ_{SO} induced by fluorination. However looking at the initial non-local studies of these fluorinated graphene hall bar devices, it is not surprising that the induced spin-orbit coupling is in the order of few meVs similar to previous reported work on hydrogenated graphene. In conclusion, we have successfully enhanced spin-orbit interaction in graphene lattice through chemical functionalization with the aim of studying its spin transport via the SHE. However, with chemical functionalization, the process is proven to be reversible, the enhancement is unstable upon annealing treatment. In the next chapter, we will discuss another more ‘permanent’ technique in enhancing graphene’s spin-orbit which proceeds through an entirely different mechanism.

CHAPTER 5 GIANT SPIN HALL EFFECT IN GRAPHENE GROWN BY CHEMICAL VAPOUR DEPOSITION

Development in large-area graphene growth via chemical vapour deposition (CVD) on metals like copper was crucial in the demonstration of graphene-based novel, wafer-scale electronic circuits and proof-of-concept applications such as flexible touch panels. In this chapter, we show that graphene grown by CVD on copper is equally promising for spintronics applications. In contrast to pristine graphene, our experiments demonstrate that chemically grown graphene has a huge spin–orbit coupling (SOC) ~20 meV giving rise to a giant spin Hall Effect (SHE). The extraordinarily large spin Hall angle ~0.2 provides an important step towards graphene-based spintronics devices within existing complementary metal-oxide-semiconductor technology. Our microscopic model shows that unavoidable residual copper adatom clusters act as local spin–orbit scatterers and, in the resonant scattering limit, induce transverse spin currents with enhanced skew-scattering contribution. Our findings are confirmed independently by introducing metallic adatoms-copper, silver and gold on exfoliated graphene samples.

Spintronics has been crucial in developing magnetic recordings and high density magnetic memory devices[3,149]. The next stage of exploration in this field is the demonstration of gate tunable control of spin currents for spin-based transistor and spin transfer torque based memory applications[150]. Key to the realization of such devices are materials with long spin relaxation times and gate tunability[151]. Graphene is an ideal material, if methods, which do not require chemical functionalization, to enhance its weak SOC are devised[1]. The recent predictions of proximity enhanced SOC in graphene decorated with metallic adatoms, where electrons tunnel from graphene to adatoms and back, thereby locally enhancing the SOC, open up a new path[36,152–155]. The proximity-induced SOC in graphene decorated with physisorbed metallic adatoms is unique and different from functionalized graphene. In the latter case, the

lattice distortion of sp3 hybridization results in the enhancement of SOC by Rashba[100] and sub-lattice inversion asymmetric[156] spin–orbit interactions. On the other hand, physisorbed metallic adatoms preserve the sp2 bond character of graphene and mediate diverse spin–orbit interactions through electron tunnelling onto and off the adatoms[157], including z→-z symmetric (intrinsic-type) and z→-z asymmetric (Rashba-type) SOC[36,157]. Adatom proximity induced SOC over the nanometre scale avoids inter-valley scattering and offers a realistic route towards two-dimensional (2D) topological insulator (TI) state engineering in graphene. The realization of such a quantum spin Hall/TI state in conjunction with the electric field effect in graphene is of great significance since TIs proximity coupled to superconductors are predicted to host Majorana fermions; an essential step towards topological quantum computations[36]. Most importantly, the detection of spin-polarized currents on the surface of TIs is a formidable task that requires the experiment to be performed in the ballistic transport regime[96,158]. Hence, systems with large electron mean free path in the ballistic transport regime are required. Graphene, with its ultra-high mobility even at room temperature[159], is thus an ideal candidate for the direct experimental detection of spin-polarized currents at elevated temperatures, which until now has only been observed in 2D HgTe quantum wells at low temperatures[96].

5.1 CVD GRAPHENE AND EXFOLIATED GRAPHENE DECORATED BY METALLIC ADATOMS

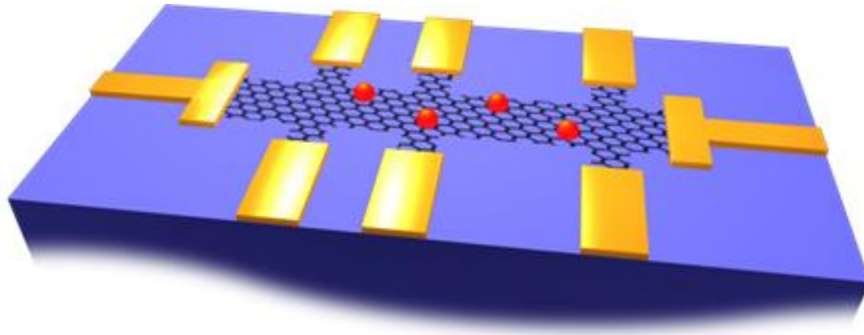

Figure 5- 1: Schematic diagram showing a graphene non-local Hall bar device with junctions of different length with adatom impurities (red solid spheres).

In this chapter, we show that the presence of dilute residual copper (Cu) adatoms on graphene grown by CVD on Cu foil (CVDG)[119,120,160–162] is sufficient to enhance the SOC strength by several orders of magnitude. Our experimental findings based on Raman spectroscopy measurements, X-ray photoelectron spectroscopy (XPS), energy-dispersive X-ray spectroscopy (EDX) and non-local spin transport characterization of the samples together with theoretical modelling demonstrate that physisorbed metallic adatoms form nanometre-size clusters[163] inducing SOC enhancement in graphene up to 20 meV. The large enhancement in SOC allows the generation of spin currents via the SHE[27] with an exceptionally large spin Hall coefficient (angle) γ~0.2. The latter is comparable to what has been observed in gold (Au)[132], platinum (Pt)[164] or tungsten (W)[150] thin films with thickness at least 10 times larger than that of graphene. Here, what differentiates graphene is the strong Fermi-energy dependence of the density of states and its sharp sensitiveness to adsorbed species making it ideal for extrinsically generated SHE[153]. To rule out CVD-specific vacancies, defects and ripples for the observed enhancement in SOC, we performed identical measurements on exfoliated pristine graphene (EPG) samples that are intentionally decorated with adatoms like copper (Cu), gold (Au) and silver (Ag). In both CVDG and EPG samples decorated with

metallic adatoms, we see a similar enhancement of the SOC[165] by three orders of magnitude (up to 20meV) confirming the proximity effect as the dominant factor for the observed SHE.

5.2 DEVICE FABRICATION AND CHARACTERIZATION

5.2.1 DEVICE FABRICATION

Sample preparations (Cu-CVD graphene):

The growth of CVD graphene on Cu foil and the subsequent etching of Cu in ammonium persulphate (7 g dissolved in 1 l of deionized (DI) water) and transfer onto a Si/SiO_2 substrate are performed following the work of Bae et al.[120]. The transferred samples are annealed in Argon/Hydrogen (90:10) environment at 320 °C for 5 h to remove any organic contaminants. Figure 5-2 a) shows the AFM image of a graphene sample decorated with Cu nanoparticles with average particle diameter of ~40 nm and is in good agreement with the recent transmission electron microscopy results[162].

Sample preparations (Exfoliated graphene devices with Cu adatom):

The graphene samples are first exfoliated onto a SiO_2 substrate with Au markers. Using the standard transfer technique for graphene/boron nitride hetero-structures[166], the exfoliated graphene samples together with the Au markers are peeled off with a polymer layer and then transferred onto a Cu foil. The transferred samples are first baked at 120 °C in a hot plate for better adhesion. The sample on Cu foil is then placed in the Cu etchant (ammonium persulphate, 7 g dissolved in 1 l of DI water). The etching process, which is exactly the same as the process performed for CVD graphene[120], introduces Cu particles on graphene. A second way to introduce the Cu adatoms is to dissolve the Cu foil in the Cu etchant (ammonium per

sulphate). This is followed by immersion of the final graphene spin Hall device on SiO_2 into the solution containing dissolved Cu.

Sample preparations (Exfoliated graphene devices with Au/Ag adatoms):

The Au and Ag adatoms are introduced onto the graphene sample by drop casting commercially available Au/Ag colloidal solutions. The Au and Ag nanoparticles are of an average size of ~30 nm. For the experiments shown in this work, we have used the colloidal solutions bought from BBI solutions (Product code: CIKITDIAG (for Au) and ArraySC40 (for Ag)). These solutions are diluted with DI water to get different concentrations of the nanoparticles, that is, 10^{10} particles per ml to 10^{7} particles per ml. For the data shown in this work, the nanoparticle concentration is 10^{8} particles per ml.

The Au particles are also introduced by thermal deposition. Here, the deposition is performed using the lowest deposition rate of 0.01 $Ås^{-1}$ and by opening the substrate shutter for a few seconds. This allows deposition of Au nanoparticles on graphene with an average size of ~25 nm. Figure 5-2 c) shows the AFM image for a graphene spin Hall device with Au adatoms and Table 5-1 shows the average diameter and particle distribution of various adatoms.

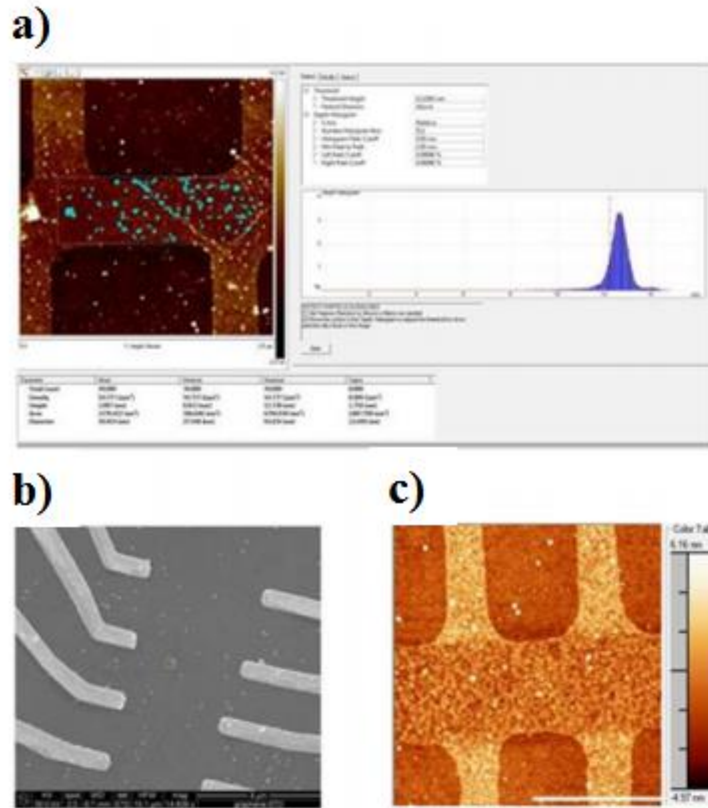

Figure 5- 2: a) AFM scan for Cu-CVD graphene device after annealing at 300 °C, particle analysis show details of distribution of particle sizes on graphene and the average of Cu nanoparticle size in this device is about ~40 nm in diameter. b) SEM and c) AFM scans of graphene device with Au adatoms. Scale bar is 2 μm.

	Average Diameter (nm)	Standard deviation (diameter in nm)	Particle density (cm^{-2})
Cu	40	12.6	0.6×10^{10}
Au	29	8	1.1×10^{10}

Table 5- 1: Adatom distribution for both Cu and Au.

5.2.2 RAMAN CHARACTERIZATION

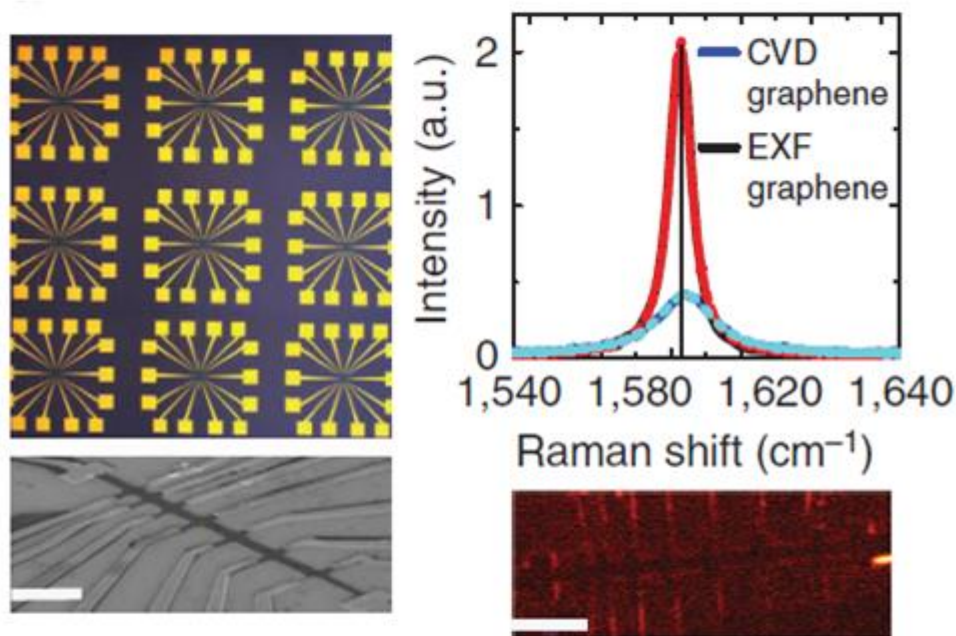

Figure 5- 3: Optical image of a 3 by 3 array of CVD graphene devices on Si/SiO_2 substrate together with Raman and SEM image of the graphene channel in a typical spin Hall device. Scale bar is 5 µm.

Figure 5-3 shows the optical picture of a 3×3 array of CVDG spin Hall devices on a Si/SiO_2 wafer together with the Raman and scanning electron micrograph (SEM) images. We have also obtained additional detailed Raman mapping of both CVD and exfoliated samples (see Figure 5-4).

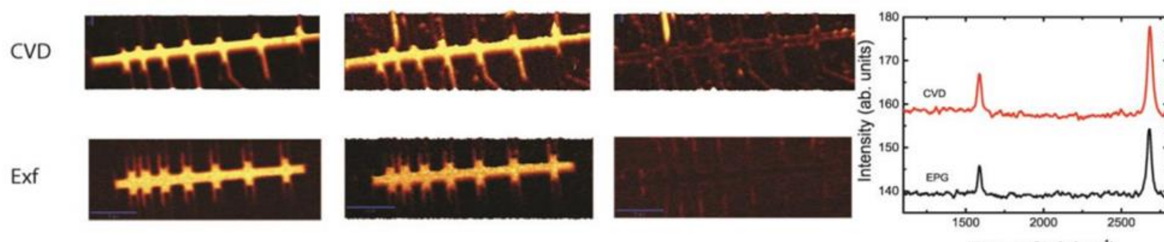

Figure 5- 4: Raman mapping of a CVD graphene device (upper panel) and exfoliated graphene device (lower panel) showing the 2D (2680 cm^{-1}), G (1560 cm^{-1}) and D (1360 cm^{-1}) peak intensities. The prominent relative 2D peak intensity with respect to G peak intensity confirms that the Cu-CVD graphene samples are monolayer. A comparison of the CVD Raman scan

with that of the exfoliated pristine graphene device show negligible D peak for the entire channel of the device and is similar to the Raman mapping of exfoliated graphene device.

5.2.3 EDX AND XPS CHARACTERIZATION

To further confirm the presence of Cu adatoms on our CVDG samples, we have also performed EDX and XPS. Figure 5-5 shows both the measurements data, which clearly shows the presence of Cu peaks, indicating the presence of Cu adatoms in these samples.

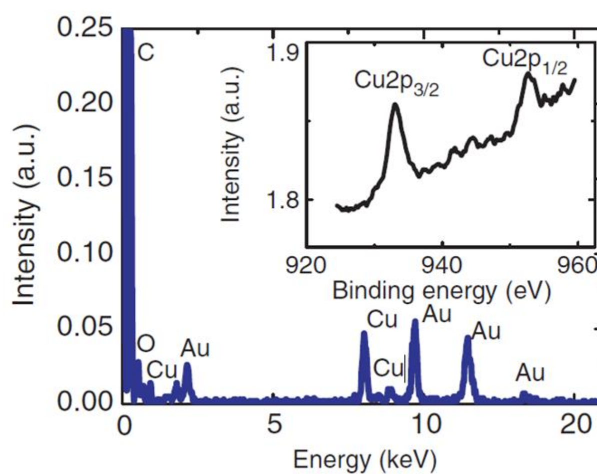

Figure 5- 5: EDX spectrum of CVD graphene sample. The samples for EDX measurements are prepared on a standard transmission electron microscopy (TEM) gold grids and are hence suspended samples. Size of each grid is 7 µm by 7 µm. The additional Au peaks in the EDX spectrum are due to the presence of gold TEM grids. Inset: XPS data on CVD graphene showing Cu 2p peaks.

5.2.4 PRELIMINARY ELECTRICAL CHARGE AND SPIN TRANSPORT CHARACTERIZATION

Charge transport characterization:

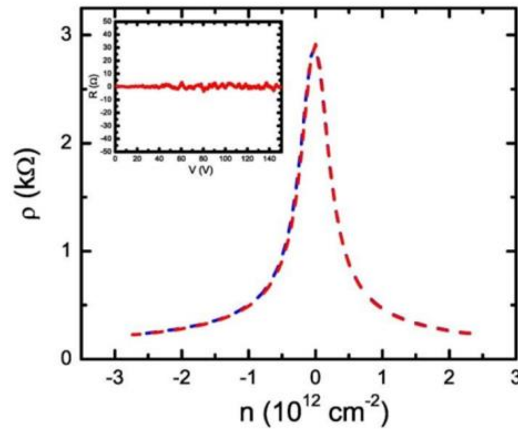

Figure 5- 6: Resistivity versus n for the upper and lower contacts in the H bar geometry. Inset: the low temperature data for the AHE measurement showing the absence of any transverse Hall signal at zero magnetic field.

The devices consists of Hall bar arrays, such that before any spin transport measurements the CVDG devices can be first characterized for charge transport using the local four-terminal geometry with Au/Cr contacts. We first characterize charge transport to ensure homogeneity of the sample by measuring the longitudinal resistivity and only Hall junctions where the opposite pair of contacts shows identical resistivity are selected (see Figure 5-6). Moreover, the absence of any transverse Hall resistivity at zero external magnetic fields confirms the uniformity of the sample[167,168]. The absence of an anomalous Hall signal eliminates the possibility of (ferro) magnetic moments due to the introduction of adatoms.

Spin transport characterization (non-local spin valve):

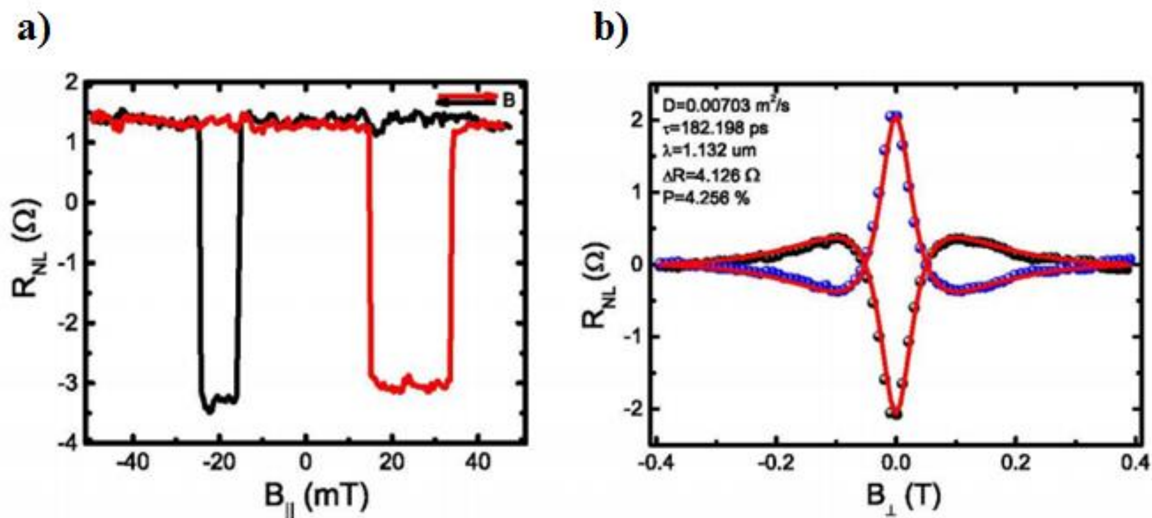

Figure 5- 7: a) Non-local spin valve measurements for in-plane magnetic field. b) Non-local spin valve Hanle precession measurements for Cu-CVD graphene devices for parallel (blue solid circles) and antiparallel (black solid circles) configuration of the injector and detector electrodes. The red lines are the fits to the measured data.

After the charge transport characterization, we performed non-local spin transport measurements via the conventional spin-valve devices prepared in an identical manner, but using ferromagnetic electrodes[31,75,108] and MgO tunnel barriers. Such spin-valve measurements allow the independent extraction of relevant spin parameters like the spin relaxation length (λ_s) and spin relaxation time (τ_s) of CVDG. The CVD spin-valves has the Co (35 nm) /MgO (2 nm)/CVD graphene/MgO (2 nm)/Co (35 nm) structure with a final Au capping layer, 5 nm thick, to prevent oxidation of the Co electrodes. The non-local spin-valve signals for parallel and perpendicular magnetic field sweeps are shown in Figure 5-7. We can fit the Hanle precession curve to obtain key spin parameters by using the relation[75,76]:

$$R_{NL} \propto \int_0^{\infty} \frac{1}{\sqrt{4\pi Dt}} e^{\frac{-L^2}{4Dt}} e^{\frac{-t}{\tau_s}} \cos(\omega_L t)\, dt, \qquad (5.1)$$

where L is the distance between injector and detector D is the diffusion coefficient and ω_L is the Larmor spin precession frequency.

From the fit, we obtained spin relaxation length of 1.3 μm, comparable to the values obtained from independent spin Hall Effect measurements which will be discussed later in the next sub-chapters.

5.3 ELECTRICAL SPIN HALL EFFECT MEASUREMENTS

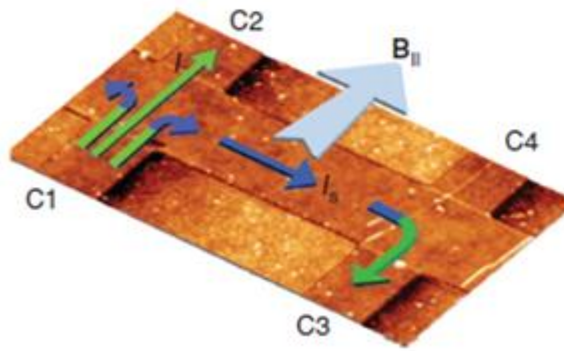

Figure 5- 8: AFM three-dimensional surface topography of a typical spin Hall device with details of actual spin Hall measurements.

Spin Hall Effect characterization:

Finally, we perform the spin Hall measurements employing only Au/Cr contacts in the H-bar geometry[1,92,93] both at room temperature (RT) and at low temperatures. In the H-bar geometry, a charge current (*I*) is driven across the contacts C1/C2 and a non-local voltage (*V*) is detected across contacts C3/C4 (see Figure 5-8). In the presence of a strong spin-orbit coupled potential $V_{SO}(r)$, the scattering cross section $\sigma(\theta)$ for electrons with up (↑) and down (↓) spins is asymmetric, that is, $\sigma^{\uparrow(\downarrow)}(\theta)\neq\sigma^{\uparrow(\downarrow)}(-\theta)$. This in combination with time-reversal symmetry, $\sigma^{\uparrow(\downarrow)}(\theta)=\sigma^{\downarrow(\uparrow)}(-\theta)$, spatially separates the spin components of charge carriers leading to the formation of transverse spin current (I_s)[153,169]. For a narrow channel, such that the spin

relaxation length λ_s is larger than the width W of the channel ($\lambda_s > W$), I_s is nearly constant across W and exponentially decays with length L as[93]:

$$I_s(L) = \frac{I\sigma_{xy}^{sH} W}{2\sigma_{xx}\lambda_s} e^{-L/\lambda_s}, \tag{5.2}$$

where σ_{xx} is the charge conductivity and σ_{xy}^{sH} is the spin Hall conductivity. A transverse charge accumulation is in turn induced by the inverse SHE and is given by the following equations[93]:

$$\delta V = \frac{\sigma_{xy}^{sH}}{\sigma_{xx}^{2}} I_s(L) = \frac{I\gamma^2 \rho W}{2\lambda_s} e^{-\frac{L}{\lambda_s}}, \tag{5.3}$$

$$\gamma = \frac{\sigma_{xy}^{sH}}{\sigma_{xx}}, \tag{5.4}$$

$$\rho = \frac{1}{\sigma_{xx}}. \tag{5.5}$$

Hanle precession measurements, where the non-local signal is measured under an in-plane magnetic field B are also employed to unambiguously confirm that the non-local signal is indeed due to spins[93]. For this experiment, multiple samples were measured for each type of adatoms discussed in this chapter.

Back gate voltage dependence of non-local signal:

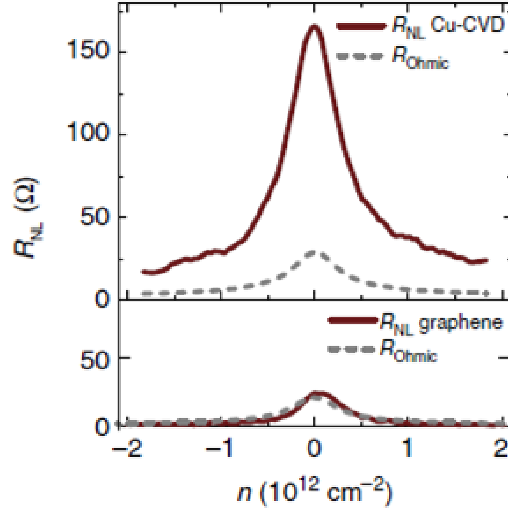

Figure 5- 9: Non-local signal versus n for pristine graphene sample (lower panel) and Cu-CVD graphene (upper panel). L/W=2 for both devices. The grey dashed line represents the ohmic contribution in these devices.

In Figure 5-9, we compare the non-local signals (R_{NL}) as a function of the charge carrier density n at room temperature, for EPG and CVDG with identical length to width ratio L/W=2 and comparable mobilities (~5,000 $cm^2V^{-1}s^{-1}$). We observe an exceptionally high R_{NL}~160 Ω for CVDG. On the other hand, in exfoliated graphene, the measured signal is almost identical from the expected ohmic leakage (~20 Ω). The latter is given by[92,93]:

$$R_{Ohmic} = \rho e^{\frac{-\pi L}{W}}. \tag{5.6}$$

Thermo-magneto electric effects, can be present in an externally applied perpendicular magnetic field[170]. As discussed in this work, the measured non-local signal could have significant contributions from thermo-magneto-electric effects. However, these contributions play an important role only in the presence of a perpendicular magnetic field. In the absence of an external field in the length and width dependence measurements and in the presence of in-plane field in the spin precession measurements, the only thermal effect which could contribute

to the non-local signal is the Joule heating. Since in Joule heating, the measured signal is proportional to the square of the source drain current, studying the I-V characteristics of the non-local device should provide the clear evidence, if any. Figure 5-10 shows the I-V curve for a Cu-CVD graphene device. The linear I-V clearly demonstrates that the contributions from Joule heating, if any, to the measured non-local signal is negligible.

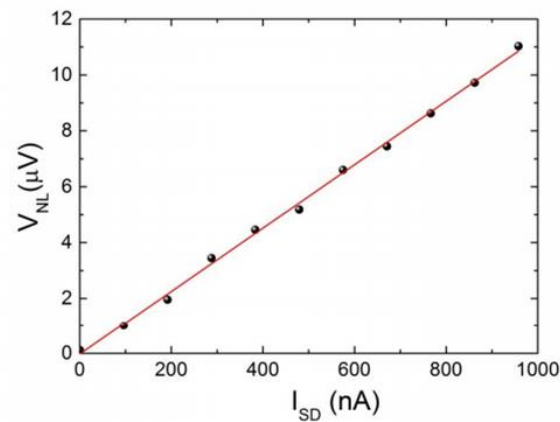

Figure 5- 10: Measured non-local signal (voltage) as a function of source drain current.

Thus, we are left with only the SHE that can give rise to such a large non-local signal at zero magnetic fields. This, however, requires a significant SOC strength and hence points to a strongly enhanced SOC in CVDG when compared with EPG.

Length and width dependence of non-local signal:

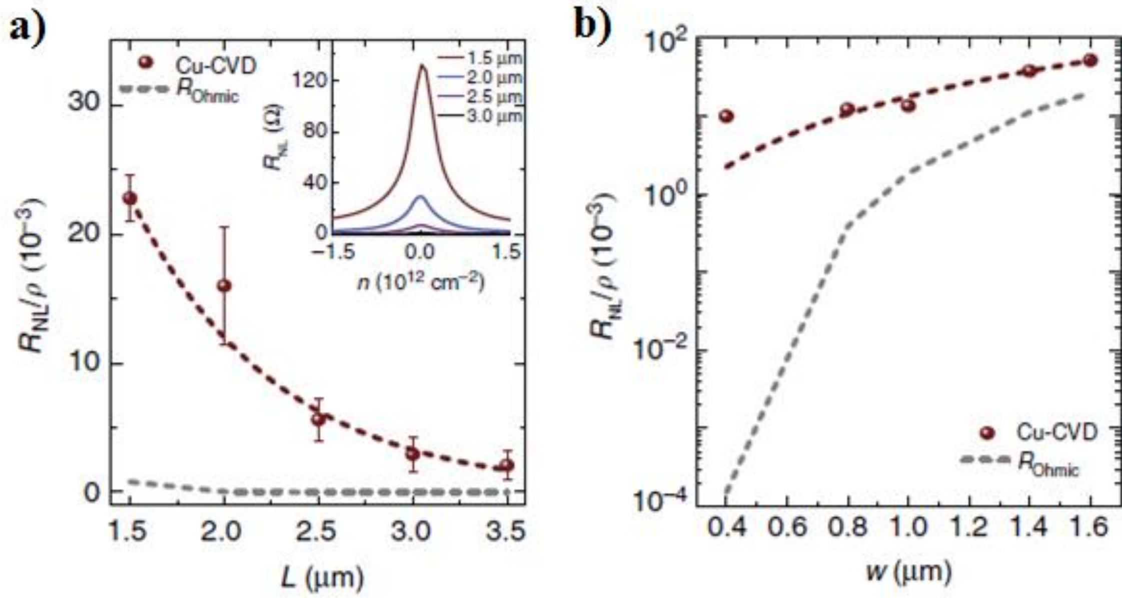

Figure 5- 11: R_{NL}/ρ versus length for CVD graphene with width W=500 nm. The plotted data are average values for three different samples and the error bar corresponds to the standard deviation from the mean value. Inset: Non-local signal for different L/W ratio of the channel.

To extract the spin parameters from the measured non-local signal, we next study the dependence of R_{NL} on the device geometry. The dependence of the non-local signal on the length and width can be obtained by solving the diffusion equation for the spins and is given by[93,138,171]:

$$R_{NL} = \frac{1}{2}\gamma^2\rho\frac{W}{\lambda_s}e^{\frac{-L}{\lambda_s}} = \frac{1}{2}\gamma^2\rho\frac{W^2}{\lambda_{SO}{}^2}e^{\frac{-LW}{\lambda_{SO}{}^2}} . \tag{5.7}$$

Here, λ_s is the spin relaxation length and is related to the spin precession length λ_{SO}, defined as the length scale for a complete spin precession cycle in a clean system, by $\lambda_s(W) = \frac{\lambda_{SO}{}^2}{W}$ as discussed in previous chapter. The dimensional dependence of R_{NL}, thus, allows two independent experiments: 1) the length and 2) the width dependence of the non-local signal, to extract the critical spin parameters like λ_s and spin Hall angle (γ). First, for a constant width W, the equation gives a R_{NL} which decays exponentially with the length L. Secondly, where the width of the sample is varied, we chose devices with narrow width such that the condition λ_s,

$\lambda_{SO}>W$ is assured. The length and width dependence equation for R_{NL}, can be simplified by expanding the exponential term as:

$$R_{NL} = \frac{1}{2}\gamma^2\rho\frac{W^2}{\lambda_{SO}{}^2}\left[1 - \frac{LW}{\lambda_{SO}{}^2} + \cdots\right]. \tag{5.8}$$

This results in the non-local signal R_{NL} to have a power law dependence on W. Here, we first discuss the length dependence of R_{NL} (Figure 5-11 a)) by fixing W=500 nm and varying length L from 1.5 μm to 4 μm. As expected, the non-local signal decays exponentially with L and the fit with the equation gives a λ_s~0.8 μm and a γ~0.2.

We next study the width dependence of R_{NL} by fixing L=2 μm. Figure 5-11 b) shows R_{NL} versus W for a device with L=2 μm at the CNP and at room temperature. In addition, we have also performed width dependence non-local signal for different carrier densities (see Figure 5-12).

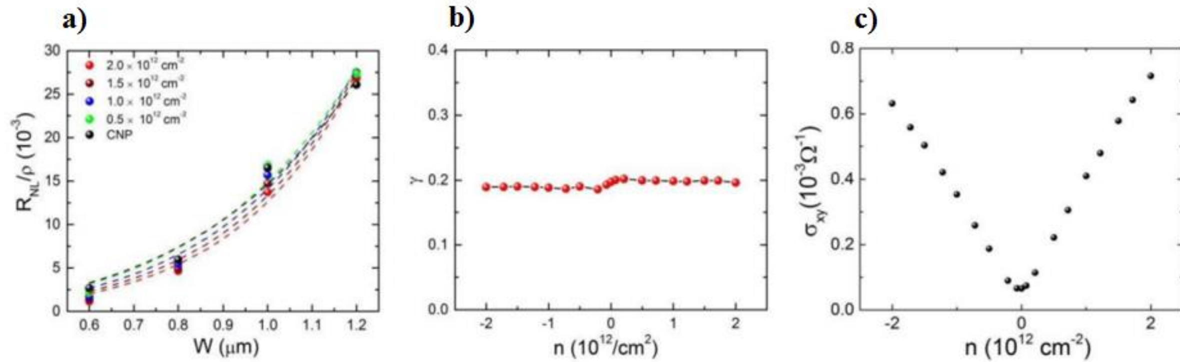

Figure 5- 12: a) Width dependence of the non-local signal for different carrier densities. b) The carrier density dependence of the extracted spin Hall angle. c) Spin Hall conductivity for the same sample.

In general, the spin Hall conductivity is determined from the spin Hall coefficient as $\sigma_{xy}^{sH} = \gamma\sigma_{xx}$. We take the same convention to calculate the spin Hall conductivity for our samples as shown in Figure 5-12 c). The observed power law behavior in our devices again confirms the spin nature of the R_{NL}. It is worthy to note that the difference between ohmic and measured non-local signals is more distinct in junctions with smaller width, in agreement with

predictions for narrow channels, that is, λ_s, $\lambda_{SO} > W$[93,138]. Furthermore, the values for λs~2 μm and γ~0.18, obtained from the width dependence, are in good agreement with values extracted from the length dependence.

In-plane magnetic field dependence of non-local signal:

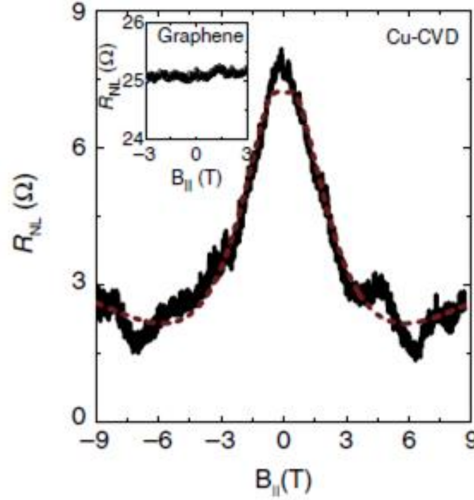

Figure 5- 13: The in-plane magnetic field dependence of the non-local signal for Cu-CVD graphene samples. The dotted line is the fit for the data. Inset: magnetic field dependence of pristine exfoliated graphene sample.

For a last and clear confirmation of the spin characteristics of R_{NL}, we also study the Hanle effect in our devices. Spin Hall Effect alone would result in an oscillatory signal due to the precession of spins in an in-plane field B[93]. Figure 5-13 compares the R_{NL} versus B for a CVDG sample with that of a representative EPG sample (inset). The sample dimensions in both devices are identical and their charge mobilities comparable. As expected, only the CVDG samples show a non-monotonic oscillatory dependence of the non-local signal, within the diffusive regime, and can be fitted with the following magnetic field dependence equation[93]:

$$R_{NL} = \frac{1}{2}\gamma^2 \rho W Re\left[\left(\frac{\sqrt{1+i\omega_B \tau_s}}{\lambda_s}\right) e^{-\left(\frac{\sqrt{1+i\omega_B \tau_s}}{\lambda_s}\right)|L|}\right], \tag{5.9}$$

where $\omega_B = \Gamma B$ is the Larmor spin precession frequency, Γ is the electron gyromagnetic ratio and B is the applied in-plane magnetic field. The fitting of the Hanle precession results in λs~2 μm and γ~0.17, again comparable to previous independent studies.

Control experiments:

The non-local length, width and Hanle precession measurements all confirm the spin origin of the R_{NL} and give comparable values for both λ_s and γ. These spin parameters are consistent with the values obtained from both independent conventional non-local spin-valve measurements[76] and spin pumping measurements published elsewhere[172]. It is noteworthy that the distinct configurations of the spin Hall and spin-valve experiments result in spin precession R_{NL} curves with very different magnetic field scales (see Figure 5-13 and Figure 5-7). The contrast of the oscillations shows that in the spin Hall configuration, the magnetic field range required to suppress R_{NL} to half its value at zero field is an order of magnitude larger than in the spin-valve configuration. This discrepancy between the non-local spin Hall and spin-valve magnetic field scales is a direct consequence of the distinct geometries involved.

In the spin-valve configuration the magnetic field range to observe oscillations is roughly determined by the condition: $\omega_L\tau_s$~1. Here, ω_L is the Larmor frequency and τ_s denotes the spin relaxation time (in Cu-CVDG representative sample this is τ_s~0.1 ns). With this condition it yields B(perpendicular)~50 mT, in excellent agreement with the data shown in Figure 5-7. Meanwhile, the onset of oscillations in the spin Hall configuration is found by setting the magnetic field dependence equation of non-local signal to zero, that is:

$$Re\left[\left(\frac{\sqrt{1+i\omega_B\tau_S}}{\lambda_S}\right)e^{-\left(\frac{\sqrt{1+i\omega_B\tau_S}}{\lambda_S}\right)|L|}\right] \approx 0. \tag{5.10}$$

The value of $\omega_L\tau_s$ in order to solve this depends strongly on L/λ_s (for example, taking L/λ_s=1(0.5) gives $\omega_L\tau_s$~12(45)). In our devices the ratio L/λ_s is very close to the unity and hence the onset for oscillations in the spin Hall setup as defined by the minimum field suppressing the signal is given by B~0.5 T (in this case, the applied magnetic field is in-plane), which is ten

times larger than the spin-valve setup. This agrees qualitatively well with the non-local data for Cu-CVDG [see Figure 5-13]. The difference between the magnetic field scales in the non-local spin Hall and spin-valve experiments is thus explained by their different configurations. We note that similar conclusions were obtained by Shchelushkin et al.[173] for spin precession in aluminum.

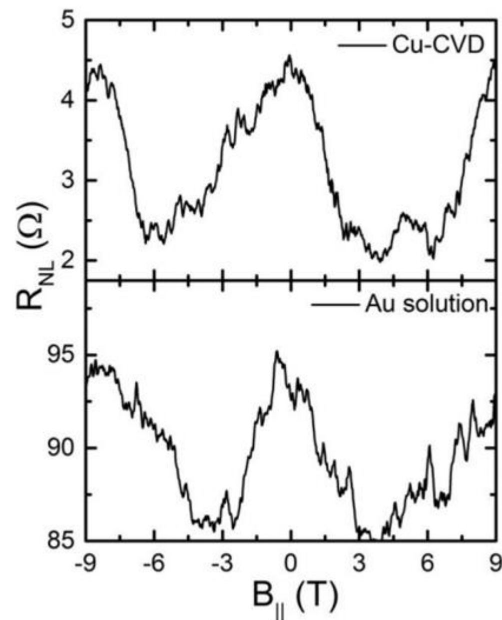

Figure 5- 14: Non-local spin Hall precession measurements showing un-damped oscillatory behavior.

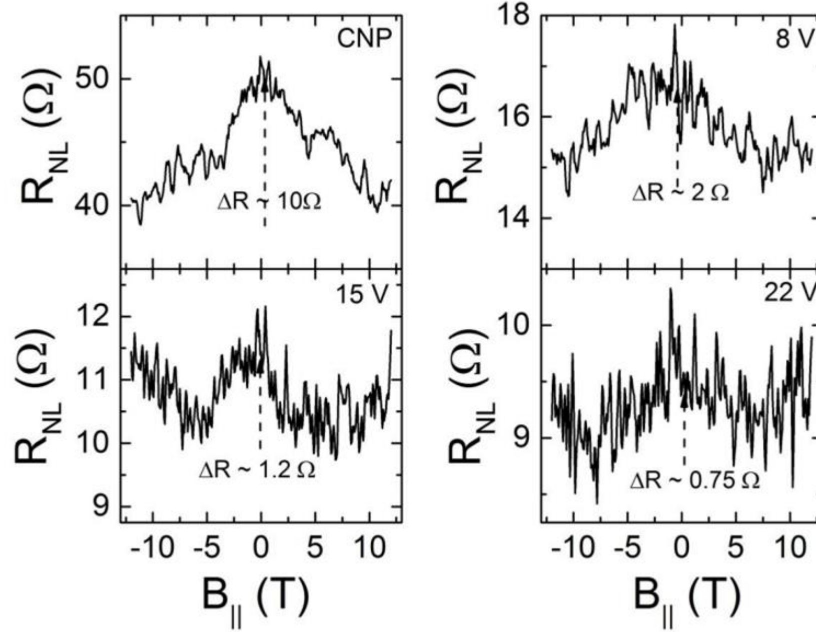

Figure 5- 15: Additional in-plane magnetic field dependence data of non-local signal at different back gate voltages for device decorated with Au adatoms.

In a diffusive system, spin precession measurements show a damped oscillatory behavior as the magnetic field is varied. However, some of our samples show a perfect oscillatory behavior (see Figure 5-14); such an un-damped precession signal has been observed in Si spin-valves in the ballistic regime by Appelbaum et al.[174]. In our case, calculations based on the transport data indicate an electron mean free path of the order of ~ 200 nm, much smaller than the device dimensions (~1 μm), ruling out ballistic propagation as an explanation. Residual background magneto-resistance could be the reason for the persistent oscillatory behavior seen in some of our decorations. The clear understanding of this effect would require experimental analysis much beyond the scope of the present work.

Furthermore, since we do not observe SHE in EPG, the origin of the SHE in CVDG must have an extrinsic origin. In principle, it can be due to a wide range of CVD-specific defects such as wrinkles, grain boundaries, ripples, vacancies, organic residues coming from

the Cu etching solution or the residual Cu adatoms[162]. We can immediately rule out structural defects as the main contributor to the observed R_{NL} since Raman mapping shows negligible D-peak for the entire device and is similar to the Raman mapping of our EPG devices. We further rule out organic residues as the dominant source by immersing identically prepared exfoliated graphene samples in the same Cu etching solution (ammonium persulphate). In such devices, the measured R_{NL} are much smaller than in CVDG and remain comparable to the expected ohmic contribution.

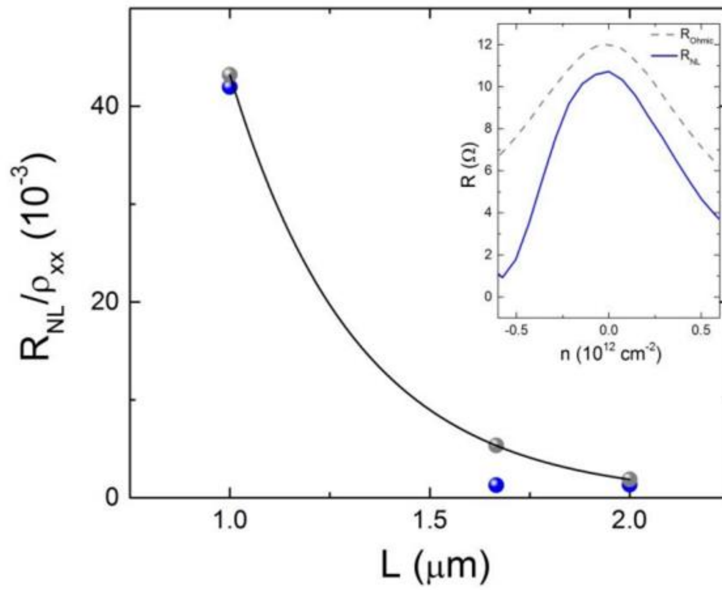

Figure 5- 16: Length dependence of the non-local signal for exfoliated graphene samples immersed in the etchant solution of ammonium persulphate. The width of the sample is W=500 nm. The measured non-local signal is comparable to the calculated ohmic contribution. Inset: non-local signal versus n for junction with dimensions L/W=2.

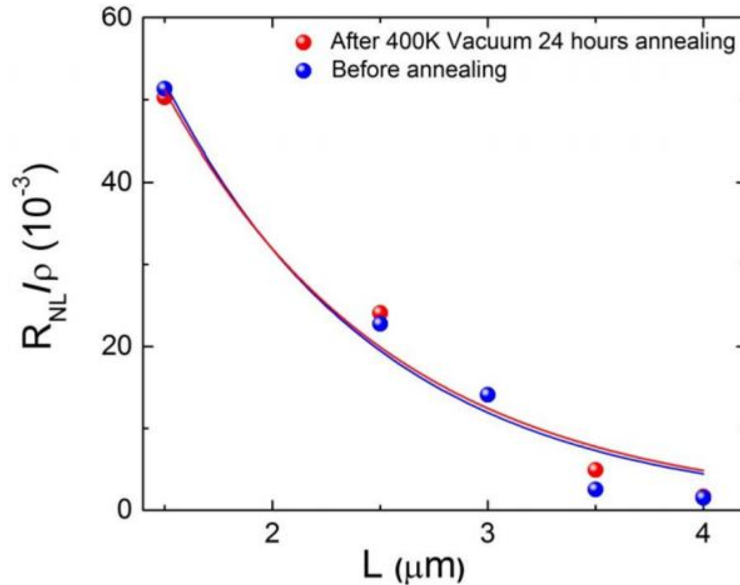

Figure 5- 17: Length dependence of the non-local signal for Cu-CVD graphene sample before and after vacuum annealing at 400 K for 24 hours.

Graphene immersed in ammonium persulphate solution:

In order to confirm that the organic residues introduced by the Cu etching solution (ammonium persulphate) on the graphene is not the cause for the observed non-local signal, we performed identical experiments on exfoliated graphene samples immersed in the etchant solution. Figure 5-16 shows the dependence of the non-local signal on the carrier density n and the length *L* of the device. The width of the sample is fixed at *W*= 500 nm. Here, similar to pristine exfoliated graphene, the measured non-local signal is comparable to the ohmic contribution, thus confirming that the organic residues do not have any significant contribution to the measured non-local signal.

Eliminating hydrogen as the origin of the measured non-local signal:

Since the growth of CVD graphene involves hydrogen environment, the possibility of the hydrogen getting bonded with the carbon atoms cannot be neglected. One way to identify the presence of hydrogen is to inspect the Raman D peak. As shown under Raman

characterization, in our CVD graphene samples the Raman D peak is prominent only at the sample edges, which can be assigned to the uneven edges of the sample due to oxygen plasma etching. However, to make sure that the contribution from any remnant hydrogen is not present to the non-local signals, we vacuum annealed the sample at 400 K (limited by the maximum temperature set point of our probe) for 24 hours. Our results, Figure 5-17, shows very little effect of annealing on the measured signal and the non-local signal before and after annealing remains the same, thus eliminating hydrogen as the possible cause for the measured non-local signal.

This suggests that residual Cu adatoms are the main cause for the large increase of R_{NL}. While the density and cluster size of Cu adatoms strongly depends on the details of the etching and transfer process for CVD graphene, they are generally speaking unavoidable. This has recently also been directly confirmed by transmission electron microscopy measurements[162]. Indeed, detailed XPS and EDX measurements of our own CVDG samples confirm (see sub-chapter on EDX and XPS characterization) the presence of Cu. For the samples discussed here, atomic force microscopy (AFM) measurements show Cu adatom clustering with an average size of ~20 nm in radius and particle density of 0.6×10^{10} cm^{-2} (see sub-chapter Device fabrication). Note also, that here and unlike in our previous hydrogenated work[1], a comparison of the Raman G-peak position in CVDG with that in EPG rules out bond-angle deformation as a potential cause for the SOC enhancement[175]: while in hydrogenated graphene the Raman G-peak shows a shift of ~10 cm^{-1} in wavenumber[175], a negligible G-peak shift in our CVDG demonstrates the physisorbed nature of the Cu adatoms.

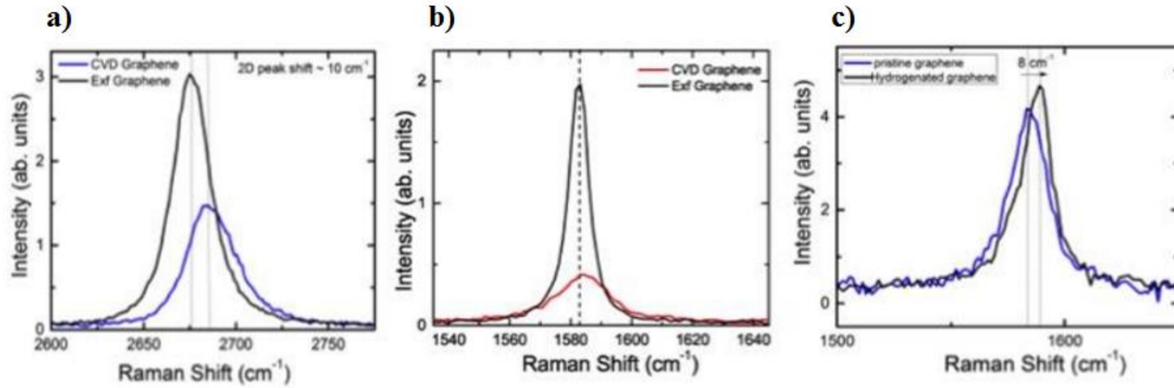

Figure 5- 18: a) Comparison of Raman 2D peak for Cu-CVD and exfoliated graphene samples. b) Comparison of Raman G peak for Cu-CVD and exfoliated graphene samples. c) Raman G peak shift for hydrogenated graphene sample showing the chemisorbed nature of the adsorption.

As discussed earlier, both XPS and EDX data clearly show the presence of Cu adatoms in CVD graphene. An idea of how the Cu adatoms are adsorbed on to the graphene lattice can be understood by analyzing the Raman data carefully. Figure 5-18 shows the comparison of the Raman 2D and G peak position for pristine exfoliated graphene samples and Cu-CVD graphene samples. With respect to the pristine exfoliated graphene samples, the Raman 2D peak for Cu-CVD graphene shows a blue shift of ~ 10 cm^{-1} in wavenumber while the G peak shows negligible shift. The blue shift of 10 cm^{-1} in 2D peak indicates a strain of 0.3 % and the relatively small G-peak shift validates the physisorbed nature of the Cu-adatoms[175]. If the adatoms were chemisorbed, i.e. forms chemical bonding with the carbon atoms like in hydrogenation, the G-peak position shows a large shift of ~ 10 cm^{-1}. Figure 5-18 c) shows the G-peak shift in weakly hydrogenated (~0.01 %) graphene sample when compared with the pristine exfoliated samples.

All this strongly suggests proximity-induced enhancement of the SOC. However to unambiguously establish that physisorbed Cu adatoms are the dominant cause for the observed SHE, we exfoliate graphene onto a Cu foil and repeat the same etching and transfer process

used for CVD graphene (see sub-chapter on Device fabrication). Lastly, we also perform similar measurements on EPG samples decorated with Ag and Au by both solution process and thermal evaporation (see sub-chapter on Device fabrication).

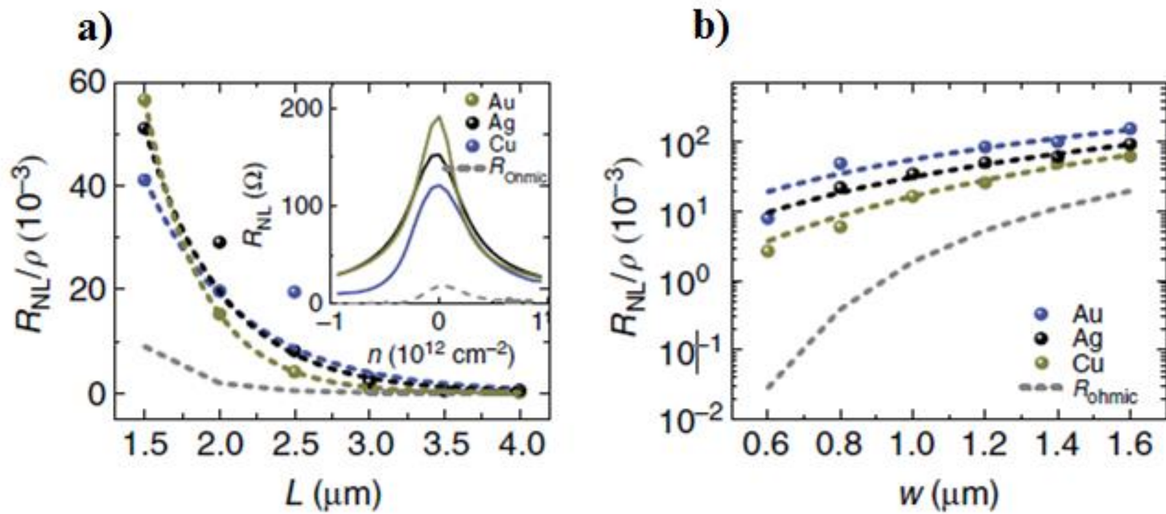

Figure 5- 19: a) and b) Length and width dependence of the non-local signal for exfoliated graphene samples decorated with Cu, Au and Ag adatoms. The grey dotted line shows the measured non-local signal (which is equal to the ohmic contribution) for a pristine graphene sample. Inset of a): non-local signal versus n.

Figure 5-19 summarizes the length and width dependence of the non-local signal for all three types of metal decoration. In all such samples, we do observe a R_{NL} comparable to the one observed for CVDG samples. The fits give comparable spin relaxation lengths and spin Hall angle (see Table 5-2).

Graphene decorated with metallic adatoms.			
Sample	Mobility (cm^{2}V^{-1}s^{-1})	λ_s (μm)	γ
Cu-CVD	11,000	1.9	0.17
Cu-EPG	9,000	1.1	0.27
Au-EPG	15,000	2.0	0.15

Table 5- 2: Sample characteristics for graphene devices decorated with metallic adatoms.

In contrast to EPG dipped in etching solution only, EPG samples that have been intentionally decorated with metallic adatoms show again an oscillatory behavior when an in-plane magnetic field is applied (see Figure 5-20). This unambiguously confirms the spin origin of the non-local signal also in these samples.

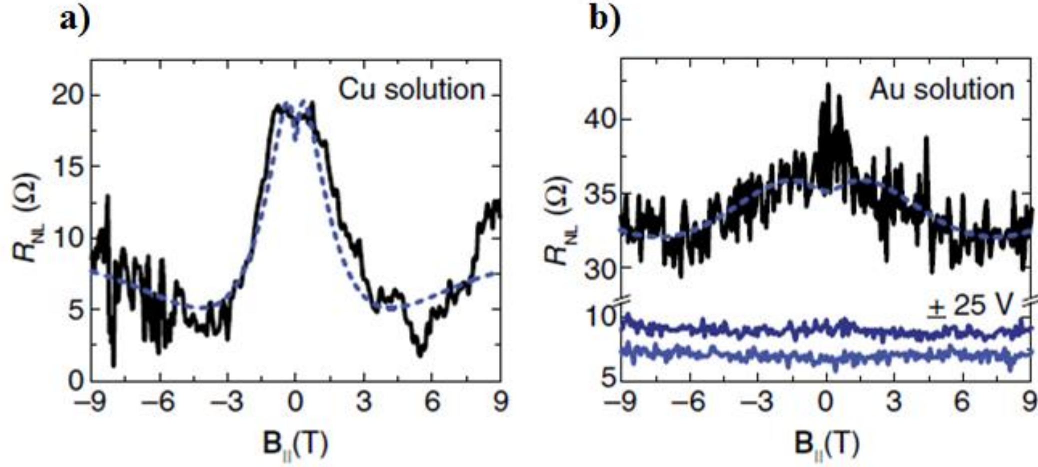

Figure 5- 20: a) In-plane magnetic field dependence precession measurements for exfoliated graphene device with Cu adatoms. b) For exfoliated graphene device with Au adatoms. The blue dashed lines are fit to the experimental data. L/W=3 for all samples with comparable mobility ~10,000 cm^{2}V^{-1}s^{-1}.

5.4 SPIN ORBIT COUPLING STRENGTH

We are now ready to estimate the SOC (Δ) in CVDG and EPG decorated with metallic adatoms. In graphene, both Elliott–Yafet (EY) and D’yakonov–Perel (DP) spin relaxation mechanisms are present. The total spin scattering rate is the sum of the individual scattering rates, that is:

$$\frac{1}{\tau_s} = \frac{1}{\tau_s^{EY}} + \frac{1}{\tau_s^{DP}} , \tag{5.11}$$

$$\tau_s^{EY} = \frac{a^2 \varepsilon_F^2}{\Delta_{EY}^2} \tau_p , \tag{5.12}$$

$$\frac{1}{\tau_s^{DP}} = \frac{4\Delta_{DP}^2}{\hbar^2}\tau_p \,, \qquad (5.13)$$

where τ_s^{EY} and τ_s^{DP} are the spin relaxation times due to Elliot-Yafet and D'yakonov-Perel respectively.

Here, a=2 for intrinsic-like SOC and a=1 for Rashba type SOC[101]. The interpretation of the experimental spin Hall angle using a semi-classical model for the adatom clusters suggests that the predominant contribution to the SOC enhancement comes from intrinsic-like spin–orbit interaction and thus we set a=2 hereafter[1,36,139,153,157].

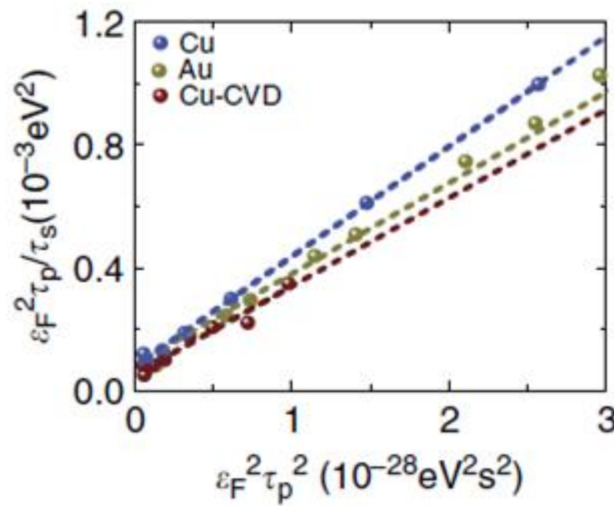

Figure 5- 21: The Fermi energy dependence of the spin relaxation time for various adatoms.

Following Zomer et al.[102], we plot $\varepsilon_F^2\tau_p/\tau_s$ versus $\varepsilon_F^2\tau_p^2$ (see Figure 5-21). From the slope and the y intercept, the SOC strength contribution from both the EY and DP spin relaxation can be estimated. Our data suggest that for all metallic adatoms, the contribution from EY spin scattering dominates over DP. The estimated Δ is only weakly dependent on the atomic number Z and falls in the range of 15±2.3 meV for CVDG and EPG decorated with Cu adatoms and 18±2 meV for EPG decorated with Au adatoms. Note that similar to metallic thin films such a weak dependence of Z is expected[176].

Finally, we discuss how metallic adatoms lead to a robust SHE with such a large γ. A large γ in pure metals such as Pt (0.01-0.1) has been ascribed to resonant scattering on impurity

states split by the spin–orbit interaction[123,132]. The importance of such resonant scatterers in graphene is also well established[153,177]. The extrinsic SHE originates in asymmetric scattering in the presence of SOC: charge carriers of opposite spins are deflected in opposite directions transverse to the applied electric field. Two extrinsic mechanisms produce SHE: skew scattering (SS) and quantum-side jump (QSJ)[71]. The former arises from asymmetry of cross sections in up/down spin channels. On the other hand, QSJ produces anomalous spin currents via spin-dependent shift (side jump) of wave packets in materials endowed with momentum–space Berry curvature. Although the latter is negligible in pristine graphene (due to very weak SOC), nontrivial Berry phase-related effects emerge in adatom-doped graphene via proximity-induced effect. In the SS (QSJ) scenario, the magnitude of induced spin currents is proportional to n_{SO}^{-1} (n_{SO})[71], where n_{SO} denotes the density of SOC active adatoms. Since all samples measured are relatively clean (that is, small n_{SO}) we expect SS to be critical. To identify the SHE mechanism, we carried out realistic transport calculations taking into account adatoms originating the observed SOC enhancement and uncontrolled sources of disorder diminishing the delivered spin Hall angle (see Figure 5-22 and Figure 5-23).

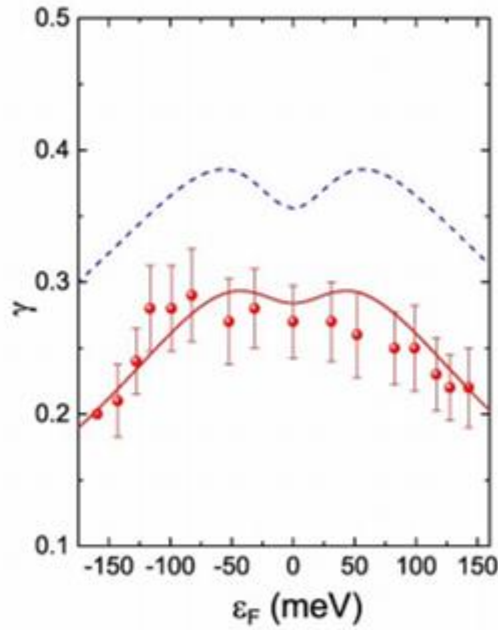

Figure 5- 22: Room temperature data for the Cu-CVD graphene sample. The (dashed) blue line is the ideal spin Hall angle as generated by SOC active dilute Cu clusters in otherwise perfect graphene. The (solid) orange line shows the realistic spin Hall coefficient taking into account other sources of disorder (modelled here as resonant scatterers). Calculations in this plot were performed at room temperature and neglecting the effect of quantum side jump.

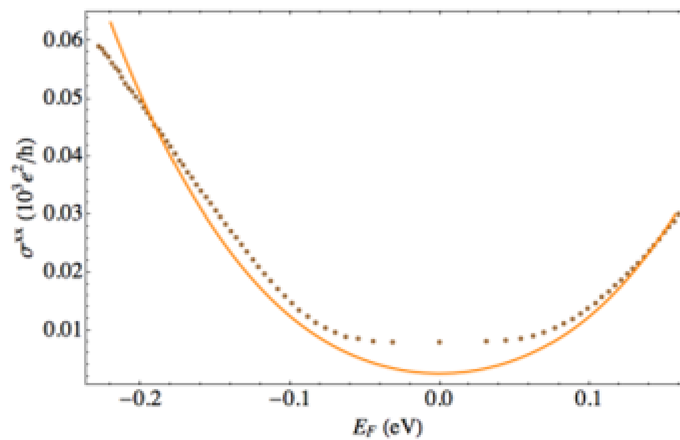

Figure 5- 23: The Fermi energy dependence of the longitudinal (charge) conductivity at room temperature for the Cu-CVD graphene sample. The (solid) orange line shows the theoretical

value of the conductivity. The excellent qualitative agreement shows that fit parameters are consistent with charge transport characteristics of the system.

Our results confirm the dominance of SS mechanism in the experiments and show that the γ for CVDG in and around the neutrality point ($\pm 1\times10^{12}$ cm^{-2}) remains almost a constant, due to the wide distribution of adatom cluster sizes (see Figure 5-24). This is significant in applications for it allows the generation of robust spin currents irrespective of the initial doping level in graphene. The combination of enhanced SOC and the resonant character of large Cu clusters (R~20 nm) make the SS mechanism extremely efficient in the production of spin currents with giant γ in the range 0.1–0.3. With respect to the absence of a strong Z dependence, it is important to note that a large SOC at the impurity site is not the only criteria that can give rise to a large SHE. A strong perturbation of the potential at the impurity site can become equally important[176]. Indeed, in both CVD and EPG, the perturbation of the potential due to the presence of metallic adatom clusters is large and thus is likely the dominant mechanism.

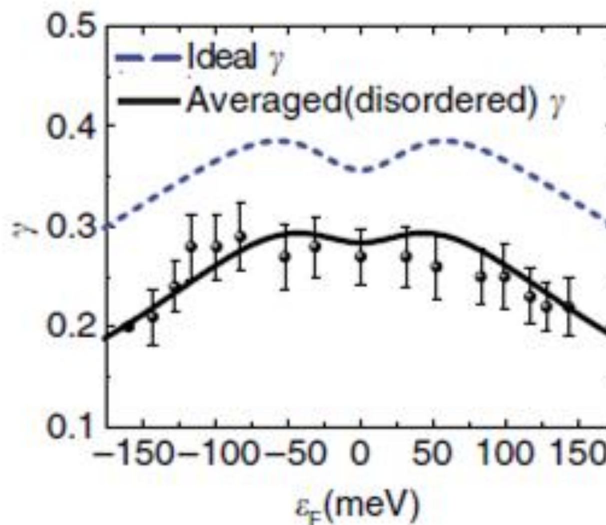

Figure 5- 24: The Fermi-energy dependence of the spin Hall coefficient for Cu-CVD graphene extracted from the length dependence data and theoretically calculated Fermi-energy dependence of spin Hall coefficient in the resonant scattering regime taking into account Cu

adatoms and other impurities limiting charge transport. The data points are from fitting the length dependence at the specified Fermi energy and the error bar corresponds to the standard deviation for spin Hall coefficient obtained from the fitting.

In conclusion, we have shown that the Cu-CVD graphene has a SOC three orders of magnitude larger than that of pristine exfoliated graphene samples. The enhancement in the SOC in Cu-CVD graphene is due to the presence of residual Cu adatoms introduced during the growth and transfer process. We confirm this by introducing Cu adatoms to exfoliated graphene samples and extract a SOC value comparable to the one in Cu-CVD graphene ~15 meV. In addition to Cu, we also show that adatoms like Au and Ag can also be used to induce such enhancement of SOC in pristine graphene. An enhancement of graphene's SOC is key to achieving a robust 2D TI state in graphene. Crucially, SEM/AFM shows that in our decorations adatoms form sizeable clusters (~20 nm size), and thus severe issues associated with inter-valley scattering from isolated adatoms such as the suppression of SHE[157] and topologically protected edge states[36,152] can be largely avoided in the present scheme. Also, the observation of a robust SHE with exceptionally large γ~0.2 at room temperature is a first but important step towards introducing graphene for spin-based concepts such as spin transfer torque based magnetic memory and spin logic applications[150]. Since the effect is equally strong with commonly used non-magnetic metals such as Cu, these applications would be also compatible with existing CMOS technology.

CHAPTER 6 COLOSSAL THERMOELECTRIC RESPONSE IN FEW-LAYER BLACK PHOSPHORUS

With the initial objective of studying spin transport in black phosphorus failed, we have attempted to optimize the contact resistance and improve the surface preparation in this system. In the process we have unexpectedly uncovered black phosphorus' potential as a thermoelectric material. I will present the detailed work on thermoelectric that we have submitted in this chapter and spintronics studies in black phosphorus will be described briefly in the summary and future work later on.

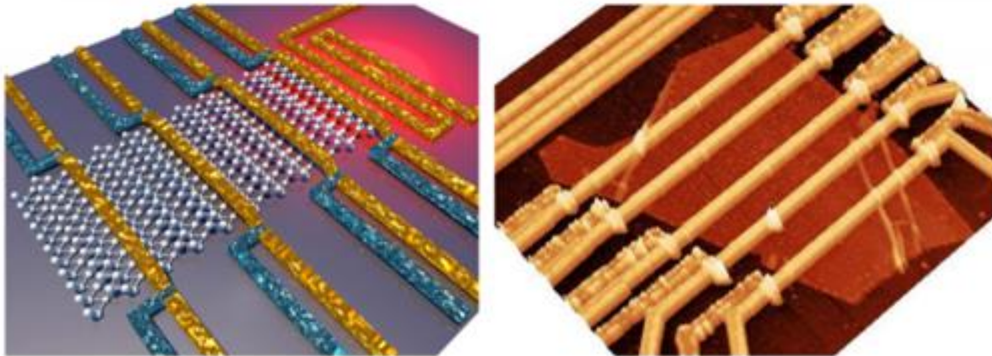

Figure 6- 1: Architecture of a mesoscopic few-layer phosphorene thermoelectric device. Schematic of a single layer phosphorene device. A snake shaped micro-fabricated resistor is used to create a thermal gradient (red) via Joule heating. Metal Au electrodes (yellow) serve as electrical contacts to the phosphorene channel, and as resistive thermometers when measured in a four-terminal configuration. NiCu electrodes (blue) are used to make the 4-terminal connection to the Au electrodes, and also as alternative NiCu/Au thermocouple thermometers. Atomic force microscopy image of a few-layer phosphorene device showing the same architecture.

There is a current drive to explore new two-dimensional atomic crystals[140,178,179] in the search for new physics and potential applications. A material that has recently attracted strong interest is black phosphorus and its single layer, phosphorene. Few-layer black phosphorus[60,67–69,118] is unique among its two-dimensional counterparts because it is a narrow gap semiconductor that retains a direct bandgap all the way down to single-layer thickness[60], giving it excellent prospects for electronics and optoelectronics. Thermoelectric research has only recently started to be explored in two-dimensional atomic crystals[112,180–183]. Motivated by recent theoretical predictions[47] here we study experimentally the thermoelectric response of few-layer black phosphorus and explore the physical mechanism responsible for the observed colossal response.

The most basic thermoelectric property is the thermopower[111] $S = -\Delta V/\Delta T$, also called thermoelectric power or Seebeck coefficient, that describes the generation of an electrical voltage ΔV due to a thermal bias ΔT. The sign of the thermopower usually reflects the polarity of the charge carrier, with $S > 0$ for holes and $S < 0$ for electrons. Additionally, the energy conversion efficiency of a thermoelectric material is quantified by the figure of merit $ZT= S^2\sigma T/\kappa$, with σ and κ the electrical and thermal conductivities, respectively. To study the thermoelectric response in mesoscopic black phosphorus we use a device architecture that combines a field-effect transistor (FET) with thermoelectric circuitry (see Figure 6-1) first developed for carbon nanotubes[180,183–185]. We also expand on this architecture by demonstrating nanoscale thermocouples that are able to map the temperature along the two-dimensional channel with increased resolution[186].

6.1 BLACK PHOSPHORUS BASED THERMOELECTRIC DEVICES

Thermoelectric deals with the interactions between heat and charge transport in solid state systems[111,187] and is a powerful approach to explore transport phenomena in nanoscale materials[188]. In this work we demonstrate that few-layer black phosphorus, a recent addition to the family of two-dimensional crystals[140,178,179], exhibits a colossal thermoelectric Seebeck coefficient up to 150 mV/K at room temperature. We attribute the exceptionally large value to electron-phonon drag, a physical mechanism not considered as yet. Together with a large electrical conductivity[60,67–69,118] and thermal resistivity[189] this gives rise to a figure of merit up to ZT~2.1, a remarkable thermoelectric efficiency for an elemental semiconductor.

6.2 DEVICE FABRICATION AND CHARACTERIZATION

6.2.1 DEVICE FABRICATION AND RAMAN CHARACTERIZATION

Sample preparation:

Few-layer black phosphorus was mechanically exfoliated from its bulk form onto highly p-doped Si substrates covered with a 300 nm thick thermal SiO_2 layer acting as gate dielectric, while the Si substrate acted as an electrostatic backgate electrode. Bulk black phosphorus crystals were purchased from Smart Elements. Prior to the exfoliation, the silicon wafers were treated with O_2 plasma to clean and activate the substrate surface for a higher exfoliation yield. Next, optical micrographs were used to locate the few-layer black phosphorus crystals for device fabrication. Immediately after, we spin coated poly(methyl methacrylate) PMMA electron beam resist to protect the crystals from further degradation in ambient conditions[68,118].

Electron beam lithography (EBL) on the PMMA resist, deposition by thermal evaporation, and lift-off in acetone were performed to first define Ti (5 nm)/Au (60 nm) electrodes to contact black phosphorus and a snake shaped resistor near one end of the device, electrically decoupled from the black phosphorus, to act as a heater element. This was followed by a second EBL step for defining 50 nm thick electrodes of a NiCu alloy by plasma sputtering. All measured samples have a channel width 5–15 μm and, unless otherwise noted, a length of 2.5 μm. The fabricated device architecture combining a field-effect transistor (FET) with thermoelectric circuitry is as depicted in Figure 6-1.

Raman characterization:

We have performed Raman spectroscopy, besides optical microscopy, to identify the black phosphorus flakes used on several of our thermoelectric devices. The Raman laser had a wavelength of 532 nm, spot size of 1 μm and power of 5 mW. We did not perform extensive Raman characterizations for all samples in order to minimize the laser-induced degradation of black phosphorus under ambient conditions[68]. For a few samples we have determined the crystal orientation of black phosphorus via polarization-resolved Raman spectroscopy at different sample orientations, as shown in Figure 6-2. Sample to sample variability due to different thicknesses and ambient degradation forbids at present a direct comparison regarding the possible anisotropy of the thermopower. For this goal further systematic studies with encapsulated samples are required.

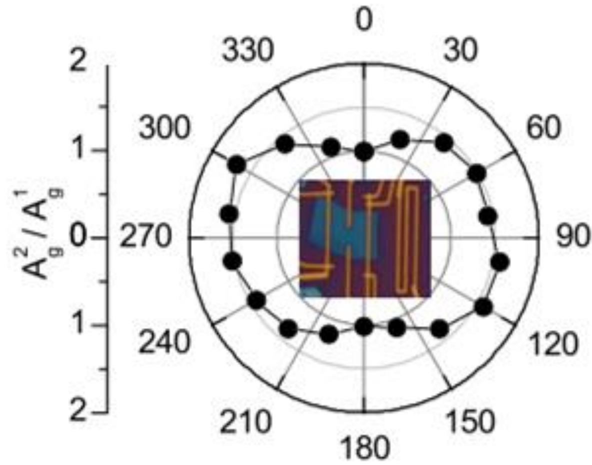

Figure 6- 2: Raman characterization of a black phosphorus based thermoelectric device showing the orientation of the black phosphorus crystal with respect to the heater element. The A^2_g/A^1_g ratio shows that in this device the thermoelectric transport was probed along the light effective mass direction[67].

6.2.2 ELECTRICAL CHARGE TRANSPORT MEASUREMENTS

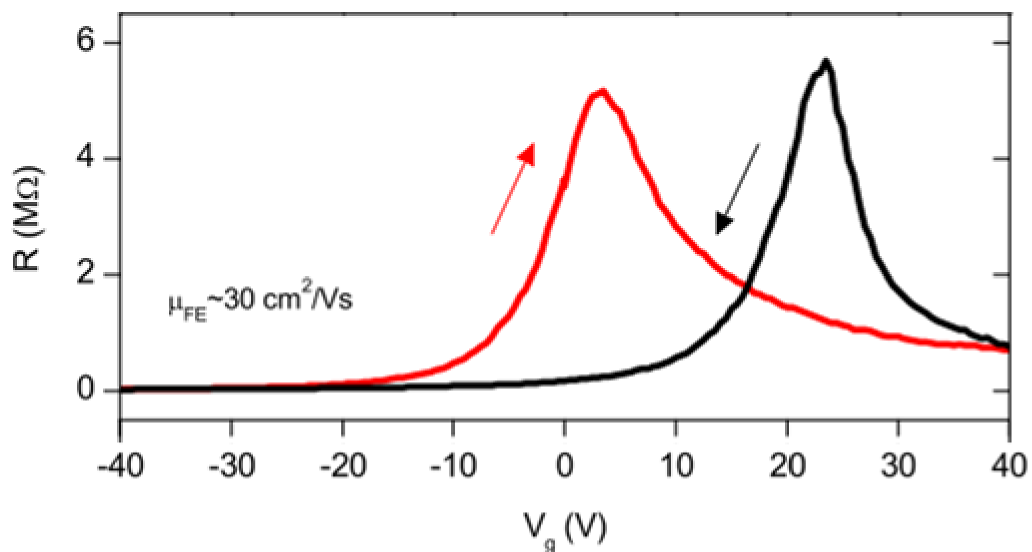

Figure 6- 3: Electrical resistance of the black phosphorus (~12 nm) measured at room temperature with source drain bias of 50 mV.

All electronic measurements were performed in a cryostat under high vacuum conditions with a base pressure of $\sim 10^{-7}$ mbar. We measured the electrical resistance of black phosphorus using the same two gold electrodes used for thermometry and thermopower measurements. We characterize charge transport in the linear regime by applying a dc bias $|V| \leq$ 100 mV, with a voltage source that allows us to measure values >10 GΩ. To account for small current offsets when R>1 GΩ we measure the charge resistance for both polarities $\pm V$ and extract the differential response. For all backgate voltage scans we kept a constant sweep rate (typically 1 V/6 sec) while scanning Vg always along the sequence: 0 → Vmax → −Vmax → Vmax → 0, with Vmax defining the window of Vg values explored. This procedure ensured reproducible results between consecutive scans for both trace (Vmax → −Vmax) and retrace (−Vmax → Vmax) sweeps. The same conditions where used for each reported set of electric and thermoelectric responses.

We first characterize charge transport in few-layer black phosphorus as a function of backgate voltage Vg. The corresponding resistance (R) curves for a 12 nm thick sample are shown in Figure 6-3. We observe a resistance peak for both trace and retrace Vg sweeps, indicating crossing through the bandgap region. The different position of the resistance peak for both traces is consistent with the hysteresis observed at room temperature[118]. Away from this region we see a strong resistance decrease due to the Fermi level shift into the conduction ($Vg \gg 0$ V) or valence ($Vg \ll 0$ V) bands, demonstrating ambipolar FET operation. We extract the field effect mobility[190] $\mu = L/WC \times \partial G/\partial Vg$, where L and W are the length and width of the sample, C the backgate capacitance per unit area, and $G = 1/R$ the conductance. In the hole regime we obtain a field effect mobility ~ 30 cm^{2}V^{-1}s^{-1}, and a current modulation $>10^2$. These characteristics are comparable to recent results.

6.3 THERMOELECTRIC MEASUREMENTS AND FIGURE OF MERIT ZT

Before we discuss on the thermoelectric measurements, it is noteworthy that we re-visit the measurement protocols of different aspects of thermoelectric measurements.

Thermometry:

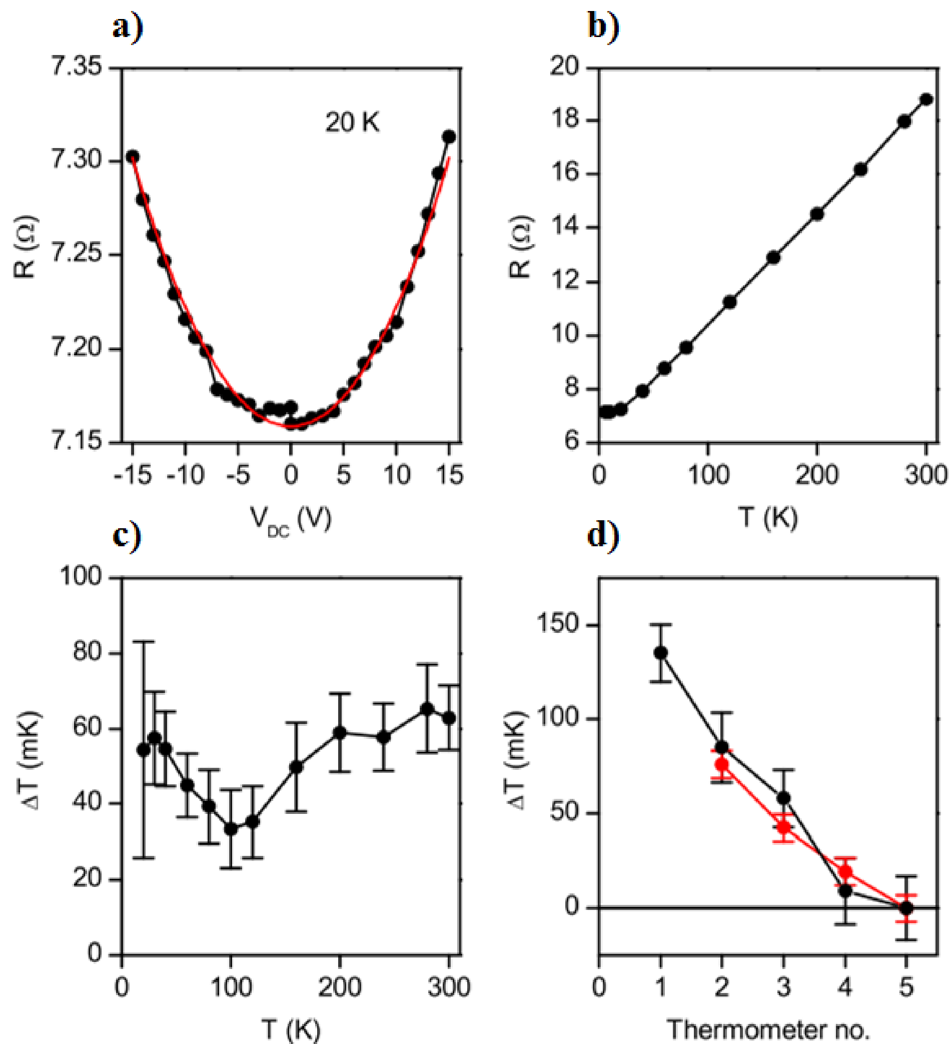

Figure 6- 4: a) Au electrode 4-terminal resistance versus dc bias applied to heater element, at a base temperature of 20 K. The red line is the parabolic fit characteristic of Joule heating. b) Calibration of Au electrode 4-terminal resistance versus temperature. The data in a) and b) are combined to measure the temperature increase at the electrode location due to the heater

element, with a typical resolution of 10 mK. c) Temperature bias ΔT, obtained by subtracting the temperature of two Au electrodes, applied to sample from Figure 6-10 versus reference temperature T. d) Temperature profile at room temperature along a black phosphorus device, referenced to the last electrode. Black symbols correspond to the Au resistive thermometry discussed in the previous panels, the standard method used in this work. Red symbols correspond to the NiCu/Au thermocouple thermometry, showing agreement with the Au thermometry but with a resolution < 5 mK. Error bars in c) and d) are derived from the standard errors in the parabolic fit (as in a)) and in $\partial R/\partial T$ (as in b)).

The resistance of the gold electrodes was measured in a 4-terminal configuration for temperatures between 10 and 300 K (see Figure 6-4). Afterwards they could serve as resistive thermometers for determining the local temperature in black phosphorus under a heat gradient, with a resolution below 10 mK for temperatures above 20 K. By using the thermometry from two gold electrodes we obtained the thermal bias ΔT. For all our measurements $\Delta T < 0.2$ K, satisfying the condition $\Delta T \ll T$ for thermal response in the linear regime. This well-established resistive thermometry method[180,184,185] was used for all the results reported in this work.

As a proof of concept, we expanded on the thermometry method described above by demonstrating nanoscale thermocouple elements that allow us to map the temperature along the two-dimensional black phosphorus channel with increased sensitivity and spatial resolution. We used the NiCu electrodes for NiCu/Au thermocouples, as previously demonstrated in metallic nanostructures[186]. The NiCu thermopower was calibrated in separate devices using the standard resistive thermometry method. We found a good agreement between both methods for thermometry along black phosphorus channels (see Figure 6-4), with the thermocouple method having the advantage of a resolution below 5 mK and a spatial resolution given by the area of the NiCu/Au junction ~500×500 nm^2.

Thermal conductivity:

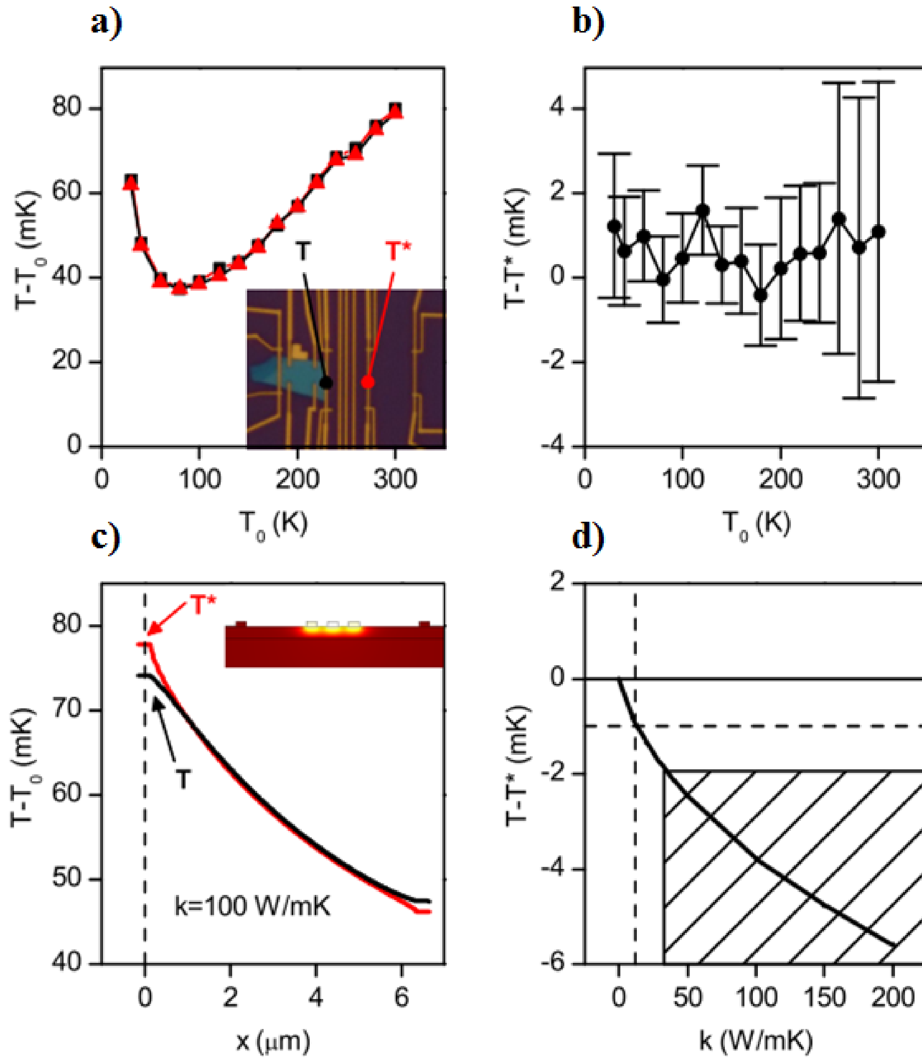

Figure 6- 5: a) Local thermometry for 13 nm black phosphorus (T black) and corresponding 'ghost device' (T* red) under a heater current of 2 mA. The inset is an optical image indicating the location of the thermometry. b) Comparative thermometry from data shown in a. For all base temperatures we observe a difference T-T*≤1 mK. c) Simulation of temperature profile along black phosphorus (black) and 'ghost device' (red) using a model (see inset) of the sample shown in a). Black phosphorus acts as a thermal shunt, leading to a smaller thermal gradient than that of the bare substrate. The dashed line indicates the location of where T and T* are obtained. A large κ= 100 $Wm^{-1}K^{-1}$ is used to make the effect apparent. d) Dependence of T-T* on κ. The result consistent with our measurements (1 mK, κ = 13 $Wm^{-1}K^{-1}$) is indicated by

dashed lines. The hatched area indicates the range ruled out (κ>30 $Wm^{-1}K^{-1}$) by our measurements.

In addition to the standard thermometry to determine the local temperature in few-layer black phosphorus, we have also devised a method which allows us to measure the thermal conductivity of the black phosphorus channel. For this we have included in some of our samples a 'ghost device': an electrode structure (without any black phosphorus) which mirrors the electrode structure contacting the black phosphorus channel on the opposite side of the heater element. By measuring the local temperature of equivalent thermometers on opposite sides of the same heater element (i.e. on the black phosphorus device and on the ghost device) we perform a comparative measurement to detect a change in the temperature profile due to thermal transport via the few-layer black phosphorus flake. The measurements (see Figure 6-5) show that any deviation between the temperatures of the two equivalent thermometers is comparable with the maximum accuracy of our thermometry (1 mK). Since the temperature profile is dominated by the 300 nm SiO2 substrate (with κ_{ox} = 1 $Wm^{-1}K^{-1}$ at room temperature) and our black phosphorus flakes are ~ 10 nm thick, this result places a strong upper limit κ<30 $Wm^{-1}K^{-1}$ for the thermal conductivity of few layer black phosphorus. We remark that the more standard approach of making suspended structures for the thermal conductivity measurement is not compatible with the fabrication process of the few-layer black phosphorus FET devices described in this work.

To extract a more accurate value of the thermal conductivity of few-layer black phosphorus we complement our measurements with numerical simulations of thermal transport in realistic models of our devices using finite element modelling software (COMSOL Multiphysics). The simulation results (see Figure 6-5) confirm our analysis of the upper limit of the thermal conductivity. Remarkably, they show that the observed deviation of ~1 mK corresponds to a thermal conductivity of κ=13 $Wm^{-1}K^{-1}$. The agreement between this extraced

value and the reported thermal conductivity of bulk black phosphorus[189] (12 $Wm^{-1}K^{-1}$) therefore validates the use of the latter for the estimation of the figure of merit *ZT*.

Thermoelectric:

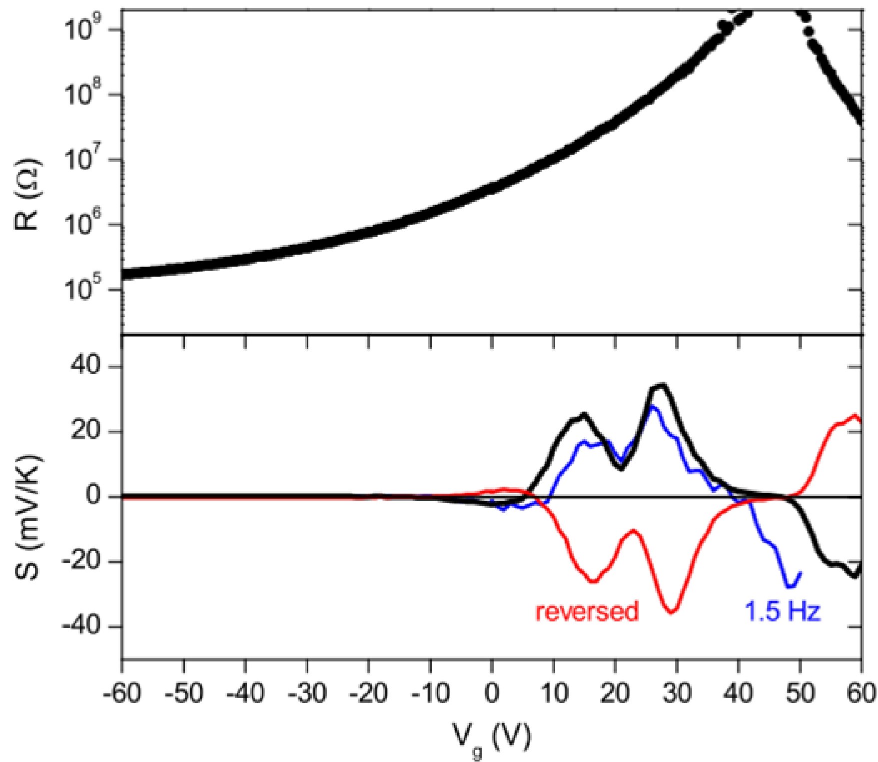

Figure 6- 6: Room temperature thermoelectric response for sample from Figure 6-10, before cooldown. a) Electrical resistance. b) Seebeck coefficient. The bandgap region is visible as the highly insulating region where the Seebeck coefficient becomes zero. The black curve corresponds to the standard lock-in measurement configuration at 4 Hz, same as in Figure 6-10. The red curve corresponds to inverting the voltage probes, its similar magnitude and opposite polarity to the standard configuration demonstrates the differential nature of the measurement and the absence of any significant common-mode signal. The blue curve is a standard measurement at 1.5 Hz (and half the Vg sweep rate), its similar magnitude and lineshape to the measurement at 4 Hz demonstrates the quasi-steady-state equilibrium in the range of frequencies used (1.5–4 Hz).

For the thermoelectric measurements we applied a low frequency ($\omega/2\pi$<5 Hz) ac signal to the heater element to produce an alternating heat gradient and measured the 2ω thermopower response in black phosphorus due to Joule heating. The thermopower is then obtained as $S=\sqrt{2}V_{2y}/\Delta T$, where V_{2y} is the second harmonic signal, with a 90 ° phase shift, measured using a lock-in technique with an input impedance of 100 MΩ that allows a large signal-to noise ratio[180,182,185]. Contribution from higher harmonics, common-mode signals and frequency-dependent capacitive coupling was found to be negligible (see Figure 6-6).

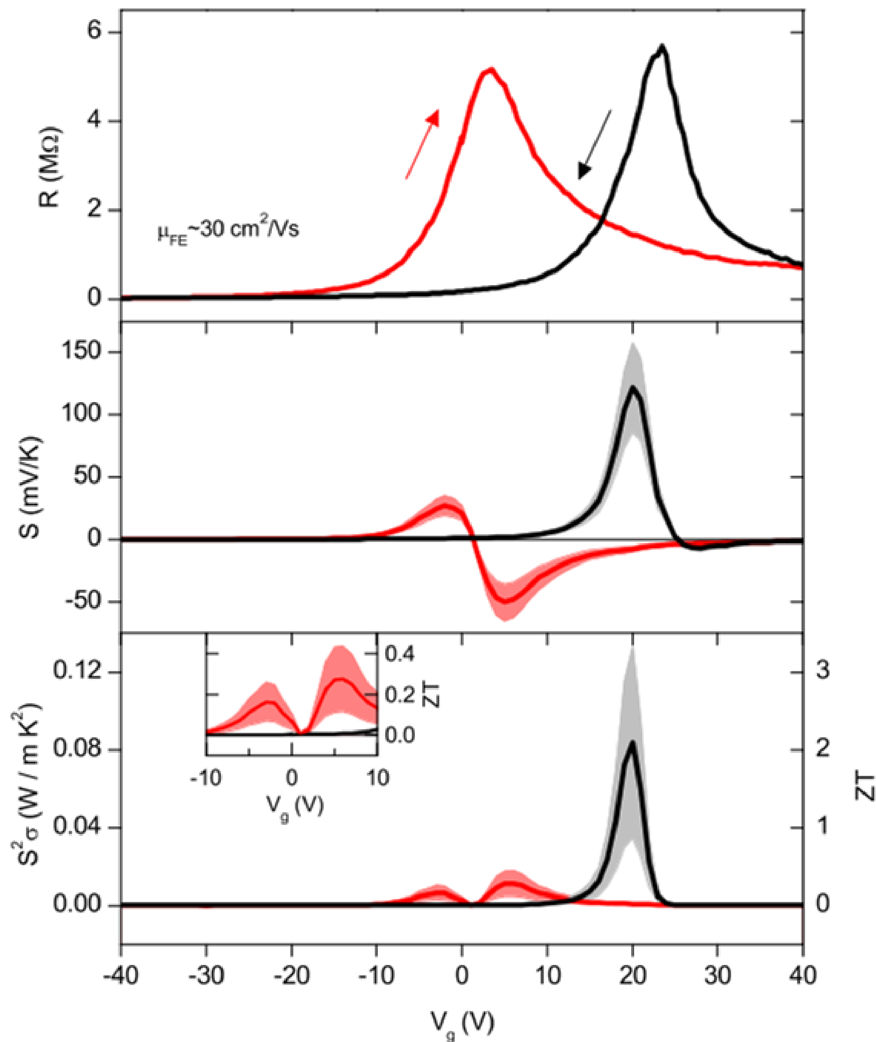

Figure 6- 7: Thermoelectric response in 12 nm thick black phosphorus at room temperature. a) and b) Electrical resistance (V=50 mV) and Seebeck coefficient (ΔT=170 mK). c) Power factor

$S^2\sigma$ calculated from data in a) and b) and ZT considering a thermal conductivity κ=12 $Wm^{-1}K^{-1}$. The inset zooms into the region around Vg=0. For all panels black and red lines correspond to Vg trace (40→40) and retrace (-40→40) sweeps, respectively. The gray and light red bands are errors due to ΔT.

With the above measurement procedures, we are now in position to characterize thermoelectric transport. For this we apply a thermal gradient along the black phosphorus channel and determine the thermopower $S=-\Delta V/\Delta T$. In Figure 6-7 (middle panel) we note the general features of the expected thermopower response: $S>0$ for the hole regime, $S<0$ for the electron regime, and a crossing through zero corresponding to the bandgap region. A detailed look reveals a different electron-hole asymmetry of the thermopower for trace and retrace sweeps. While hysteresis manifests itself in transport as a shift of the resistance peak, its effect in the thermopower is more profound. We attribute this to the high sensitivity of the thermopower to the electronic structure close to the band edges[111,184], as it depends on the distribution of adsorbed impurities and interfacial charge traps both of which are modulated by the gate electric field[68,118]. A second observation is the large values of the thermopower up to 120 (50) mVK^{-1} close to the hole (electron) band edge. These are the largest values for any two-dimensional crystal as directly measured with the device architecture of Figure 6-1 (with a second place of 30 mVK^{-1} for MoS2[183]) and are a factor $\sim 10^3$ higher than for graphene[180–182] and semiconducting carbon nanotubes[184].

A quantity related to the figure of merit is the thermoelectric power factor $S^2\sigma$, which serves to quantify the ability to convert thermal energy into electrical energy without regard to the efficiency of the process. From our charge and thermoelectric transport results we can directly extract the power factor as shown in Figure 6-7 (bottom panel). We obtain large power factor of up to 0.08 (0.01) $Wm^{-1}K^{-2}$ close to the hole (electron) band edge. To calculate the figure of merit we need the thermal conductivity κ, for which there is no experimental

measurement in few-layer black phosphorus yet. To address this issue we have devised a method to measure κ for our device architecture (see section on Thermal conductivity) and extract a thermal conductivity ~13 $Wm^{-1}K^{-1}$, in agreement with the reported value of κ=12 $Wm^{-1}K^{-1}$ for bulk black phosphorus[189]. We therefore take the latter as a conservative estimate, for ultrathin films its value may be reduced via boundary scattering. The end result is a maximum figure of merit of 2.1 (0.2) for the hole (electron) band edge. Such an exceptional *ZT*~2.1 is comparable to state of the art nanostructured materials[188] with a maximum reported *ZT*~2.4 for Bi_2Te_3/Sb_2Te_3 superlattices[191] at room temperature, whereas here it is achieved in an elemental semiconductor without the requirement of any complex superlattice.

It is worth to note that the calculation of the figure of merit *ZT*, for all our devices we found that the electronic contribution κ_e to the thermal conductivity was negligible. Using the Wiedemann-Franz law $\kappa_e = L\sigma T$, with L the Lorenz number, we found that κ_e is smaller than κ=12 $Wm^{-1}K^{-1}$ by a factor >10^3.

6.4 THERMOELECTRIC RESPONSE FOR THINNER BLACK PHOSPHORUS

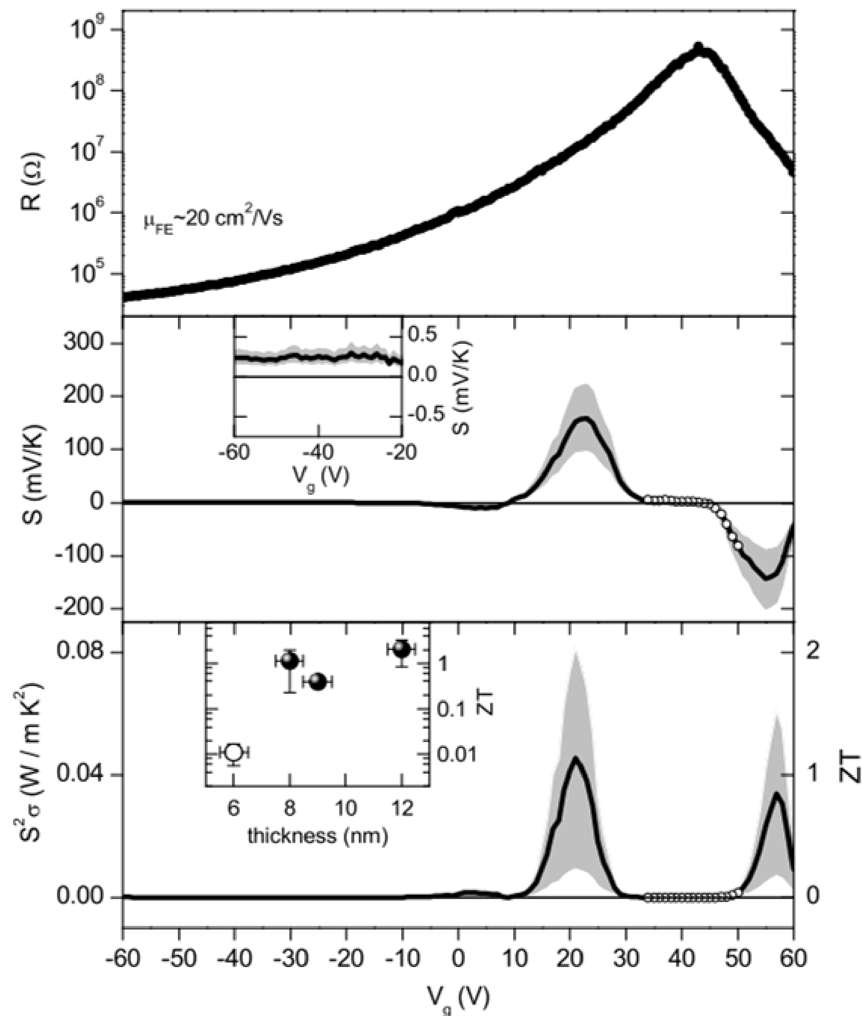

Figure 6- 8: Thermoelectric response for 8 nm thick black phosphorus showing bandgap region at room temperature. a) and b) Electrical resistance (V=100 mV) and Seebeck coefficient (ΔT=50 mK). The bandgap region is visible as the highly insulating region where the Seebeck coefficient becomes zero. The inset in b zooms into the region of large hole doping showing saturation of the Seebeck coefficient to a value of 200 μV/K. c) Power factor $S^2\sigma$ calculated from data in a) and b) and ZT considering a thermal conductivity κ=12 $Wm^{-1}K^{-1}$. The inset shows the maximum ZT values achieved for different thicknesses. Open symbols in b) and c) correspond to R > 100 MΩ. The gray bands are errors due to ΔT.

Next, we explore the response of thinner devices and address what are the limitations for exploring the single-layer phosphorene limit. The rest of the samples showed similar (albeit smaller) effects of the hysteresis, so below we focus on trace sweeps. In Figure 6-8 (top panel) we present the results for a thinner sample, 8 nm thick. The electrical response shows a highly insulating region and a modulation of 10^4 in the hole regime, a factor $\sim 10^2$ larger than for the thicker sample (previous sub-chapter). For large hole doping the mobility of both samples are comparable. These results are consistent with a more uniform electrostatic gating in thinner channels allowing us to reach the bandgap throughout its whole thickness, whereas thicker samples are limited by screening of the backgate electric field[60,69]. The enhanced electrostatic gating is evident in the thermoelectric response (see Figure 6-8, middle panel) showing a clear separation of hole and electron bands by a bandgap region where the thermopower approaches zero. We observe again large thermopower values, with a more symmetric electron-hole response up to ~ 150 mVK^{-1}. The narrow bandgap in few-layer black phosphorus offers the advantageous combination of a clear separation of electron and hole bands at room temperature with the ability to easily achieve ambipolar FET operation. Together with a sizable electrical conductivity, these characteristics makes black phosphorus an interesting material for thermoelectrics. This assertion is confirmed by the obtained large power factor of ~ 0.04 $Wm^{-1}K^{-2}$ and figure of merit $ZT \sim 1.0$ for both electron and holes (see Figure 6-8, bottom panel).

The maximum figure of merit for different thicknesses is shown in the inset of Figure 6-8 (bottom panel). For thickness below ~10 nm black phosphorus exhibits a decreased mobility due to interaction with substrate and surface impurities[60,69] and degradation under ambient conditions[68,118], which we have observed in a highly resistive 6 nm sample (see Figure 6-9). The extracted figure of merit ZT for this 6 nm sample is a lower limit, because of a twofold effect from the extrinsic decrease in conductance. First, via the direct dependence $ZT \propto \sigma$.

Second, indirectly via the dependence $ZT \propto S^2$, because the measured thermopower will be underestimated when the sample resistance increases above the input impedance of the measurement instrument[185], in our case 100 MΩ. Therefore, we conclude that the limitations for exploring thermoelectric transport down to phosphorene thickness are extrinsic (impurity scattering and instrumentation) and that few-layer black phosphorus is a high performance thermoelectric material with a large figure of merit at room temperature.

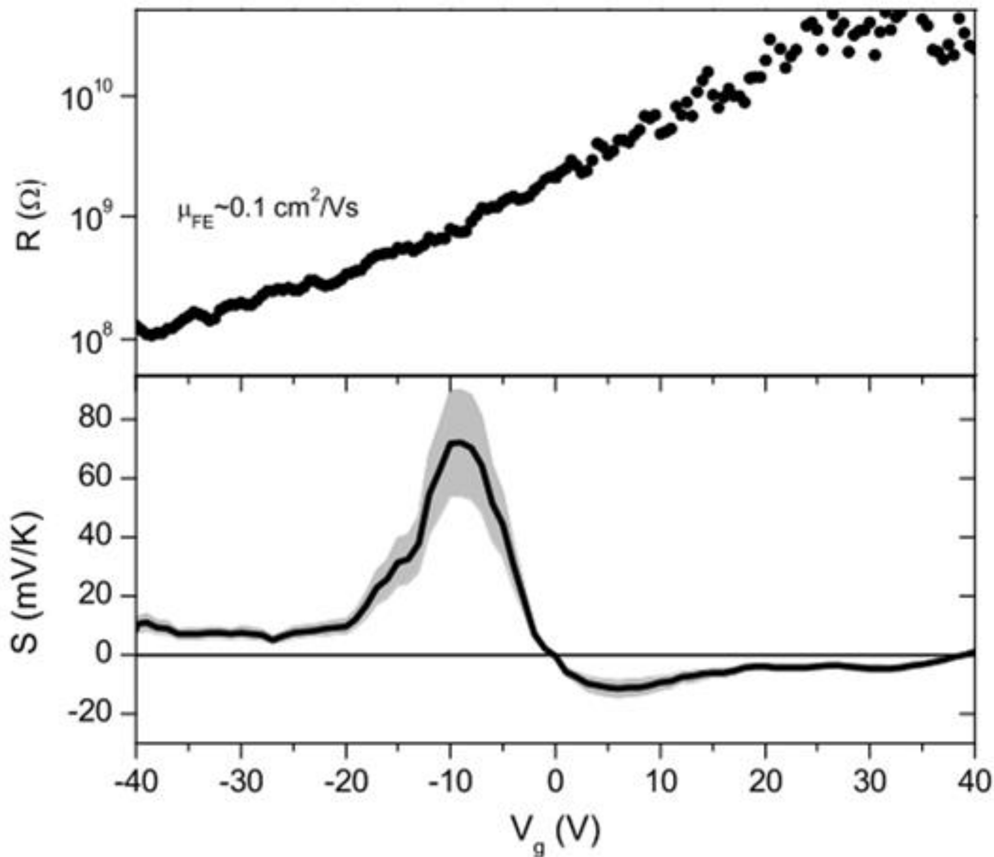

Figure 6- 9: Thermoelectric response for 6 nm thick black phosphorus at room temperature. a) Electrical resistance (V=100 mV). b) Seebeck coefficient (ΔT=200 mK). The gray band is the error due to ΔT. Compared with the thicker samples, this sample showed lower mobility, a larger bandgap region and unipolar FET operation. The Seebeck coefficient is underestimated due to the resistance of the sample being > 100 MΩ.

6.5 PHONON DRAG IN BLACK PHOSPHORUS

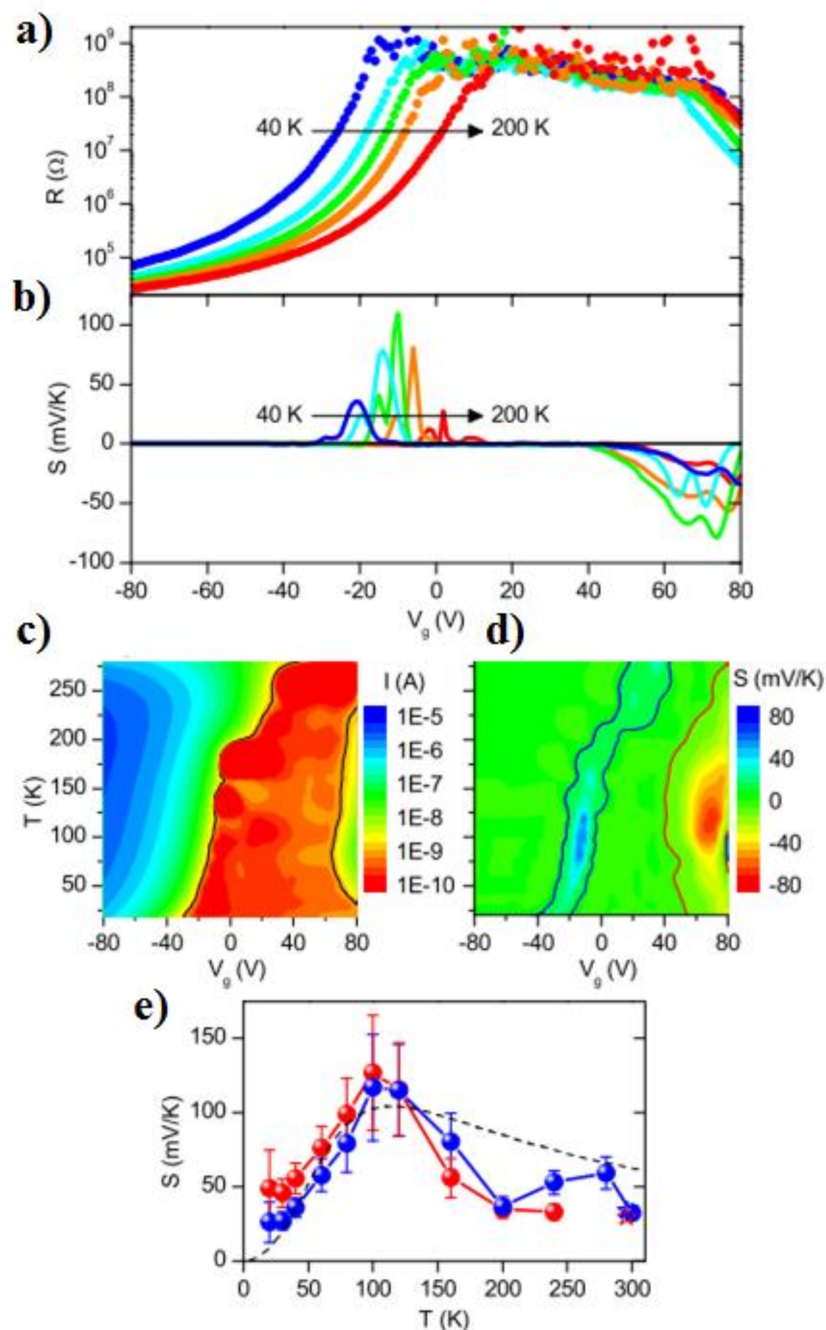

Figure 6- 10: Low temperature thermoelectric response. a) and b) Electrical resistance and Seebeck coefficient at different temperatures for 8 nm thick, 8.5 μm long sample. The electrical response showed no significant hysteresis for T<200 K (Figure 6-11). c) and d) 2D maps of the temperature dependence of the electric (V=100 mV) and thermoelectric responses,

respectively. Black contours in c correspond to I = 10^{-9} A indicating the band edges. Blue (red) contours in d) correspond to S=+(-)3 mVK^{-1}. e) Maximum Seebeck coefficient versus temperature. Red (blue) symbols correspond to electron (hole) regime. Open stars correspond to the initial room temperature measurement (Figure 6-6). Error bars are due to uncertainty in ΔT. The dashed line is the phonon-drag model described in the discussion.

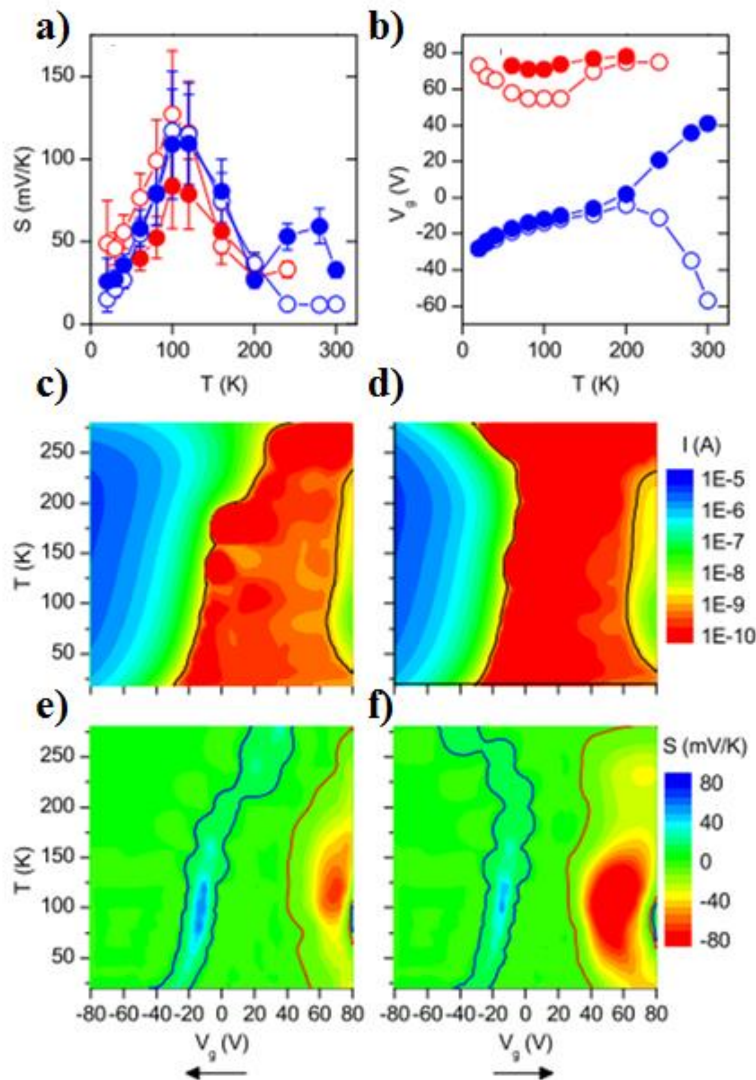

Figure 6- 11: Low temperature thermoelectric response including trace and retrace analysis, for sample from Figure 6-10. a) Maximum Seebeck coefficient versus temperature, separately for Vg trace (80→80) and retrace (-80→80) sweeps. Red and blue symbols correspond to electron and hole regimes. Filled and open symbols correspond to trace and retrace sweeps.

Error bars are due to uncertainty in ΔT. b) Vg position of Seebeck maximum versus temperature. Symbols have the same meaning as in a. Note the absence of hysteresis below 200 K for the electric response and for the maximum hole thermopower. 2D maps of the temperature dependence are shown for the electric response (V=100 mV) in c) (trace) and d) (retrace), and for the thermoelectric response in e) (trace) and f) (retrace). Black contours in c) and d) correspond to R=100 MΩ, indicating the band edges. Blue (red) contours in e) and f) correspond to S=+(-)3 mVK^{-1}.

Recent theoretical predictions for black phosphorus[47] show a predicted thermopower a factor of $\sim 10^3$ smaller than in our devices. These theoretical predictions are based on the semi-classical Boltzmann theory under the assumption of relaxation times equal to those of bulk black phosphorus and therefore might not represent the experimental state of the art in few-layer devices. Furthermore, the predicted thermopower was calculated within the framework of thermoelectricity driven by electron diffusion so it can only account for diffusive thermopower[111]. The disagreement between measured and predicted thermopower hints to a hitherto unexplored physics. To address this issue we have conducted temperature dependent measurements in another 8 nm sample, which also showed a large thermopower ~ 30 mV/K at room temperature. As shown in Figure 6-10 and Figure 6-11, the maximum thermopower closely follows both electron and hole band edges and shows a non-monotonic temperature dependence with a broad peak at T ~100 K. These features have been further reproduced in a 9 nm sample as shown in Figure 6-12. The large magnitude and non-monotonic temperature dependence are inconsistent with diffusive thermopower, as this mechanism usually results in values < 1 mVK^{-1} and a monotonic increase with temperature[180,181,184]. On the other hand, these observations are consistent with a thermopower dominated by the mechanism of phonon drag[192].

Phonon drag thermopower is generated due to scattering of electrons by phonons diffusing along the heat gradient. It has been invoked as the mechanism behind the observation of colossal thermopower in high-purity low-doped semiconductors, including Ge (10 mVK^{-1})[193], bulk Si (20 mVK^{-1})[194] and Si nanowires (0.4 mVK^{-1})[195], and narrow-gap semiconductors $FeSb_2$ (1 mVK^{-1})[196] and $CrSb_2$ (5 mVK^{-1})[197]. We note that in black phosphorus phonons are also the dominant contribution to the thermal conductivity κ[189]. We can understand the non-monotonic temperature dependence from a basic model of phonon-drag contribution[111] $Sp \propto c \times \alpha$, with c the specific heat of the lattice, and $\alpha = l_p/(l_p + l_{pe})$ a parameter relating the mean-free paths for phonon-electron scattering (l_{pe}) and all other phonon scattering where momentum is not conserved (l_p). Modeling the specific heat c using the Debye temperature for black phosphorus ($T_D = 400$ K)[189] and a temperature dependence $\alpha \propto T^{-1}$ for phonon-phonon Umklapp scattering, we obtain the line shape shown in Figure 6-10, with a peak at $\sim T_D/5$[111] and in reasonable agreement with our data. The simple model above can only account for a qualitative description. A first order quantitative estimate[194,196,197] from the theory of phonon drag in semiconductors is given by[192] $S_p = \beta v_s l_p / \mu T$, where v_s is the velocity of sound and $\beta \subset (0, 1)$ indicates the relative contribution of electron-phonon interaction to electron mobility. We estimate the phonon mean free path using the Debye equation $\kappa = c v_s l_p / 3$, with $v_s = 4000$ ms^{-1} and the reported values of thermal conductivity[189], yielding $l_p \sim 30$–120 nm for intermediate temperatures 50–100 K. We remark that this estimated l_p is an effective lower bound involving all phonons, whereas for phonon drag only phonons with small wave vector and larger mean free paths are relevant[192,194]. Finally, the measured mobilities at the thermopower maxima were ~0.1 $cm^2V^{-1}s^{-1}$. The resulting estimate, $S_p = \beta \times (100\text{–}1000)$ mVK^{-1}, confirms that phonon drag can account for the large thermopower.

Our findings demonstrate that few-layer black phosphorus is a high performance thermoelectric material and set the stage for further studies down to its single layer,

phosphorene. Further open questions include the reduction of sample to sample variability by controlling device quality via encapsulation, which will also enable the study of anisotropic thermopower. Considering it is an elemental semiconductor without the requirements of complex superlattices[191] nor nanostructuring[188], few-layer black phosphorus is a two-dimensional crystal with potential for its use in thermoelectrics[187].

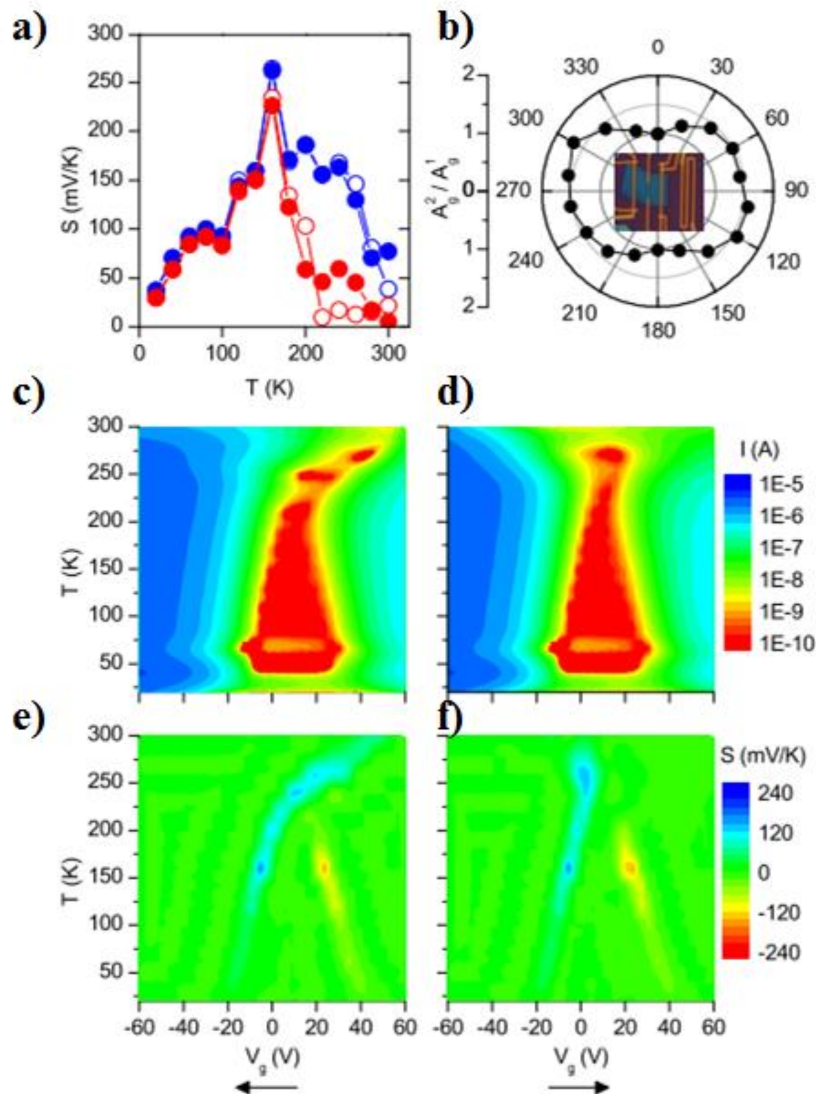

Figure 6- 12: Additional low temperature thermoelectric response for 9 nm thick black phosphorus. a) Maximum Seebeck coefficient versus temperature, separately for Vg trace (60→60) and retrace (-60→60) sweeps. Red and blue symbols correspond to electron and hole

regimes. Filled and open symbols correspond to trace and retrace sweeps. b) Raman characterization of the same device showing the orientation of the black phosphorus flake with respect to the heater element. The $A^2_g=A^1_g$ ratio shows that in this device thermoelectric transport was probed along the light effective mass direction. Similarly to the previous sample, 2D maps of the temperature dependence are shown for the electric response (V=50 mV) in c) (trace) and d) (retrace), and for the thermoelectric response in e) (trace) and f) (retrace).

CHAPTER 7 SUMMARY AND FUTURE WORK

7.1 GRAPHENE SPINTRONICS

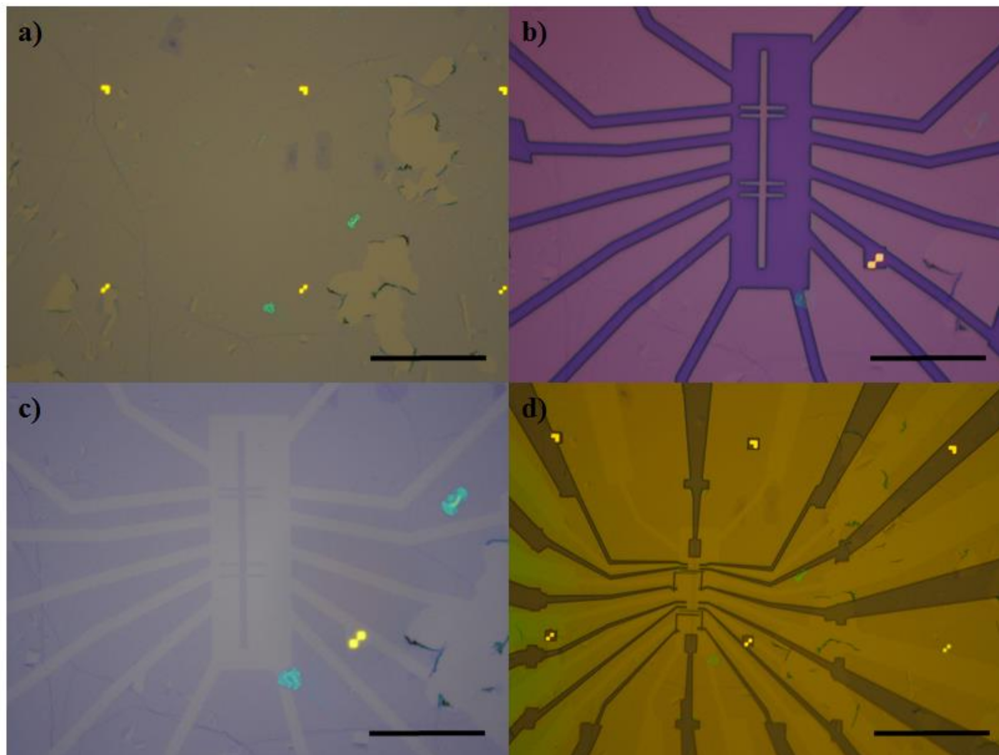

Figure 7- 1: Optical microscope images. a) After deposition of metal alignment markers to locate area of clean CVD graphene. b) After patterning of etch mask to define the final device channel. c) After liftoff of etch mask resist in acetone. d) After patterning of device electrodes for MgO and Co depositions. Scale bar is 20 µm.

The next stage of graphene spintronics work would be to combine spin Hall configuration together with non-local spin valve electrodes to perform direct measurement of spin accumulations due to spin Hall Effect with ferromagnetic contacts.

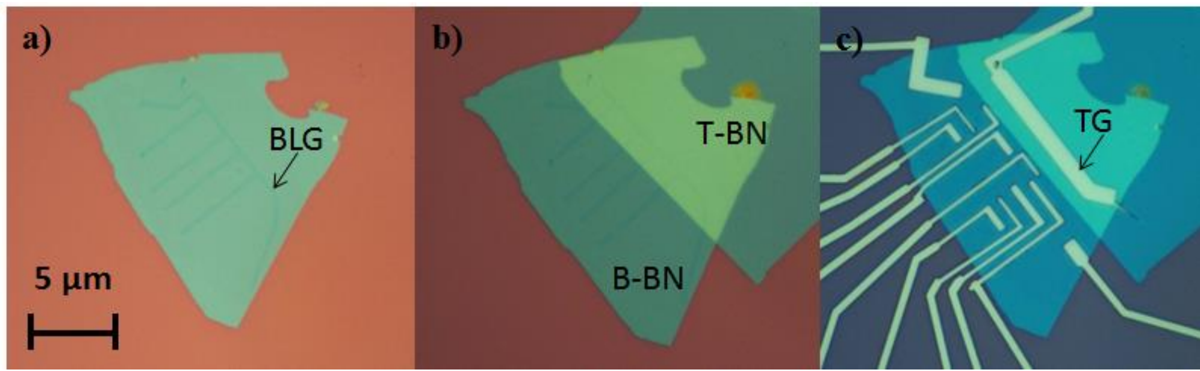

Figure 7- 2: a) Optical microscope image of etched bilayer graphene on BN substrate. b) Optical microscope image after second transfer of BN top gate. c) Optical image after complete device fabrication showing top and bottom gates.

Another graphene spintronics experiment that can be pursued is to study the spin transport in bilayer graphene under band gap opening. It will be scientifically interesting to see how the spin parameters in graphene are affected under the opening of band gap through an additional fabricated top gate.

7.2 BLACK PHOSPHORUS THERMOELECTRIC

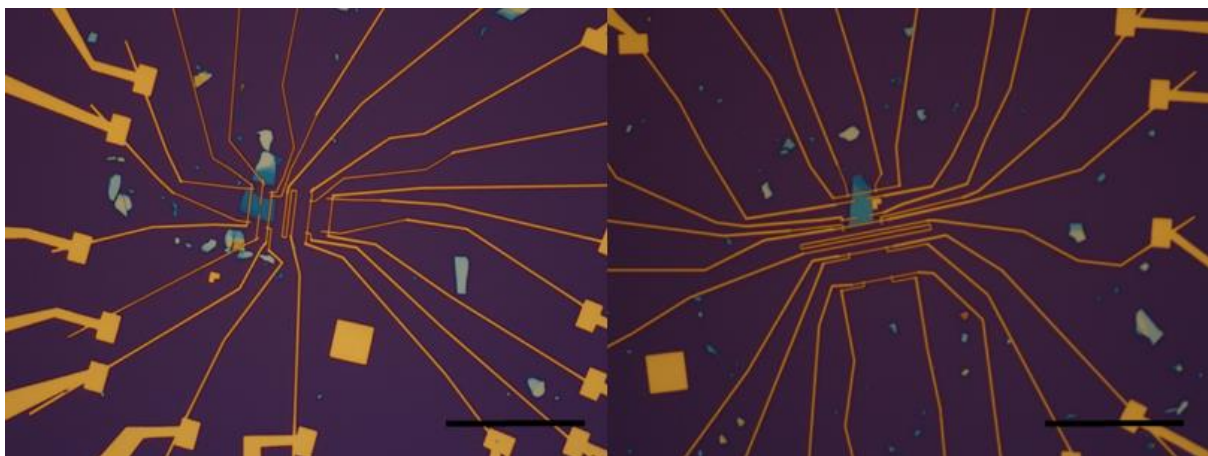

Figure 7- 3: Optical microscope images of two different black phosphorus based thermoelectric device with lateral contacts for the measurement of Nernst effect. Scale bar is 20 µm.

Motivated by our promising results in thermoelectric response of black phosphorus, we fabricated new thermoelectric devices based on black phosphorus with the addition of lateral contacts to study the thermal Nernst effect under applied magnetic field. Results from these

measurements will provide us with more details on the phonon-drag mechanism that governs the thermal transport in this material.

7.3 BLACK PHOSPHORUS ULTRAVIOLET PHOTODETECTOR

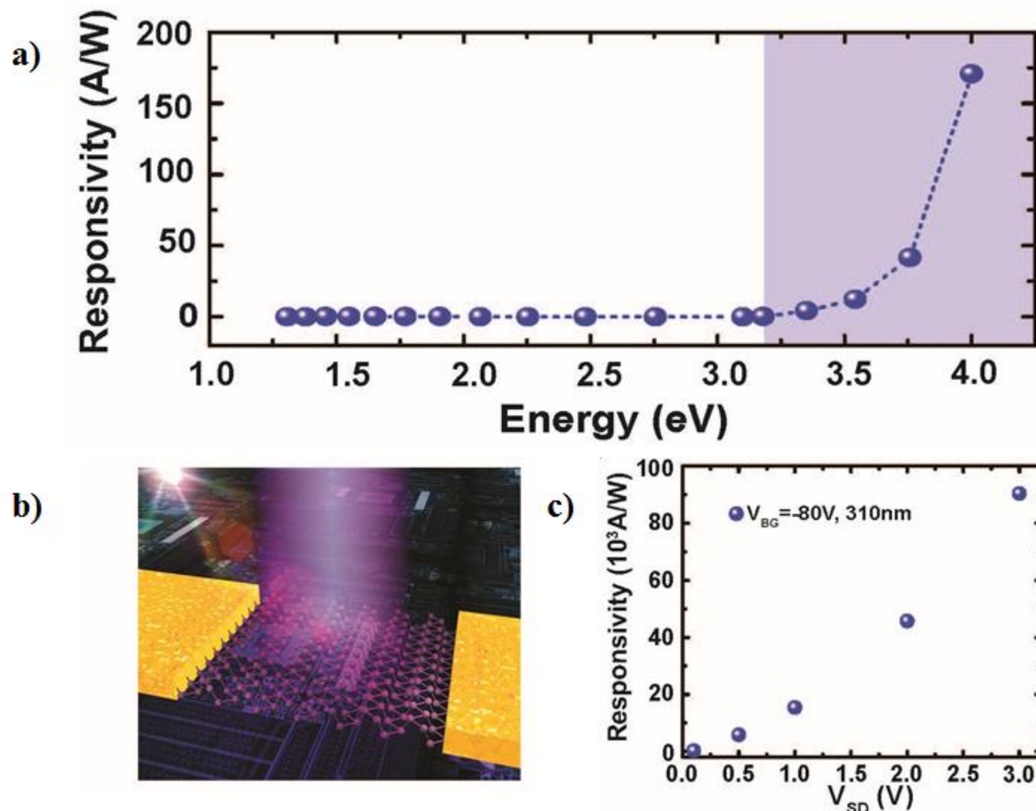

Figure 7- 4: a) Photo-responsivity of device within energy range of 1-4 eV measured at source drain bias V_{SD}=0.1 V. b) Three-dimensional schematics of the device structure used to measure photo-response. c) Photo-responsivity in the ultraviolet regime as a function of source drain bias V_{SD}.

Extensive work has been performed and submitted on black phosphorus based photodetector. Black phosphorus exhibits a layer-dependent direct band gap from monolayer to bulk; a crucial property for photo-detection. Driven by this, we studied the optoelectronics characteristics of few-layer black phosphorus-based photodetectors over a wide spectrum ranging from near ultraviolet (UV) to near infrared (NIR). We demonstrated for the first time that black phosphorus can be configured as an excellent UV photodetector with a specific

detectivity ~ 3×10^{13} Jones. More critically, we found that the UV photo-responsivity can be significantly enhanced to ~9×10^{4} AW^{-1} by applying a source-drain bias (V_{SD}) of 3 V, which is the highest ever measured in any 2D materials and 10^{7} times higher than previous reported value for black phosphorus. Such colossal UV photo responsivity is mainly attributed to the resonant-interband transition between two special nested valence band and conduction band, which provides unusual high density of states for the high-efficient UV absorption due to their singularity nature. This work has been submitted with me as an equally contributing author at the present time of this thesis (see List of Publications (3)).

7.4 BLACK PHOSPHORUS SPINTRONICS

Figure 7- 5: Optical microscope image of a black phosphorus based non-local spin valve device with MgO and Co electrodes. Scale bar is 20 μm.

Finally, spintronics studies in black phosphorus have been ongoing with the objective of understanding spin transport in a tunable band gap system. Observation of first spin transport in black phosphorus will be of significant importance especially toward making spin field effect transistors.

BIBLIOGRAPHY

1. Balakrishnan, J., Koon, G. K. W., Jaiswal, M., Castro Neto, A. H. & Özyilmaz, B. Colossal enhancement of spin-orbit coupling in weakly hydrogenated graphene. *Nat. Phys.* **9,** 284–287 (2013).
2. Balakrishnan, J. *et al.* Giant spin Hall effect in graphene grown by chemical vapour deposition. *Nat. Commun.* **5,** (2014).
3. Wolf, S. A. *et al.* Spintronics: A Spin-Based Electronics Vision for the Future. *Science* **294,** 1488–1495 (2001).
4. Thomson, W. The Bakerian Lecture - On the Electro-dynamic Qualities of Metals. *Philos. Trans. R. Soc. Lond.* **146,** 649–751 (1856).
5. Thomson, W. On the Electro-Dynamic Qualities of Metals: Effects of Magnetization on the Electric Conductivity of Nickel and of Iron. *Proc. R. Soc. Lond.* **8,** 546–550 (1856).
6. Smit, J. Magnetoresistance of ferromagnetic metals and alloys at low temperatures. *Physica* **17,** 612–627 (1951).
7. Dirac, P. A. M. *The Principles of Quantum Mechanics*. (Oxford University Press, 1958).
8. Uhlenbeck, G. E. & Goudsmit, S. Spinning Electrons and the Structure of Spectra. *Nature* **117,** 264–265 (1926).
9. Awschalom, D. D., Loss, D. & Samarth, N. *Semiconductor Spintronics and Quantum Computation*. (Springer Science & Business Media, 2002).
10. Prinz, G. A. Magnetoelectronics. *Science* **282,** 1660–1663 (1998).
11. Datta, S. & Das, B. Electronic analog of the electro-optic modulator. *Appl. Phys. Lett.* **56,** 665–667 (1990).
12. Åkerman, J. Toward a Universal Memory. *Science* **308,** 508–510 (2005).
13. Aronov, A. G. & Pikus, G. E. Spin injection into semiconductors. *Sov. Phys. Semicond.-Ussr* **10,** 698–700 (1976).

14. Rashba, E. I. Theory of electrical spin injection: Tunnel contacts as a solution of the conductivity mismatch problem. *Phys. Rev. B* **62,** R16267 (2000).

15. Johnson, M. & Silsbee, R. H. Interfacial charge-spin coupling: Injection and detection of spin magnetization in metals. *Phys. Rev. Lett.* **55,** 1790–1793 (1985).

16. Johnson, M. & Silsbee, R. H. Coupling of electronic charge and spin at a ferromagnetic-paramagnetic metal interface. *Phys. Rev. B* **37,** 5312–5325 (1988).

17. Johnson, M. & Silsbee, R. H. Spin-injection experiment. *Phys. Rev. B* **37,** 5326–5335 (1988).

18. Baibich, M. *et al.* Giant Magnetoresistance of (001)Fe/(001)Cr Magnetic Superlattices. *Phys. Rev. Lett.* **61,** 2472–2475 (1988).

19. Binasch, G., Grünberg, P., Saurenbach, F. & Zinn, W. Enhanced magnetoresistance in layered magnetic structures with antiferromagnetic interlayer exchange. *Phys. Rev. B* **39,** 4828–4830 (1989).

20. Meservey, R., Tedrow, P. M. & Fulde, P. Magnetic Field Splitting of the Quasiparticle States in Superconducting Aluminum Films. *Phys. Rev. Lett.* **25,** 1270–1272 (1970).

21. Meservey, R. & Tedrow, P. M. Spin-polarized electron tunneling. *Phys. Rep.* **238,** 173–243 (1994).

22. Jedema, F. J., Filip, A. T. & van Wees, B. J. Electrical spin injection and accumulation at room temperature in an all-metal mesoscopic spin valve. *Nature* **410,** 345–348 (2001).

23. Jedema, F. J., Heersche, H. B., Filip, A. T., Baselmans, J. J. A. & van Wees, B. J. Electrical detection of spin precession in a metallic mesoscopic spin valve. *Nature* **416,** 713–716 (2002).

24. Jedema, F. J., Nijboer, M. S., Filip, A. T. & van Wees, B. J. Spin injection and spin accumulation in all-metal mesoscopic spin valves. *Phys. Rev. B* **67,** 085319 (2003).

25. Tombros, N., van der Molen, S. J. & van Wees, B. J. Separating spin and charge transport in single-wall carbon nanotubes. *Phys. Rev. B* **73,** 233403 (2006).

26. Dyakonov, M. I. & Perel, V. I. Current-induced spin orientation of electrons in semiconductors. *Phys. Lett. A* **35,** 459–460 (1971).

27. Hirsch, J. Spin Hall Effect. *Phys. Rev. Lett.* **83,** 1834–1837 (1999).

28. Kato, Y. K., Myers, R. C., Gossard, A. C. & Awschalom, D. D. Observation of the Spin Hall Effect in Semiconductors. *Science* **306,** 1910–1913 (2004).

29. Wunderlich, J., Kaestner, B., Sinova, J. & Jungwirth, T. Experimental Observation of the Spin-Hall Effect in a Two-Dimensional Spin-Orbit Coupled Semiconductor System. *Phys. Rev. Lett.* **94,** 047204 (2005).

30. Iijima, S. Helical microtubules of graphitic carbon. *Nature* **354,** 56–58 (1991).

31. Tombros, N., Jozsa, C., Popinciuc, M., Jonkman, H. T. & van Wees, B. J. Electronic spin transport and spin precession in single graphene layers at room temperature. *Nature* **448,** 571–574 (2007).

32. Žutić, I., Fabian, J. & Das Sarma, S. Spintronics: Fundamentals and applications. *Rev. Mod. Phys.* **76,** 323–410 (2004).

33. Hueso, L. E. *et al.* Transformation of spin information into large electrical signals using carbon nanotubes. *Nature* **445,** 410–413 (2007).

34. Dlubak, B. *et al.* Highly efficient spin transport in epitaxial graphene on SiC. *Nat. Phys.* **8,** 557–561 (2012).

35. Loh, K. P., Bao, Q., Ang, P. K. & Yang, J. The chemistry of graphene. *J. Mater. Chem.* **20,** 2277–2289 (2010).

36. Weeks, C., Hu, J., Alicea, J., Franz, M. & Wu, R. Engineering a Robust Quantum Spin Hall State in Graphene via Adatom Deposition. *Phys. Rev. X* **1,** 021001 (2011).

37. Seebeck, T. J. Ueber die magnetische Polarisation der Metalle und Erze durch Temperatur-Differenz. *Ann. Phys.* **82,** 133–160 (1826).

38. Thomson, W. On the Dynamical Theory of Heat. Trans. *R Soc Edinb. Earth Sci* **3,** 91–98 (1851).

39. Altenkirch, E. Über den Nutzeffekt der Thermosäule. *Phys. Zeitschrif* **10,** 560–580 (1909).

40. Slack, G. A. Nonmetallic crystals with high thermal conductivity. *J. Phys. Chem. Solids* **34,** 321–335 (1973).

41. Heikes, R. R. & Ure, R. W. *Thermoelectricity: science and engineering*. (Interscience Publishers New York, 1961).

42. Ioffe, A. F. Semiconductor thermoelements and thermoelectric cooling. (1957).

43. Vedernikov, M. V. & Iordanishvili, E. K. A.F. Ioffe and origin of modern semiconductor thermoelectric energy conversion. in *XVII International Conference on Thermoelectrics, 1998. Proceedings ICT 98* 37–42 (1998).

44. Slack, G. A. New materials and performance limits for thermoelectric cooling. *CRC Handb. Thermoelectr.* **407,** (1995).

45. Dresselhaus, M. S. *et al.* New Directions for Low-Dimensional Thermoelectric Materials. *Adv. Mater.* **19,** 1043–1053 (2007).

46. Snyder, G. J. & Toberer, E. S. Complex thermoelectric materials. *Nat. Mater.* **7,** 105–114 (2008).

47. Lv, H. Y., Lu, W. J., Shao, D. F. & Sun, Y. P. Large thermoelectric power factors in black phosphorus and phosphorene. *ArXiv14045171 Cond-Mat* (2014).

48. Castro Neto, A. H., Guinea, F., Peres, N. M. R., Novoselov, K. S. & Geim, A. K. The electronic properties of graphene. *Rev. Mod. Phys.* **81,** 109–162 (2009).

49. Wallace, P. R. The Band Theory of Graphite. *Phys. Rev.* **71,** 622–634 (1947).

50. Novoselov, K. S. *et al.* Electric Field Effect in Atomically Thin Carbon Films. *Science* **306,** 666–669 (2004).

51. Das Sarma, S., Adam, S., Hwang, E. H. & Rossi, E. Electronic transport in two-dimensional graphene. *Rev. Mod. Phys.* **83,** 407–470 (2011).

52. Lee, C., Wei, X., Kysar, J. W. & Hone, J. Measurement of the Elastic Properties and Intrinsic Strength of Monolayer Graphene. *Science* **321,** 385–388 (2008).

53. Kim, E.-A. & Neto, A. H. C. Graphene as an electronic membrane. *EPL Europhys. Lett.* **84,** 57007 (2008).

54. Cooper, D. R. *et al.* Experimental Review of Graphene. *Int. Sch. Res. Not.* **2012,** e501686 (2012).

55. Vozmediano, M. A. H. Renormalization group aspects of graphene. *Philos. Trans. R. Soc. Lond. Math. Phys. Eng. Sci.* **369,** 2625–2642 (2011).

56. Novoselov, K. S. *et al.* Two-dimensional gas of massless Dirac fermions in graphene. *Nature* **438,** 197–200 (2005).

57. Tan, Y.-W. *et al.* Measurement of Scattering Rate and Minimum Conductivity in Graphene. *Phys. Rev. Lett.* **99,** 246803 (2007).

58. Chen, J.-H. *et al.* Charged-impurity scattering in graphene. *Nat. Phys.* **4,** 377–381 (2008).

59. Józsa, C. *et al.* Linear scaling between momentum and spin scattering in graphene. *Phys. Rev. B* **80,** 241403 (2009).

60. Liu, H. *et al.* Phosphorene: An Unexplored 2D Semiconductor with a High Hole Mobility. *ACS Nano* **8,** 4033–4041 (2014).

61. Delhaes, P. *Graphite and Precursors*. (CRC Press, 2000).

62. Brown, A. & Rundqvist, S. Refinement of the crystal structure of black phosphorus. *Acta Crystallogr.* **19,** 684–685 (1965).

63. Takao, Y., Asahina, H. & Morita, A. Electronic Structure of Black Phosphorus in Tight Binding Approach. *J. Phys. Soc. Jpn.* **50,** 3362–3369 (1981).

64. Jamieson, J. C. Crystal Structures Adopted by Black Phosphorus at High Pressures. *Science* **139,** 1291–1292 (1963).

65. Kawamura, H., Shirotani, I. & Tachikawa, K. Anomalous superconductivity in black phosphorus under high pressures. *Solid State Commun.* **49,** 879–881 (1984).

66. Wittig, J. & Matthias, B. T. Superconducting Phosphorus. *Science* **160,** 994–995 (1968).

67. Xia, F., Wang, H. & Jia, Y. Rediscovering black phosphorus as an anisotropic layered material for optoelectronics and electronics. *Nat. Commun.* **5,** (2014).

68. Castellanos-Gomez, A. *et al.* Isolation and characterization of few-layer black phosphorus. *2D Mater.* **1,** 025001 (2014).

69. Li, L. *et al.* Black phosphorus field-effect transistors. *Nat. Nanotechnol.* **9,** 372–377 (2014).

70. Hoffmann, R. An Extended Hückel Theory. I. Hydrocarbons. *J. Chem. Phys.* **39,** 1397–1412 (1963).

71. *Concepts in Spin Electronics*. (Series on Semiconductor Science and Technology 13, 2006).

72. Fert, A. & Campbell, I. A. Electrical resistivity of ferromagnetic nickel and iron based alloys. *J. Phys. F Met. Phys.* **6,** 849 (1976).

73. Van Son, P. C., van Kempen, H. & Wyder, P. Boundary Resistance of the Ferromagnetic-Nonferromagnetic Metal Interface. *Phys. Rev. Lett.* **58,** 2271–2273 (1987).

74. Jedema, F. J. Electrical spin injection in metallic mesoscopic spin valves. (2002).

75. Yang, T.-Y. *et al.* Observation of Long Spin-Relaxation Times in Bilayer Graphene at Room Temperature. *Phys. Rev. Lett.* **107,** 047206 (2011).

76. Avsar, A. *et al.* Toward Wafer Scale Fabrication of Graphene Based Spin Valve Devices. *Nano Lett.* **11,** 2363–2368 (2011).
77. Schmidt, G., Ferrand, D., Molenkamp, L. W., Filip, A. T. & van Wees, B. J. Fundamental obstacle for electrical spin injection from a ferromagnetic metal into a diffusive semiconductor. *Phys. Rev. B* **62,** R4790–R4793 (2000).
78. Moodera, J. S., Kinder, L. R., Wong, T. M. & Meservey, R. Large Magnetoresistance at Room Temperature in Ferromagnetic Thin Film Tunnel Junctions. *Phys. Rev. Lett.* **74,** 3273–3276 (1995).
79. Sakurai, J. J. & Tuan, S. F. *Modern Quantum Mechanics*. (Benjamin-Cummings Publishing Co.,Subs. of Addison Wesley Longman,US, 1985).
80. Mott, N. F. The Scattering of Fast Electrons by Atomic Nuclei. *Proc. R. Soc. Lond. Math. Phys. Eng. Sci.* **124,** 425–442 (1929).
81. The Theory of Atomic Collisions. Second Edition by N. F. Mott, H. S. W. Massey: Oxford University Press - Zubal Books (1950).
82. Berger, L. Side-Jump Mechanism for the Hall Effect of Ferromagnets. *Phys. Rev. B* **2,** 4559–4566 (1970).
83. Rashba, E. I. Side jump contribution to spin-orbit mediated hall effects and berry curvature. *Semiconductors* **42,** 905–908 (2008).
84. Karplus, R. & Luttinger, J. M. Hall Effect in Ferromagnetics. *Phys. Rev.* **95,** 1154–1160 (1954).
85. Hall, E. H. On the New Action of Magnetism on a Permanent Electric Current. *Philos Mag* **10,** (1880).
86. Smith, A. W. & Sears, R. W. The Hall Effect in Permalloy. *Phys. Rev.* **34,** 1466–1473 (1929).

87. Stern, N. P., Steuerman, D. W., Mack, S., Gossard, A. C. & Awschalom, D. D. Time-resolved dynamics of the spin Hall effect. *Nat. Phys.* **4,** 843–846 (2008).

88. Stern, N. P. *et al.* Current-Induced Polarization and the Spin Hall Effect at Room Temperature. *Phys. Rev. Lett.* **97,** 126603 (2006).

89. Valenzuela, S. O. & Tinkham, M. Direct electronic measurement of the spin Hall effect. *Nature* **442,** 176–179 (2006).

90. Kimura, T., Otani, Y., Sato, T., Takahashi, S. & Maekawa, S. Room-Temperature Reversible Spin Hall Effect. *Phys. Rev. Lett.* **98,** 156601 (2007).

91. Vila, L., Kimura, T. & Otani, Y. Evolution of the Spin Hall Effect in Pt Nanowires: Size and Temperature Effects. *Phys. Rev. Lett.* **99,** 226604 (2007).

92. Mihajlović, G., Pearson, J., Garcia, M., Bader, S. & Hoffmann, A. Negative Nonlocal Resistance in Mesoscopic Gold Hall Bars: Absence of the Giant Spin Hall Effect. *Phys. Rev. Lett.* **103,** 166601 (2009).

93. Abanin, D., Shytov, A., Levitov, L. & Halperin, B. Nonlocal charge transport mediated by spin diffusion in the spin Hall effect regime. *Phys. Rev. B* **79,** 035304 (2009).

94. Hankiewicz, E. M., Molenkamp, L. W., Jungwirth, T. & Sinova, J. Manifestation of the spin Hall effect through charge-transport in the mesoscopic regime. *Phys. Rev. B* **70,** 241301 (2004).

95. Brüne, C. *et al.* Evidence for the ballistic intrinsic spin Hall effect in HgTe nanostructures. *Nat. Phys.* **6,** 448–454 (2010).

96. Brüne, C. *et al.* Spin polarization of the quantum spin Hall edge states. *Nat. Phys.* **8,** 485–490 (2012).

97. Kane, C. & Mele, E. Quantum Spin Hall Effect in Graphene. *Phys. Rev. Lett.* **95,** 226801 (2005).

98. Huertas-Hernando, D., Guinea, F. & Brataas, A. Spin-orbit coupling in curved graphene, fullerenes, nanotubes, and nanotube caps. *Phys. Rev. B* **74,** 155426 (2006).

99. Trauzettel, B., Bulaev, D. V., Loss, D. & Burkard, G. Spin qubits in graphene quantum dots. *Nat. Phys.* **3,** 192–196 (2007).

100. Castro Neto, A. & Guinea, F. Impurity-Induced Spin-Orbit Coupling in Graphene. *Phys. Rev. Lett.* **103,** 026804 (2009).

101. Ochoa, H., Castro Neto, A. & Guinea, F. Elliot-Yafet Mechanism in Graphene. *Phys. Rev. Lett.* **108,** 206808 (2012).

102. Zomer, P. J., Guimarães, M. H. D., Tombros, N. & van Wees, B. J. Long-distance spin transport in high-mobility graphene on hexagonal boron nitride. *Phys. Rev. B* **86,** 161416 (2012).

103. Maassen, T. *et al.* Localized States Influence Spin Transport in Epitaxial Graphene. *Phys. Rev. Lett.* **110,** 067209 (2013).

104. Elliott, R. J. Theory of the Effect of Spin-Orbit Coupling on Magnetic Resonance in Some Semiconductors. *Phys. Rev.* **96,** 266–279 (1954).

105. Yafet, Y. *Solid State Physics, Vol. 14, edited by F. Seitz, and D. Turnbull*. (Academic Press, New York, 1963).

106. Dyakonov, M. I. & Perel, V. I. Spin relaxation of conduction electrons in noncentrosymmetric semiconductors. *Sov. Phys. Solid State Ussr* **13,** 3023–3026 (1972).

107. Maassen, T., Dejene, F. K., Guimarães, M. H. D., Józsa, C. & van Wees, B. J. Comparison between charge and spin transport in few-layer graphene. *Phys. Rev. B* **83,** 115410 (2011).

108. Han, W. & Kawakami, R. K. Spin Relaxation in Single-Layer and Bilayer Graphene. *Phys. Rev. Lett.* **107,** 047207 (2011).

109. Ertler, C., Konschuh, S., Gmitra, M. & Fabian, J. Electron spin relaxation in graphene: The role of the substrate. *Phys. Rev. B* **80,** 041405 (2009).
110. Kittel, C. *Introduction to Solid State Physics*. (Wiley, 2004).
111. MacDonald, D. K. C. *Thermoelectricity: An Introduction to the Principles*. (Courier Corporation, 2013).
112. Balandin, A. A. Thermal properties of graphene and nanostructured carbon materials. *Nat. Mater.* **10,** 569–581 (2011).
113. Ioffe, A. F. & Goldsmid, H. J. *Physics of semiconductors*. (Infosearch London, 1960).
114. Nair, R. R. *et al.* Fine Structure Constant Defines Visual Transparency of Graphene. *Science* **320,** 1308–1308 (2008).
115. Blake, P. *et al.* Making graphene visible. *Appl. Phys. Lett.* **91,** 063124 (2007).
116. Cullen, W. *et al.* High-Fidelity Conformation of Graphene to SiO2 Topographic Features. *Phys. Rev. Lett.* **105,** 215504 (2010).
117. Ferrari, A. C. & Basko, D. M. Raman spectroscopy as a versatile tool for studying the properties of graphene. *Nat. Nanotechnol.* **8,** 235–246 (2013).
118. Koenig, S. P., Doganov, R. A., Schmidt, H., Neto, A. H. C. & Özyilmaz, B. Electric field effect in ultrathin black phosphorus. *Appl. Phys. Lett.* **104,** 103106 (2014).
119. Li, X. *et al.* Large-Area Synthesis of High-Quality and Uniform Graphene Films on Copper Foils. *Science* **324,** 1312–1314 (2009).
120. Bae, S. *et al.* Roll-to-roll production of 30-inch graphene films for transparent electrodes. *Nat. Nanotechnol.* **5,** 574–578 (2010).
121. Elias, D. C. *et al.* Control of Graphene's Properties by Reversible Hydrogenation: Evidence for Graphane. *Science* **323,** 610–613 (2009).
122. Nair, R. R. *et al.* Fluorographene: A Two-Dimensional Counterpart of Teflon. *Small* **6,** 2877–2884 (2010).

123. Fert, A. & Levy, P. Spin Hall Effect Induced by Resonant Scattering on Impurities in Metals. *Phys. Rev. Lett.* **106,** 157208 (2011).

124. Kuemmeth, F., Ilani, S., Ralph, D. C. & McEuen, P. L. Coupling of spin and orbital motion of electrons in carbon nanotubes. *Nature* **452,** 448–452 (2008).

125. Jespersen, T. S. *et al.* Gate-dependent spin-orbit coupling in multielectron carbon nanotubes. *Nat. Phys.* **7,** 348–353 (2011).

126. Dyakonov, M. I. & Perel, V. I. Current-induced spin orientation of electrons in semiconductors. *Phys. Lett. A* **35,** 459–460 (1971).

127. Abanin, D. A. *et al.* Giant Nonlocality Near the Dirac Point in Graphene. *Science* **332,** 328–330 (2011).

128. Kane, C. & Mele, E. Z2 Topological Order and the Quantum Spin Hall Effect. *Phys. Rev. Lett.* **95,** 146802 (2005).

129. Schmidt, M. & Loss, D. Edge states and enhanced spin-orbit interaction at graphene/graphane interfaces. *Phys. Rev. B* **81,** 165439 (2010).

130. Zhou, J., Liang, Q. & Dong, J. Enhanced spin–orbit coupling in hydrogenated and fluorinated graphene. *Carbon* **48,** 1405–1409 (2010).

131. Rappoport, T., Uchoa, B. & Castro Neto, A. Magnetism and magnetotransport in disordered graphene. *Phys. Rev. B* **80,** 245408 (2009).

132. Seki, T. *et al.* Giant spin Hall effect in perpendicularly spin-polarized FePt/Au devices. *Nat. Mater.* **7,** 125–129 (2008).

133. Ryu, S. *et al.* Reversible Basal Plane Hydrogenation of Graphene. *Nano Lett.* **8,** 4597–4602 (2008).

134. Jaiswal, M. *et al.* Controlled Hydrogenation of Graphene Sheets and Nanoribbons. *ACS Nano* **5,** 888–896 (2011).

135. Cançado, L. G. *et al.* Quantifying Defects in Graphene via Raman Spectroscopy at Different Excitation Energies. *Nano Lett.* **11,** 3190–3196 (2011).

136. Hornekær, L. *et al.* Clustering of Chemisorbed H(D) Atoms on the Graphite (0001) Surface due to Preferential Sticking. *Phys. Rev. Lett.* **97,** 186102 (2006).

137. McCreary, K., Swartz, A., Han, W., Fabian, J. & Kawakami, R. Magnetic Moment Formation in Graphene Detected by Scattering of Pure Spin Currents. *Phys. Rev. Lett.* **109,** 186604 (2012).

138. Kettemann, S. Dimensional Control of Antilocalization and Spin Relaxation in Quantum Wires. *Phys. Rev. Lett.* **98,** 176808 (2007).

139. Huertas-Hernando, D., Guinea, F. & Brataas, A. Spin-Orbit-Mediated Spin Relaxation in Graphene. *Phys. Rev. Lett.* **103,** 146801 (2009).

140. Geim, A. K. & Novoselov, K. S. The rise of graphene. *Nat. Mater.* **6,** 183–191 (2007).

141. Berger, C. *et al.* Electronic Confinement and Coherence in Patterned Epitaxial Graphene. *Science* **312,** 1191–1196 (2006).

142. Robinson, J. T. *et al.* Properties of Fluorinated Graphene Films. *Nano Lett.* **10,** 3001–3005 (2010).

143. Cheng, S.-H. *et al.* Reversible fluorination of graphene: Evidence of a two-dimensional wide bandgap semiconductor. *Phys. Rev. B* **81,** 205435 (2010).

144. Jeong, H. Y. *et al.* Graphene Oxide Thin Films for Flexible Nonvolatile Memory Applications. *Nano Lett.* **10,** 4381–4386 (2010).

145. Joung, D., Chunder, A., Zhai, L. & Khondaker, S. I. High yield fabrication of chemically reduced graphene oxide field effect transistors by dielectrophoresis. *Nanotechnology* **21,** 165202 (2010).

146. Eda, G., Mattevi, C., Yamaguchi, H., Kim, H. & Chhowalla, M. Insulator to Semimetal Transition in Graphene Oxide. *J. Phys. Chem. C* **113,** 15768–15771 (2009).

147. Lee, J. H. *et al.* Property Control of Graphene by Employing 'Semi-Ionic' Liquid Fluorination. *Adv. Funct. Mater.* **23,** 3329–3334 (2013).

148. Lee, J. H. *et al.* One-Step Exfoliation Synthesis of Easily Soluble Graphite and Transparent Conducting Graphene Sheets. *Adv. Mater.* **21,** 4383–4387 (2009).

149. Marrows, C. H. & Hickey, B. J. New directions in spintronics. *Philos. Trans. R. Soc. Lond. Math. Phys. Eng. Sci.* **369,** 3027–3036 (2011).

150. Pai, C.-F. *et al.* Spin transfer torque devices utilizing the giant spin Hall effect of tungsten. *Appl. Phys. Lett.* **101,** 122404 (2012).

151. Pesin, D. & MacDonald, A. H. Spintronics and pseudospintronics in graphene and topological insulators. *Nat. Mater.* **11,** 409–416 (2012).

152. Hu, J., Alicea, J., Wu, R. & Franz, M. Giant Topological Insulator Gap in Graphene with 5d Adatoms. *Phys. Rev. Lett.* **109,** 266801 (2012).

153. Ferreira, A., Rappoport, T. G., Cazalilla, M. A. & Castro Neto, A. H. Extrinsic Spin Hall Effect Induced by Resonant Skew Scattering in Graphene. *Phys. Rev. Lett.* **112,** 066601 (2014).

154. Ding, J., Qiao, Z., Feng, W., Yao, Y. & Niu, Q. Engineering quantum anomalous/valley Hall states in graphene via metal-atom adsorption: An ab-initio study. *Phys. Rev. B* **84,** 195444 (2011).

155. Ma, D., Li, Z. & Yang, Z. Strong spin–orbit splitting in graphene with adsorbed Au atoms. *Carbon* **50,** 297–305 (2012).

156. Gmitra, M., Kochan, D. & Fabian, J. Spin-Orbit Coupling in Hydrogenated Graphene. *Phys. Rev. Lett.* **110,** 246602 (2013).

157. Pachoud, A., Ferreira, A., Özyilmaz, B. & Castro Neto, A. H. Scattering theory of spin-orbit active adatoms on graphene. *Phys. Rev. B* **90,** 035444 (2014).

158. Ando, Y. Topological Insulator Materials. *J. Phys. Soc. Jpn.* **82,** 102001 (2013).

159. Wang, L. *et al.* One-Dimensional Electrical Contact to a Two-Dimensional Material. *Science* **342,** 614–617 (2013).

160. Kim, K. S. *et al.* Large-scale pattern growth of graphene films for stretchable transparent electrodes. *Nature* **457,** 706–710 (2009).

161. Reina, A. *et al.* Large Area, Few-Layer Graphene Films on Arbitrary Substrates by Chemical Vapor Deposition. *Nano Lett.* **9,** 30–35 (2008).

162. Lin, Y.-C. *et al.* Graphene Annealing: How Clean Can It Be? *Nano Lett.* **12,** 414–419 (2011).

163. McCreary, K. M. *et al.* Effect of cluster formation on graphene mobility. *Phys. Rev. B* **81,** 115453 (2010).

164. Nakayama, H. *et al.* Detection of inverse spin-Hall effect induced in $Pt_{1-x}M_x$ (M = Cu, Au) thin films. *J. Phys. Conf. Ser.* **200,** 062014 (2010).

165. Gmitra, M., Konschuh, S., Ertler, C., Ambrosch-Draxl, C. & Fabian, J. Band-structure topologies of graphene: Spin-orbit coupling effects from first principles. *Phys. Rev. B* **80,** 235431 (2009).

166. Dean, C. R. *et al.* Boron nitride substrates for high-quality graphene electronics. *Nat. Nanotechnol.* **5,** 722–726 (2010).

167. Wel, W. van der, Harmans, C. J. P. M. & Mooij, J. E. A geometric explanation of the temperature dependence of the quantised Hall resistance. *J. Phys. C Solid State Phys.* **21,** L171 (1988).

168. Guignard, J., Leprat, D., Glattli, D. C., Schopfer, F. & Poirier, W. Quantum Hall effect in exfoliated graphene affected by charged impurities: Metrological measurements. *Phys. Rev. B* **85,** 165420 (2012).

169. Dyakonov, M. I. & Khaetskii, A. V. in *Spin Physics in Semiconductors* (ed. Dyakonov, P. M. I.) 211–243 (Springer Berlin Heidelberg, 2008).

170. Renard, J., Studer, M. & Folk, J. A. Origins of Nonlocality Near the Neutrality Point in Graphene. *Phys. Rev. Lett.* **112,** 116601 (2014).

171. Rudolph, M. *et al.* Dependence of the Spin Coherence Length on Wire Width for Quasi-1-Dimensional InSb and InAs Wires and Bi Wire Surface States. in *AIP Conference Proceedings* **1416,** 171–173 (AIP Publishing, 2011).

172. Patra, A. K. *et al.* Dynamic spin injection into chemical vapor deposited graphene. *Appl. Phys. Lett.* **101,** 162407 (2012).

173. Shchelushkin, R. V. & Brataas, A. Spin Hall effect, Hall effect, and spin precession in diffusive normal metals. *Phys. Rev. B* **72,** 073110 (2005).

174. Appelbaum, I., Huang, B. & Monsma, D. J. Electronic measurement and control of spin transport in silicon. *Nature* **447,** 295–298 (2007).

175. He, R. *et al.* Large Physisorption Strain in Chemical Vapor Deposition of Graphene on Copper Substrates. *Nano Lett.* **12,** 2408–2413 (2012).

176. Gradhand, M., Fedorov, D. V., Zahn, P. & Mertig, I. Extrinsic Spin Hall Effect from First Principles. *Phys. Rev. Lett.* **104,** 186403 (2010).

177. Ferreira, A. *et al.* Unified description of the dc conductivity of monolayer and bilayer graphene at finite densities based on resonant scatterers. *Phys. Rev. B* **83,** 165402 (2011).

178. Novoselov, K. S. *et al.* Two-dimensional atomic crystals. *Proc. Natl. Acad. Sci. U. S. A.* **102,** 10451–10453 (2005).

179. Geim, A. K. & Grigorieva, I. V. Van der Waals heterostructures. *Nature* **499,** 419–425 (2013).

180. Zuev, Y. M., Chang, W. & Kim, P. Thermoelectric and Magnetothermoelectric Transport Measurements of Graphene. *Phys. Rev. Lett.* **102,** 096807 (2009).

181. Wei, P., Bao, W., Pu, Y., Lau, C. N. & Shi, J. Anomalous Thermoelectric Transport of Dirac Particles in Graphene. *Phys. Rev. Lett.* **102,** 166808 (2009).

182. Vera-Marun, I. J., Ranjan, V. & van Wees, B. J. Nonlinear detection of spin currents in graphene with non-magnetic electrodes. *Nat. Phys.* **8,** 313–316 (2012).

183. Wu, J. *et al.* Large Thermoelectricity via Variable Range Hopping in Chemical Vapor Deposition Grown Single-Layer MoS2. *Nano Lett.* **14,** 2730–2734 (2014).

184. Small, J. P., Perez, K. M. & Kim, P. Modulation of Thermoelectric Power of Individual Carbon Nanotubes. *Phys. Rev. Lett.* **91,** 256801 (2003).

185. Brovman, Y. M. *et al.* Electric Field Effect Thermoelectric Transport in Individual Silicon and Germanium/Silicon Nanowire. *ArXiv13070249 Cond-Mat* (2013).

186. Bakker, F. L., Flipse, J. & Wees, B. J. van. Nanoscale temperature sensing using the Seebeck effect. *J. Appl. Phys.* **111,** 084306 (2012).

187. Bell, L. E. Cooling, Heating, Generating Power, and Recovering Waste Heat with Thermoelectric Systems. *Science* **321,** 1457–1461 (2008).

188. Heremans, J. P., Dresselhaus, M. S., Bell, L. E. & Morelli, D. T. When thermoelectrics reached the nanoscale. *Nat. Nanotechnol.* **8,** 471–473 (2013).

189. Slack, G. A. Thermal Conductivity of Elements with Complex Lattices: B, P, S. *Phys. Rev.* **139,** A507–A515 (1965).

190. Schroder, D. K. in *Semiconductor Material and Device Characterization* 465–522 (John Wiley & Sons, Inc., 2005).

191. Venkatasubramanian, R., Siivola, E., Colpitts, T. & O'Quinn, B. Thin-film thermoelectric devices with high room-temperature figures of merit. *Nature* **413,** 597–602 (2001).

192. Herring, C. Theory of the Thermoelectric Power of Semiconductors. *Phys. Rev.* **96,** 1163–1187 (1954).

193. Frederikse, H. P. R. Thermoelectric Power of Germanium below Room Temperature. *Phys. Rev.* **92,** 248–252 (1953).

194. Weber, L. & Gmelin, E. Transport properties of silicon. *Appl. Phys. A* **53,** 136–140 (1991).

195. Boukai, A. I. *et al.* Silicon nanowires as efficient thermoelectric materials. *Nature* **451,** 168–171 (2008).

196. Takahashi, H., Okazaki, R., Yasui, Y. & Terasaki, I. Low-temperature magnetotransport of the narrow-gap semiconductor $FeSb_2$. *Phys. Rev. B* **84,** 205215 (2011).

197. Sales, B. C. *et al.* Transport, thermal, and magnetic properties of the narrow-gap semiconductor $CrSb_2$. *Phys. Rev. B* **86,** 235136 (2012).

LIST OF PUBLICATIONS

1. A. Avsar, J. H. Lee, **G. K. W. Koon**, B. Özyilmaz, Enhanced spin-orbit coupling in dilute fluorinated graphene, Submitted to 2D Materials at the time of thesis submission (2015).
2. I. J. Vera-Marun*, **G. K. W. Koon***, J. Wu and B. Özyilmaz, Colossal thermoelectric response in few-layer black phosphorus, Submitted to Nature Materials at the time of thesis submission (2015).
3. J. Wu*, **G. K. W. Koon***, D. Xiang*, C. Han, C. T. Toh, E. S. Kulkarni, I. Verzhbitskiy, A. Carvalho, A. S. Rodin, S. P. Koenig, G. Eda, W. Chen, A. H. Castro Neto and B. Özyilmaz, Colossal ultraviolet photoresponsivity of few-layer black phosphorus, Submitted to ACS Nano at the time of thesis submission (2015).
4. X. Luo, X. Lu, G. K. W. Koon, A. H. Castro Neto, B. Özyilmaz, Q. Xiong, S. Y. Quek, Large frequency change with thickness in interlayer breathing mode - Significant interlayer interactions in few layer black phosphorus, Nanoletters 15(6), 3931-3938 (2015).
5. A. Avsar, J. Y. Tan, T. Taychatanapat, J. Balakrishnan, **G. K. W. Koon**, Y. Yeo, J. Lahiri, A. Carvalho, A. S. Rodin, E. C. T. O'Farrell, G. Eda, A. H. Castro Neto and B. Özyilmaz, Spin-orbit proximity effect in graphene, Nature Communications 5, 4875 (2014).
6. J. Balakrishnan*, **G. K. W. Koon***, A. Avsar, Y. Ho, J. H. Lee, M. Jaiswal, S. Baeck, J. Ahn, A. Ferreira, M. A. Cazalilla, A. H. Castro Neto and B. Özyilmaz, Giant spin Hall effect in graphene grown by chemical vapour deposition, Nature Communications 5, 4748 (2014).
7. J. Y. Tan, A. Avsar, J. Balakrishnan, **G. K. W. Koon**, T. Taychatanapat, E. C. T. O'Farrell, K. Watanabe, T. Taniguchi, G. Eda, A. H. Castro Neto and B. Özyilmaz,

Electronic transport in graphene-based heterostructures, Applied Physics Letters 104, 183504 (2014).

8. J. H. Lee, **G. K. W. Koon**, D. W. Shin, V. E. Fedorov, J. Choi, J. Yoo and B. Özyilmaz, Property control of graphene by employing “semi-ionic” liquid fluorination, Advanced Functional Materials 23(26), 3329-3334 (2013).
9. J. Balakrishnan*, **G. K. W. Koon***, M. Jaiswal, A. H. Castro Neto and B. Özyilmaz, Colossal enhancement of spin-orbit coupling in weakly hydrogenated graphene, Nature Physics 9, 284-287 (2013).
10. Y. Huang, J. Wu, X. Xu, Y. Ho, G. Ni, Q. Zou, **G. K. W. Koon**, W. Zhao, A. H. Castro Neto, G. Eda, C. Shen and B. Özyilmaz, An innovative way of etching MoS_2: Characterization and mechanistic investigation, Nano Research 6(3), 200-207 (2013).
11. S. X. Lim, **G. K. W. Koon**, D. Zhan, Z. Shen, B. Özyilmaz and C. Sow, Assembly of suspended graphene on carbon nanotube scaffolds with improved functionalities, Nano Research 5(11), 783-795 (2012).